Local Ion Velocity Measurements in the MST Saturated Single Helical Axis State

by
John Boguski

A dissertation submitted in partial fulfillment of
the requirements for the degree of

Doctor of Philosophy
(Physics)

at the
UNIVERSITY OF WISCONSIN - MADISON
2019

The dissertation is approved by the following members of the Final Oral Committee:

Mark Nornberg, Scientist, Engineering Physics
Carl Sovinec, Professor, Engineering Physics
John Sarff, Professor, Physics
Paul Terry, Professor, Physics

Acknowledgments

I would like to thank Mark Nornberg and John Sarff for their advice, encouragement, and overall good nature throughout my time here, and especially the thesis writing process. Without their help, I would certainly not have made it through graduate school.

The University of Wisconsin plasma physics program is an incredibly friendly and collaborative place to work. There were no shortage of doors to knock on whenever I was stuck, or needed a distractions. This includes not just the MST science and engineering team, but the entire group of plasma physics graduate students, to all of whom I am very grateful for your time, consideration, and friendship.

A special thanks to Urvashi Gupta and Karsten McCollam for running simulations for this project. Also to Takashi Nishizawa and Anthony Xing, who's work on the CHERS system was invaluable to its successful operation. A thanks, as well, to the many MST operators and diagnosticians that had to put up with the long hours of my run days.

Finally, I would like to thank my family for all of their support and encouragement over the last seven years of graduate school, and for a lifetime of fostering my interest in science and learning.

Abstract

The first local velocity measurements of helical equilibrium plasmas in the RFP are made to characterize the equilibrium flow profile. In high current, low density MST plasmas, the island associated with the innermost resonant tearing mode can grow and envelop the magnetic axis, resulting in a saturated Single Helical Axis (SHAx) equilibrium. The process by which this self-organized transition occurs is not fully understood. Theory and modeling suggest that viscous dissipation or large flow or magnetic shear might stimulate the transition. Local, toroidally resolved non-axisymmetric velocity measurements are obtained with a CHERS diagnostic while using a resonant magnetic perturbation to control the orientation of the helical plasma. The axisymmetric part of the flow is a rigid-rotor-like poloidal flow and relatively flat toroidal flow. Outside of the core, r/a > 0.5, the non-axisymmetric flow shows variations of order 10 km/s and more structure than a simple sinusoidal variation matching the helical variation of the magnetic axis. The toroidally resolved helical flow shear measured by CHERS may be comparable to strength of the critical shear necessary to mute nonlinear coupling of tearing modes. Flow measurements are compared with preliminary NIMROD simulations of visco-resistive, single-fluid MHD in toroidal and cylindrical geometry with full and limited axial periodicity. Both measurements and toroidal simulations show stronger inboard flows relative to the outboard. In the experiment, the $n = 5$ component of the poloidal flow is phase shifted by 0.7 rad from the reconnection-like flow observed in

the simulations, possibly due to decoupling of the ion and electron fluids over much of the plasma.

Contents

List of Figures

1. Introduction

Producing energy from fusion, the process of combining lighter elements to form heavier elements along with a release in energy, has been identified as a grand challenge for humanity, due to its promise to provide a longer term source of widely available, clean, safe electricity. Creating a fusion reactor capable of producing more power than it consumes has been a leading objective in plasma science and engineering for over fifty years, but has not yet been achieved. The basic problem is one of confining a hot plasma long enough for sufficient fusion reactions to occur for net power gain. Many plasma confinement schemes have been pursued, though none have achieved net electricity production yet. The focus of this thesis is on the reversed field pinch and a specific self-organized helical equilibrium within the device that leads to higher levels of confinement called the Single Helical Axis State (SHAx). Since this state forms spontaneously, there is minimum need for external control. While the historical motivation for developing the reversed field pinch and characterizing the Single Helical Axis State is for fusion energy, the state itself is an interesting plasma science problem involving self-organization through non-linear magnetohydrodynamic processes that are not fully understood.

1.1. The Reversed Field Pinch

The Reversed Field Pinch (RFP) is an axisymmetric toroidal plasma confinement device of interest to the fusion community as a potential economically attractive means of achieving ignition. External magnetic field coils are a strong cost driver in fusion experiments, but the RFP generates most of its magnetic field in the plasma itself through an externally applied inductive electric field. The applied electric field also ohmically heats the plasma, removing the need for other, more expensive auxiliary heating methods such as neutral beam injection or RF heating. The RFP belongs to a class of toroidal confinement concepts that use self-organization properties of the plasma to maintain confinement and equilibrium. The perturbed magnetic fields introduced by the self-organization process are detrimental to confinement, resulting in lower confinement than stellarator and tokamak devices of comparable size and input power. Ultimately, to be useful for fusion power, there must be sufficient confinement to achieve ignition.

The RFP is created by applying a toroidal inductive electric field along a toroidal magnetic field inside a conducting shell. The toroidal current generated from the inductive electric field creates a poloidal magnetic field, resulting in a paramagnetic pinch. In an ideal case, without resistivity or instabilities, this would be the end result. This is not the case, however, and the presence of both finite resistivity in the plasma and global MHD instabilities cause the plasma to continue to evolve.

The final state of a flux conserving plasma subject to magnetic fluctuations and resistivity was described by J. B. Taylor[1]. The analysis shows that global magnetic helicity, the inter-linkage of magnetic field lines described by:

$$K = \int \mathbf{A} \cdot \mathbf{B} dV \tag{1.1}$$

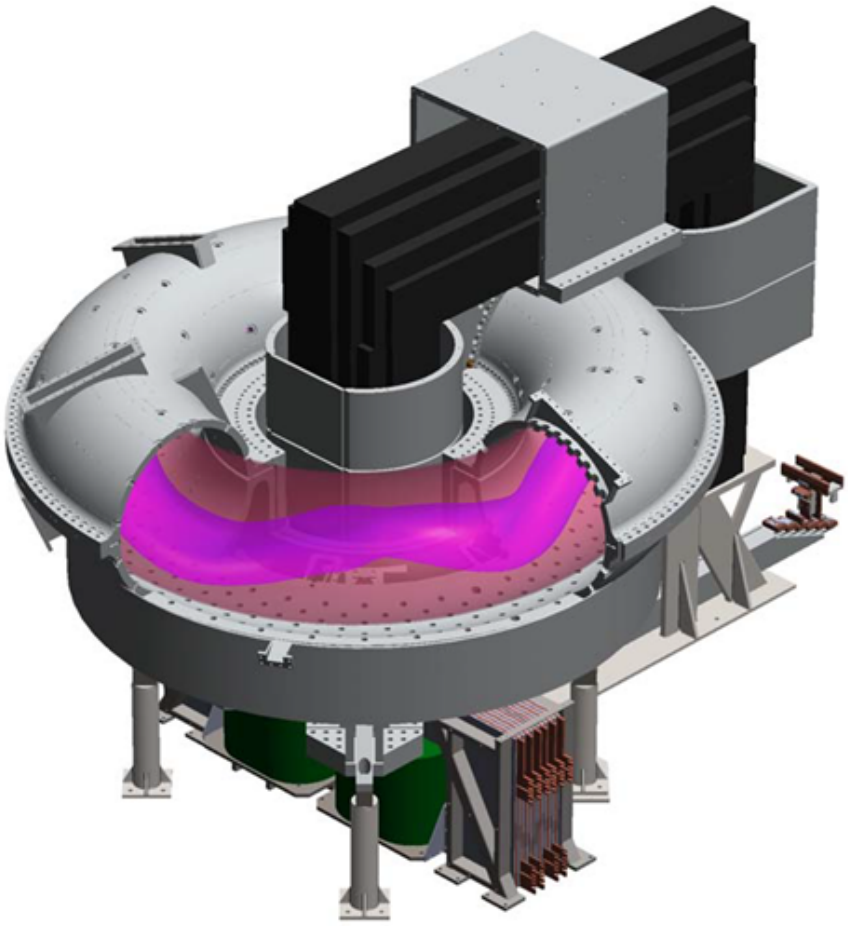

Figure 1.1.: The Madison Symmetric Torus machine.The dark red is an artistic representation of the QSH state helical core.

is better conserved than energy. In the equation above, K is the global magnetic helicity, $\mathbf{A}$ is the magnetic vector potential, and $\mathbf{B}$ is the magnetic field. Therefore global magnetic helicity acts as a strong constraint on the plasma evolution as the system undergoes energy minimization through relaxation. A system in a minimum energy state constrained by constant helicity satisfies:

$$\nabla \times \mathbf{B} = \lambda \mathbf{B} \tag{1.2}$$

where λ is a constant. Unlike the tokamak and stellarator, which have strong toroidal magnetic fields relative to their poloidal field, the RFP has poloidal and toroidal field of comparable strength. The pitch of the magnetic field is referred to as the safety-factor, or q-profile, and is written as:

$$q(r) = \frac{rB_\phi(r)}{RB_\theta(r)} \tag{1.3}$$

Due to the comparable poloidal and toroidal magnetic fields in RFPs $q(r) < 1$ everywhere, whereas for stellarators and tokamaks $q(r) > 1$ everywhere.

1.1.1. The Madison Symmetric Torus

The RFP used for experiments in this thesis is the Madison Symmetric Torus (MST)[2]. It is a toroidal confinement device capable of producing a relatively large volume of fusion relevant plasma. Some relevant MST parameters are reviewed in Table 1.1, and a diagram of the machine is shown in Figure 1.1. A key feature of MST is its 5 cm thick Aluminum shell that acts as both the conducting shell and vacuum vessel. The shell acts as a conducting boundary condition on the plasma, limiting the magnetic perturbations at the plasma edge, and inhibiting the growth of all external unstable magnetohydrodynamic modes. Due to the thickness of the shell, the magnetic soak through time is much longer than the lifetime of a plasma discharge, on the order of 800 ms[3] compared to 60 ms plasma discharges.

MST Parameters	
Parameter	Value
Plasma Current [kA]	500
B_0 [T]	0.5
Electron Temperature [eV]	800
β [%]	10
Major Radius [m]	1.5
Minor Radius [m]	0.5

Table 1.1.: Relevant MST parameters for plasma discharges analyzed in this thesis.

1.1.2. Tearing Modes and the Sawtooth Cycle

The detailed process by which relaxation occurs is not prescribed in Taylor's argument, only the final state in a system where helicity is conserved while energy is minimized. In the RFP, the dominant fluctuation that acts to redistribute current and minimize energy is the tearing mode instability. The tearing modes occur at rational surfaces in the q-profile of the RFP ($q = -m/n$ where m and n are integers), where field line bending of modes with the same pitch as the equilibrium magnetic field no longer prohibits the growth of magnetic perturbations. This condition is represented mathematically as:

$$\boldsymbol{k} \cdot \boldsymbol{B} = 0. \tag{1.4}$$

where $\boldsymbol{k} = \frac{m}{r}\hat{\theta} + \frac{n}{R}\hat{\phi}$ is the wavevector of the magnetic perturbation and $\boldsymbol{B}$ is the equilibrium magnetic field. This can be reworked for a condition on the q-profile:

$$\frac{m}{r}B_\theta + \frac{n}{R}B_\phi = 0 \tag{1.5}$$

$$\frac{rB_\phi}{RB_\theta} = -\frac{m}{n} \longrightarrow q = -\frac{m}{n}. \tag{1.6}$$

The perturbations "tear" magnetic field lines within a resistive layer through magnetic reconnection, forming a magnetic island with an O-point and X-point on the rational surface, shown in Figure 1.2. It is useful to define a new helical coordinate $\chi = m\theta + n\phi$, to describe the island perturbation, where m and n are the poloidal and toroidal mode numbers of the perturbation. Magnetic fields near the rational surface lie along lines of constant χ, and perturbations b_r and b_χ in the and $\hat{k}$ directions oscillate according to $\sin(\chi)$ and $\cos(\chi)$ respectively.

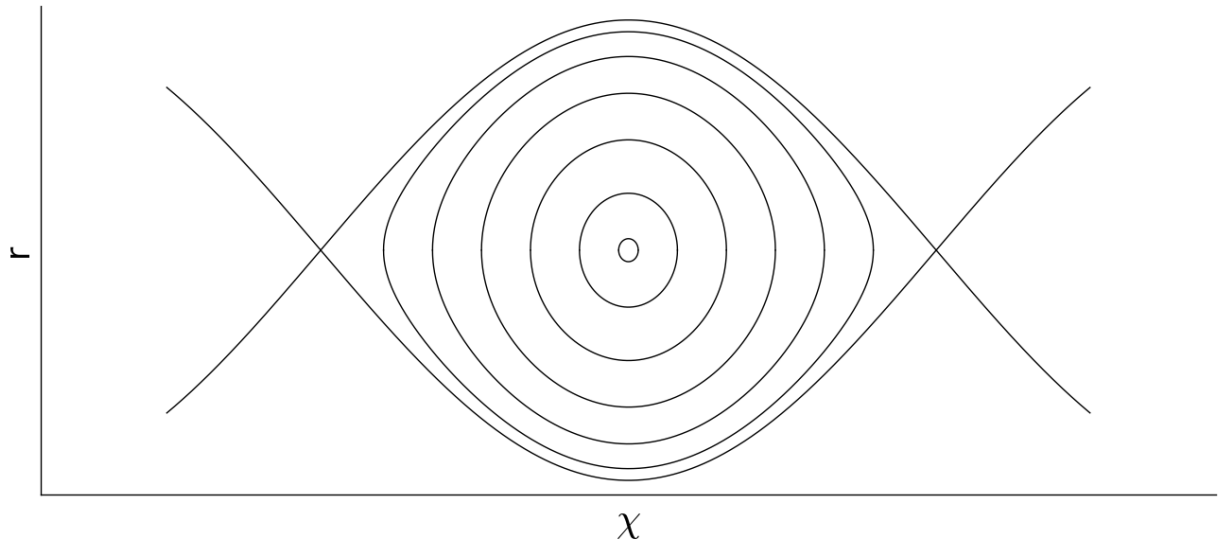

Figure 1.2.: Tearing mode induced island along helical coordinate plane.

Tearing modes and magnetic reconnection are only possible due to finite resistivity or other non-ideal effects in Ohm's law. The many rational flux surfaces in the RFP q-profile lead to many tearing modes at different radii. These $m = 1$ tearing modes are non-linearly coupled via three-wave coupling, dominantly by a global $(m, n) = (0, 1)$ mode resonant at the reversal surface. The many tearing modes lead to overlapping magnetic islands and the stochasitization of the magnetic fields. Electrons and ions confined to magnetic field lines can pass from the inner core of the plasma to the edge much more easily in a stochastic

magnetic field compared to one with ordered flux surfaces. The degree of transport caused by stochastic field lines is modified by the periodic rapid redistribution of current and magnetic flux called the sawtooth cycle, an integral part of the standard RFP[4].

1.1.3. Improved Confinement Strategies

The relatively poor confinement in standard RFP operation motivates the search for modes of operation in which the strength of tearing modes can be reduced so that the confinement can be improved. One method is through inductive control of the q-profile[5, 6]. The method of operation is referred to as Pulsed Parallel Current Drive (PPCD). In the edge, an electric field is induced parallel to the edge magnetic field such that Ohm's law is satisfied with reduced need for a dynamo contribution from perturbed field ($E_\parallel$ is enhanced in $E_\parallel + \left\langle \boldsymbol{v} \times \boldsymbol{B} \right\rangle_\parallel = \eta J_\parallel$). Over 10 ms of reduced tearing mode activity can be achieved in MST using this method, providing substantial improvements in confinement that rivals the confinement expected from a tokamak with similar size, magnetic field, and heating power[7]. This has been shown to be quite successful in reducing plasma stochasticity and improving confinement, but is intrinsically a pulsed process that cannot be sustained indefinitely.

Another approach is to operate in a regime where the inner-most tearing mode grows to sufficient strength that it causes flux surface healing and produces a 3D helical core of well-confined plasma[8, 9, 10]. A comparison of the improvement in thermal confinement with standard RFP operation is shown in Figure 1.3. This 3D equilibrium is referred to as the Single Helical Axis (SHAx) state, and is attractive because of its potential to operate as a steady-state reactor, and will be explored more fully in Chapter 2.

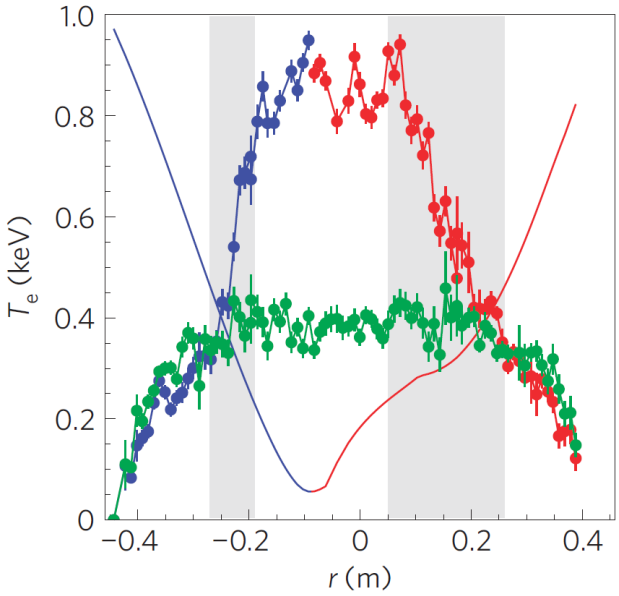

Figure 1.3.: Temperature profiles of a multi-helicity plasma (green) and a helical equilibrium plasma (blue and red) measured in RFX-mod. Blue and red colors indicate different sides of the helical magnetic equilibrium. Solid blue and red lines indicate the effective radial coordinate in reference to the helical magnetic equilibrium. The figure is reproduced from [8].

1.2. Motivation and Summary of Key Results

Plasma flows are a critical component of the RFP dynamo and the non-linear MHD involved in the formation and sustainment of the SHAx helical equilibrium, which is an inherently 3D phenomenon. Despite its importance, characterization of velocity in the RFP is generally sparse, and no local measurements of velocity in the saturated SHAx state exist. To fully understand the role velocity plays in the sustainment of the saturated SHAx state, characterization of the local 3D velocity is necessary. This work represents a step forward in the understanding of velocity structures in the saturated helical equilibrium, and provides important constraints and references for future theory and computational work.

The aim of this research is to provide experimental measurements of ion flow in the

saturated SHAx state and to provide constraints for theoretical models that try to explain the conditions in which the SHAx state is formed and sustained. The measurements were designed to answer the simple question:

What is the flow profile of an RFP's self-organized helical equilibrium?

This informs more detailed scientific questions such as:

- Does resistive dissipation play a role in the formation and sustainment of SHAx states?
- What are the effects of toroidal geometry on the flow profile?
- Are two-fluid effects in the helical equilibrium important to the dynamics of the SHAx state?
- Does flow shear affect non-linear energy transfer?

The data acquired in this thesis are toroidal and radial profiles of flow in the poloidal and toroidal plane in the saturated SHAx state. They reveal relatively uniform axisymmetric toroidal flow on the order of 10 km/s and poloidal flow that is rigid-rotor-like on the inboard side, but that peaks at the mid-radius and reverses on the outboard side. The non-axisymmetric flow is dominantly $n = 5$ inside of $r/a < 0.5$, and has a hollow poloidal profile. At measurement locations $r/a = 0.62$ and $r/a = -0.58$, the harmonics of the $n = 5$ flow in the poloidal plane dominate over the $n = 5$ flow.

The data and subsequent analysis in the thesis shed light on the above questions in the following ways:

- The radial profiles of flow in the poloidal plane observed in high-dissipation simulations are characteristically different than those observed in experimental results, having radial profiles in the poloidal plane that are peaked in the core where low-dissipation simulations and the experimental results have hollow profiles.

- A strong inboard/outboard asymmetry in the radial profile of axisymmetric flow in the poloidal plane is observed, but not observed in the radial profile of the $n = 5$ non-axisymmetric flow.
- Phase shifts in the dominant helical flow relative to the magnetic equilibrium are suggestive of decoupling of ion and electron flows seen in the two-fluid physics regime.
- The uncertainty in flow shear is too large between the helical core and the nearest sub-dominant tearing mode to compare to the critical shear necessary to affect sub-dominant tearing modes, based on an analysis of the eddy turnover time of the sub-dominant tearing modes.

Details of these results and the work performed to obtain them are given in the proceeding chapters as follows. Chapter 2 introduces details of the SHAx state, the past work done, and the models proposed to understand its onset and sustainment. Chapter 3 covers the tools used to characterize the SHAx state and its flow profiles. Chapter 4 presents the flow data and analysis techniques used to characterize the flow profiles. Chapter 5 uses simulation results in conjunction with the flow data to infer physical effects that can be observed in the data, and which effects are likely to be important in future simulations. Chapter 6 looks at the shear profiles available from the data. Chapter 7 reviews the conclusions drawn from the data and analysis.

References

[1] J. B. Taylor, "Relaxation of toroidal plasma and generation of reverse magnetic fields," *Physical Review Letters*, vol. 33, no. 19, pp. 1139–1141, 1974.

[2] R. N. Dexter, D. W. Kerst, T. W. Lovell, and S. C. Prager, "The Madison Symmetric Torus," *Fusion Technology*, vol. 19, pp. 131–139, 1990.

[3] B. E. Chapman, R. Fitzpatrick, D. Craig, P. Martin, and G. Spizzo, "Observation of tearing mode deceleration and locking due to eddy currents induced in a conducting shell," *Physics of Plasmas*, vol. 11, no. 5, pp. 2156–2171, 2004.

[4] S. Ortolani and D. Schnack, *The Magnetohydrodynamics of Plasma Relaxation*. World Scientific Publishing Company, 1993.

[5] J. S. Sarff, A. F. Almagri, M. Cekic, C. S. Chaing, D. Craig, D. J. Den Hartog, G. Fiksel, S. A. Hokin, R. W. Harvey, H. Ji, C. Litwin, S. C. Prager, D. Sinitsyn, C. R. Sovinec, J. C. Sprott, and E. Uchimoto, "Transport reduction by current profile control in the reversed-field pinch," *Physics of Plasmas*, vol. 2, no. 6, pp. 2440–2446, 1995.

[6] B. Chapman, *Fluctuation Reduction and Enhanced Confinement in the MST Reversed-Field Pinch*. PhD thesis, University of Wisconsin - Madison, 1997.

[7] J. S. Sarff, J. K. Anderson, T. M. Biewer, D. L. Brower, B. E. Chapman, P. K. Chattopadhyay, D. Craig, B. Deng, D. J. Den Hartog, W. X. Ding, G. Fiksel, C. B. Forest, J. A. Goetz, R. O'Connell, S. C. Prager, and M. A. Thomas, "Tokamak-like confinement at high beta and low field in the reversed field pinch," *Plasma Physics and Controlled Fusion*, vol. 45, no. 12 A, pp. A457–A470, 2003.

[8] R. Lorenzini, E. Martines, P. Piovesan, D. Terranova, P. Zanca, M. Zuin, A. Alfier, D. Bonfiglio, F. Bonomo, A. Canton, S. Cappello, L. Carraro, R. Cavazzana, D. F. Escande, A. Fassina, P. Franz, M. Gobbin, P. Innocente, L. Marrelli, R. Pasqualotto, M. E. Puiatti, M. Spolaore, M. Valisa, N. Vianello, P. Martin, L. Apolloni, M. E. Puiatti, J. Adamek, M. Agostini, A. Alfier, S. V. Annibaldi, V. Antoni, F. Auriemma, O. Barana, M. Baruzzo, P. Bettini, T. Bolzonella, D. Bonfiglio, F. Bonomo, M. Brom-

bin, J. Brotankova, A. Buffa, P. Buratti, A. Canton, S. Cappello, L. Carraro, R. Cavazzana, M. Cavinato, B. E. Chapman, G. Chitarin, S. D. Bello, A. D. Lorenzi, G. D. Masi, D. F. Escande, A. Fassina, A. Ferro, P. Franz, E. Gaio, E. Gazza, L. Giudicotti, F. Gnesotto, M. Gobbin, L. Grando, L. Guazzotto, S. C. Guo, V. Igochine, P. Innocente, Y. Q. Liu, R. Lorenzini, A. Luchetta, G. Manduchi, G. Marchiori, D. Marcuzzi, L. Marrelli, S. Martini, E. Martines, K. McCollam, F. Milani, M. Moresco, L. Novello, S. Ortolani, R. Paccagnella, R. Pasqualotto, S. Peruzzo, R. Piovan, L. Piron, A. Pizzimenti, N. Pomaro, I. Predebon, J. A. Reusch, G. Rostagni, G. Rubinacci, J. S. Sarff, F. Sattin, P. Scarin, G. Serianni, P. Sonato, E. Spada, A. Soppelsa, S. Spagnolo, M. Spolaore, G. Spizzo, C. Taliercio, D. Terranova, V. Toigo, M. Valisa, F. Villone, R. B. White, D. Yadikin, P. Zaccaria, A. Zamengo, P. Zanca, B. Zaniol, L. Zanotto, E. Zilli, H. Zohm, and M. Z. Zuin, "Self-organized helical equilibria as a new paradigm for ohmically heated fusion plasmas," *Nature Physics*, vol. 5, pp. 570–574, 8 2009.

[9] R. Lorenzini, M. Agostini, A. Alfier, V. Antoni, L. Apolloni, F. Auriemma, O. Barana, M. Baruzzo, P. Bettini, D. Bonfiglio, T. Bolzonella, F. Bonomo, M. Brombin, A. Buffa, A. Canton, S. Cappello, L. Carraro, R. Cavazzana, G. Chitarin, S. Dal Bello, A. De Lorenzi, G. De Masi, D. F. Escande, A. Fassina, P. Franz, E. Gaio, E. Gazza, L. Giudicotti, F. Gnesotto, M. Gobbin, L. Grando, S. C. Guo, P. Innocente, A. Luchetta, G. Manduchi, G. Marchiori, D. Marcuzzi, L. Marrelli, P. Martin, S. Martini, E. Martines, F. Milani, M. Moresco, L. Novello, S. Ortolani, R. Paccagnella, R. Pasqualotto, S. Peruzzo, R. Piovan, P. Piovesan, L. Piron, A. Pizzimenti, N. Pomaro, I. Predebon, M. E. Puiatti, G. Rostagni, F. Sattin, P. Scarin, G. Serianni, P. Sonato, E. Spada, A. Soppelsa, S. Spagnolo, G. Spizzo, M. Spolaore, C. Taliercio, D. Terranova, V. Toigo, M. Valisa, P. Veltri, N. Vianello, P. Zaccaria, B. Zaniol, L. Zanotto, E. Zilli, and M. Zuin, "Improvement of the magnetic configuration in the reversed field pinch through succes-

sive bifurcations," *Physics of Plasmas*, vol. 16, no. 5, p. 056109, 2009.

[10] R. Lorenzini, F. Auriemma, A. Fassina, E. Martines, D. Terranova, and F. Sattin, "Internal Transport Barrier Broadening through Subdominant Mode Stabilization in Reversed Field Pinch Plasmas," *Physical Review Letters*, vol. 116, no. 18, p. 185002, 2016.

2. Single Helical Axis State Physics

The Single Helical Axis state in the RFP has garnered significant interest in the fusion and plasma physics community both as a pathway to fusion energy production and as an interesting self-organized, non-linear MHD system. The cause for the spontaneous transition to the SHAx state is not fully understood. This chapter will introduce the background and relevant features of the SHAx transition and equilibrium state, as well as current theories as to how to state arises.

2.1. The QSH and SHAx States

The high-confinement, helical equilibrium is referred to as the Single Helical Axis state in literature. It is part of a larger parameter regime called Quasi-Single Helicity (QSH). QSH states are defined by the growth of the most unstable, innermost resonant tearing mode to large amplitude compared with higher toroidal mode number tearing modes (sub-dominant modes). Hints of these states were observed in early RFP experiments[1, 2, 3, 4]. Internal measurements of QSH states revealed helical thermal structures resulting from improved confinement of "healed" helical flux surfaces[5]. These results were connected to results from earlier computational efforts to produce a purely Single Helicity (SH) state RFP[6, 7]. The

presence of sub-dominant tearing modes at small, but finite amplitude distinguishes the SHAx state from the theoretical SH state.

QSH is empirically defined using a threshold value in the spectral index, N_s[4], which is a metric for describing the distribution of total energy between modes. The spectral index is defined as:

$$N_s = \left[\sum_n \left(\frac{\tilde{b}_n^2}{\sum_{n'} \tilde{b}_{n'}^2} \right)^2 \right]^{-1} \tag{2.1}$$

where n is the toroidal mode number, and $\tilde{b}_n$ is the magnetic mode amplitude of the specific toroidal mode measured at the wall. The spectral index scales inversely with increasing amplitude of a single mode. The threshold value of $N_s < 2$ is typically used to define a QSH state in literature.

QSH is most readily achieved when the toroidal magnetic field is forced to be zero at the wall, such that it is now a "non-reversed" RFP. It is inferred that by moving the reversal surface to the conducting wall and reducing the strength of the global $(m, n) = (0, 1)$ mode resonant at the reversal surface, the coupling between the dominant and sub-dominant tearing modes is also reduced, allowing the dominant mode to grow large. Non-reversed discharges are the only ones where the QSH state has grown and saturated for the duration of the discharge, as shown in Figure 2.1. As can be seen in the plot, during the growth and saturation of the $n = 5$ mode, the $(m, n) = (0, 1)$ burst activity corresponding to sawtoothing is not present.

In non-reversed plasmas, the strength and persistence of the QSH state is observed to scale with increasing plasma current as well as decreasing plasma density. Specifically, QSH strength and persistence empirically scales well with Lundquist number, the ratio of the

resistive time τ_R and Alfvén time τ_A [**?**].

$$S = \frac{\tau_R}{\tau_A} \propto \frac{I_p T_e^{3/2}}{\sqrt{n_e}} \tag{2.2}$$

where I_p is the plasma current, T_e is the electron temperature, and n_e is the electron density.

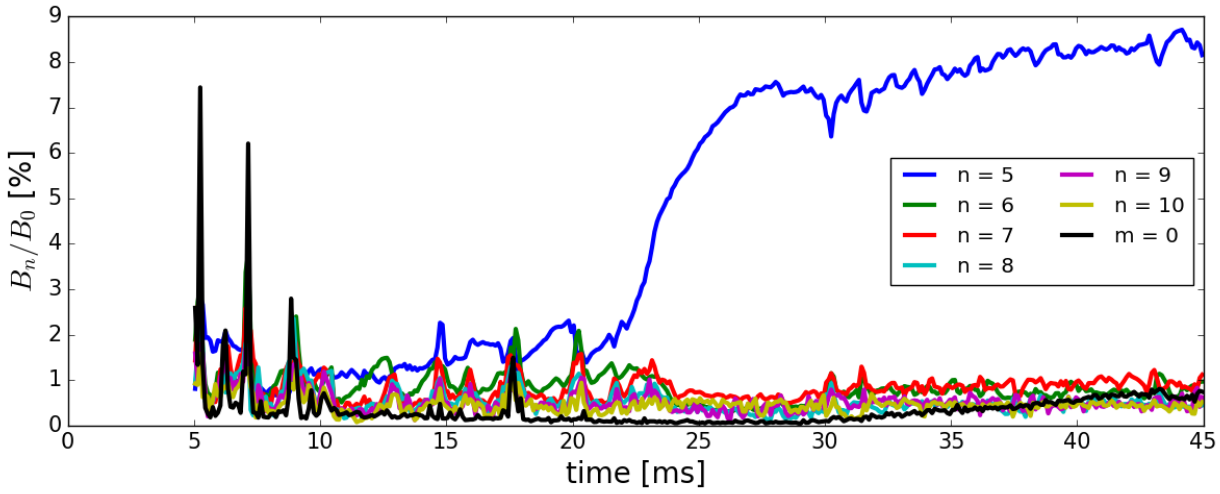

Figure 2.1.: Example of a long lived QSH discharge. The $n = 5$ magnetic field at the wall is representative of the strength of the $(m, n) = (1, 5)$ tearing mode strength in the plasma, which dominates over other, high n tearing modes.

Initially, the growing dominant tearing mode can be considered a second helical magnetic axis that co-exists with the axisymmetric magnetic axis. This regime is sometimes referred to as the Dual Axis (DAx) state[8]. Single shot electron temperature measurements of a heat-confining island have been made with a Thomson scattering diagnostic in the MST[9] and in RFX[10]. As the dominant mode grows, eventually the helical island encompasses the magnetic axis and only a single helical axis (SHAx) remains[11]. Sub-dominant modes are still present in this state and a large volume of the plasma outside of the helical core remains stochastic. The transition is represented in Figure 2.2, which shows Poincaré plots of DEBS RFP simulations. The QSH state in b.) is produced by artificially amplifying

the simulated tearing mode profile to levels relevant to QSH[12].

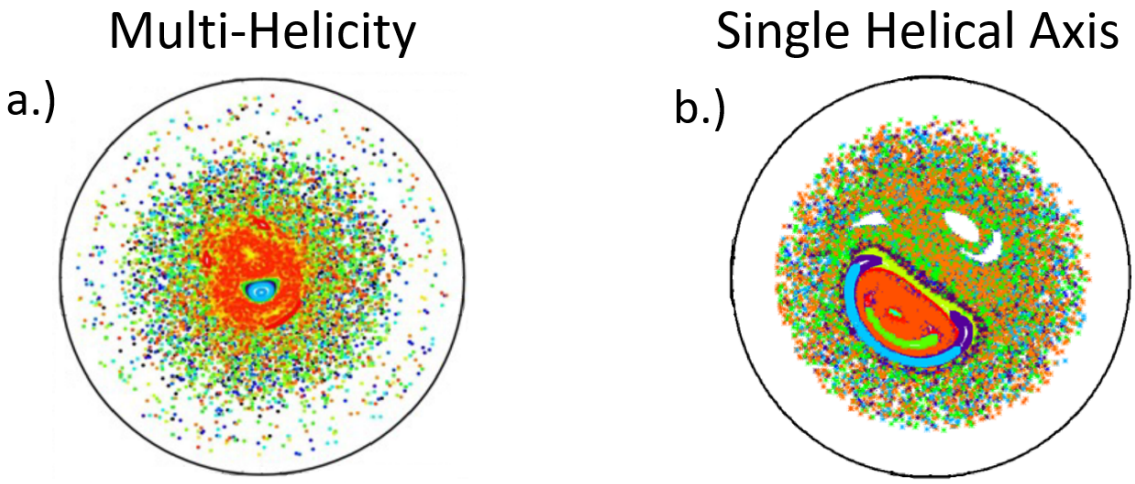

Figure 2.2.: a.) Representative Poincaré plots of a poloidal cross-section RFP plasma in a.) multi-helicity and b.) Single Helical Axis states taken from [12].

The transition to SHAx can be described mathematically as a saddle-node bifurcation, and involves the loss of the x-point of the island as it merges with the axisymmetric magnetic axis[5]. The transition is a significant topological change in the flux surfaces despite the magnetic energy in the dominant mode being only a fraction of the axisymmetric magnetic field energy. The evolution of the transition was described using Newcomb eigenfunctions scaled by the magnetic mode amplitude measured at the wall and applied to an axisymmetric equilibrium[13]. While this is a simplification of the equilibrium, it matches well with non-axisymmetries observed in soft-x-ray[14] and FIR polarimetry measurements[15]. The topological change is reflected in the average q-profile, which becomes three-dimensional, and is no longer monotonic[16]. A helical coordinate system is required to describe the new helical magnetic axis and helical flux surfaces. Since the flux surfaces in the helical core of the plasma take on the helicity of the dominant mode, the pitch of the magnetic field lines relative to the new helical surfaces is reduced. As a consequence of reduced values of q in the

helical core region of the plasma, the maximum of the q-profile lies between the helical core and the nearly axisymmetric edge[17]. The new q-profile also loses the resonant surface of the dominant mode helicity. The maximum q-value decreases scales inversely with increasing dominant mode strength, and tends to move radially outward with increasing mode strength as well[16, 18].

The transition to SHAx was initially associated with a jump in the volume of high electron thermal confinement[11, 19], but further investigations showed that the SHAx transition likely happens earlier than the observed jump in thermal confinement occurs [20]. The transition to SHAx can occur when the edge dominant mode amplitude is only 1.5% of the total edge magnetic field, while the jump in the width the of the region of high confinement occurs around 3.5%. The jump in the high confinement region volume is more closely associated with the reduction in secondary mode amplitudes. Below this amplitude, there is still a region with high electron temperature, but it is more strongly localized to the helical axis, and could be described equally well as a heat confining island.

I will further classify SHAx being in a growing or saturated state. While a topological SHAx state may occur at relatively low magnetic mode amplitude, the dominant mode may grow to significantly higher amplitude before reaching saturation. On average the state tends to saturate around $\tilde{B}_{Dom}/B(a) = 7\%$ in MST. This can be seen at about 26 ms in Figure 2.1, after which the $n = 5$ mode rolls over and only grows weakly in time. Figure 2.3 shows a density scatter plot of magnetic mode measurements for many shots. The dense region at high dominant mode amplitude is considered to be the "saturated SHAx" state. The dynamics in each of these different regimes is likely rich in physics, but it is the average properties of the saturated SHAx state that is the focus of this work. This regime could accurately also be called the saturated QSH state, as the dominant mode is much stronger than any sub-dominant modes, and it easily satisfies any metric for defining a QSH state.

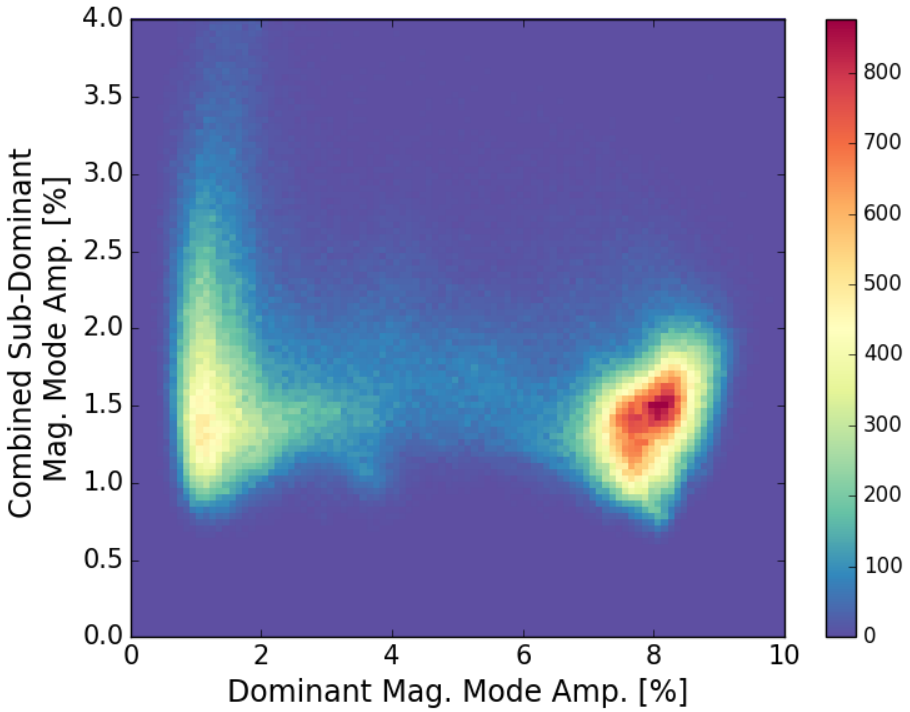

Figure 2.3.: 2D histogram of the magnetic signals of the dominant mode between 4-45 ms for a number of 500 kA non-reversed discharges. The saturated-SHAx state tends to begin at about a 7% dominant mode amplitude.

Despite early predictions of the possibility of a SHAx state, the cause of the onset and sustainment of QSH is still not fully understood. The current paradigm is that the state is caused by a reduction in the non-linear coupling of tearing modes, but the mechanism is not known. The next section will discuss several possibilities that have been explored in past work. Specifically, computational and theoretical work that has been done to reproduce a QSH state similar to what is seen in experiment.

2.2. Mechanisms for Computationally Producing a SHAx state

It is important to understand the mechanisms controlling the onset and sustainment of the SHAx state in order to improve experimental control of the state. Ultimately the plasma must obey an energy balance between tearing modes where each mode has some drive, dissipation, and energy transfer mechanisms. Typical tearing modes transfer energy to higher n tearing modes, which tend to be more stable, through three-wave coupling with $m = 0$ modes. This process drives sub-dominant modes that might otherwise be small compared with the unstable modes, thereby limiting the total amplitude of the dominant mode. So one way of generating a SHAx state computationally is to cut off the transfer of energy to high n modes.

Three paradigms for creating the SHAx state will be reviewed here: high-dissipation damping of tearing modes, application of an edge perturbation, and shear induced decoupling of the dominant and sub-dominant modes. The plasma description used for understanding the plasma and running simulations is magnetohydrodynamics (MHD)[21, 22]. Single-fluid MHD is described by the following equations:

$$\frac{\partial \rho}{\partial t} + \nabla \cdot \rho \boldsymbol{V} = 0, \tag{2.3}$$

and

$$\rho \frac{\partial \boldsymbol{V}}{\partial t} + \rho \boldsymbol{V} \cdot \nabla \boldsymbol{V} - \boldsymbol{J} \times \boldsymbol{B} + \nabla p = -\nabla \cdot \underline{\boldsymbol{\Pi}}, \tag{2.4}$$

and

$$\frac{\partial p}{\partial t} + \boldsymbol{V} \cdot \nabla p = -\Gamma p \nabla \cdot \boldsymbol{V} + (\Gamma - 1)[-\nabla \cdot \boldsymbol{q} + \underline{\boldsymbol{\Pi}} : \nabla \boldsymbol{V} + \eta \boldsymbol{J}^2], \tag{2.5}$$

and

$$\frac{\partial \boldsymbol{B}}{\partial \bar{t}} = \nabla \times (\boldsymbol{V} \times \boldsymbol{B} - \eta \boldsymbol{J}) \tag{2.6}$$

where $\boldsymbol{V}$ is the ion velocity, ρ is the fluid density, $\boldsymbol{J}$ is the plasma current, $\boldsymbol{B}$ is the magnetic field, $\underline{\boldsymbol{\Pi}}$ is the stress tensor, p is the pressure, Γ is the adiabatic index (5/3 for a plasma), $\boldsymbol{q}$ is the heat flux, and η is the plasma resistivity. Expressions for $\underline{\boldsymbol{\Pi}}$, $\boldsymbol{q}$, and η, close the system of equations, but depend on the specific properties of the plasma being considered.

2.2.1. high-dissipation of sub-dominant tearing modes

Early computational efforts relied on high viscous dissipation to achieve a SH state [6, 7]. Highly resistive simulations were later found to also cause a transition to a SH state, and a succinct criterion for transitioning to an SH state was described using the Hartmann number[23]. Low Hartmann number (high-dissipation) leads to a SH state, where high Hartmann number (low-dissipation) results in a multi-helicity (MH) state with many tearing modes. The simulations are not necessarily meant to assign a casual link between high dissipation and the formation of QSH states in experiment, but they are used to infer the magnetic and flow profiles in experimental QSH states[24, 25]. This will be described briefly at the end of the section.

The Hartmann number, Ha, is a hybrid measure that includes both resistivity and viscosity:

$$Ha = \frac{BL}{\sqrt{\eta\mu}} = \frac{S}{\sqrt{Pm}} \tag{2.7}$$

where B and L are characteristic magnetic field and length scales, η is the electrical resistivity, μ is the viscosity, S is the Lundquist number, and Pm is the magnetic Prandtl number. The Lundquist number was previously defined in Equation 2.2, but can be rewritten in terms of

parameters of interest to simulation settings:

$$S = \frac{\mu_0 L V_A}{\eta} \tag{2.8}$$

where $\nu = \mu/\rho$ is the kinematic viscosity, and $V_A = B/\sqrt{\mu_0 \rho}$ is the Alfvén speed. The magnetic Prandtl number is the ratio of the viscous diffusion rate to the magnetic diffusion rate:

$$Pm = \mu_0 \frac{\nu}{\eta}. \tag{2.9}$$

The role the Hartmann number plays in the plasma evolution can be seen in the re-scaled subset of MHD equations[23]:

$$\frac{\partial \boldsymbol{B}}{\partial \bar{t}} = \nabla \times (\bar{\boldsymbol{V}} \times \boldsymbol{B} - \frac{1}{Ha}\boldsymbol{J}), \tag{2.10}$$

and

$$\frac{1}{Pm}\Big(\frac{\partial \bar{\boldsymbol{V}}}{\partial \bar{t}} + (\bar{\boldsymbol{V}} \cdot \nabla \bar{\boldsymbol{V}}\Big) = \boldsymbol{J} \times \boldsymbol{B} + \frac{1}{Ha}\nabla^2 \bar{\boldsymbol{V}} \tag{2.11}$$

where $\bar{t}$ and $\bar{v}$ are re-scaled using $\bar{t} = \sqrt{\frac{\eta}{\nu}}\frac{1}{\tau_A}t$ and $\bar{V} = \sqrt{\frac{\nu}{\eta}}\frac{1}{V_A}V$. The Hartmann number is the quantity that controls the impact of the dissipative terms on the plasma evolution in the simulations when the scaled inertia on the left side of Equation 2.11 is negligible. Simulations performed with SpeCyl[26] at constant density, zero β at a variety of independent values of viscosity and resistivity show a transition from SH to MH at a Hartmann number of about 2000[23].

SpeCyl simulations, and simulations that will be presented in this thesis, implement a flat isotropic profile for viscosity, but viscosity is quite complex in experiments. It is difficult to know for certain what form of viscosity is dynamically most important, and thus to know

how the Hartmann number scaling used in simulations applies to experiment. Perpendicular Braginskii viscosity is arguably the relevant viscious quantity, since flows in the plasma are expected to be dominantly $\boldsymbol{E} \times \boldsymbol{B}$, and thus perpendicular to the magnetic field. The perpendicular Braginskii viscosity is[27]

$$\nu_\perp = \frac{3 n_i T_i}{10 \rho \omega_{ci}^2 \tau_i} \tag{2.12}$$

where n_i is the ion density, T_i is the ion temperature, $\omega_{ci} = q_i B / m_i$ is the ion gyroradius, and τ_i is the ion collision time. Specifically, in a two-component singly-charged-ion plasma,

$$\tau_i = \frac{12 \pi^{3/2} \epsilon^2 \sqrt{m_i} T_i^{3/2}}{\ln \Lambda e^4 n}. \tag{2.13}$$

Using perpendicular Braginskii viscosity and Spitzer resistivity to estimate the Hartmann number gives values on the order of $Ha = 10^6$, far larger than the transition observed in simulation. This point is illustrated in Figure 2.4. Furthermore, since both perpendicular Braginskii viscosity and Spitzer resistivity decrease with increasing plasma current (electron temperature, ion temperature, and magnetic field increase with plasma current), the expected scaling of the Hartmann number is to increase with increasing plasma current as well, where QSH becomes more prevalent. This is the opposite scaling that is observed in high-dissipation simulations. Parallel Braginskii viscosity scales with increasing temperature, and is orders of magnitude larger than perpendicular viscosity, but, again, the important flow dynamics are perpendicular to the magnetic field. Also, the ion temperatures observed in SHAx plasmas, shown in Appendix B, are cold relative to multiple-helicity plasmas, on the order of 150 eV.

Momentum transport in standard and non-reversed RFP plasmas has been shown to

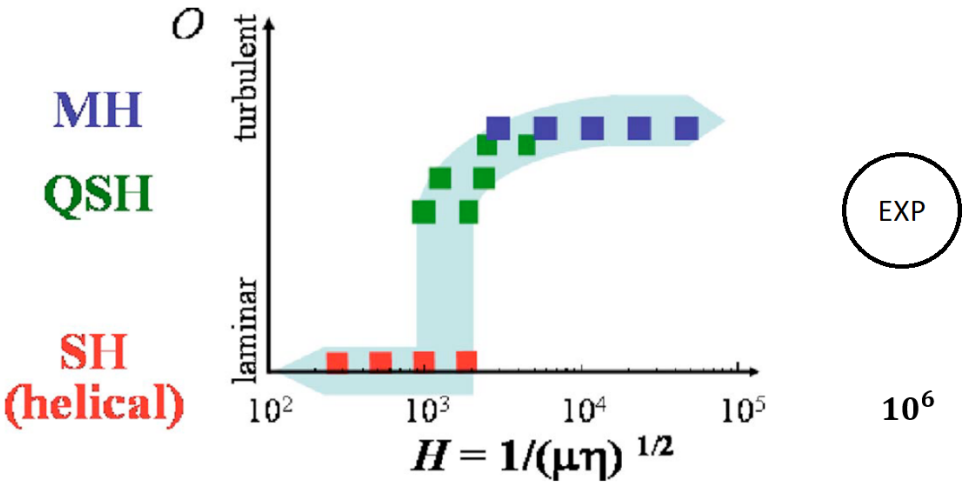

Figure 2.4.: Plot of transition from MH-to-SH as a function of the Hartmann number in simulations run by SpeCyl. Figure is modified from [28]. The experimental regime where QSH is observed is closer to $H = 10^6$. It should be noted that in the Cappello 2006 paper, it is not suggested that the high dissipation transition to an SH state explains the transition in experiment, but that the profiles that develop may be representative of the experimental profiles.

be mostly anomalous, however[29], so there is the possibility that other mechanisms for momentum transport are dominant over collisional Braginskii viscosity. In an alternative momentum transport model, it is suggested that the viscosity in a stochastic plasma scales with the magnetic perturbation strength and speed of sound[30]. This model has recently been experimentally validated in a variety of plasma regimes for MST [31]. The measured perpendicular viscosity in 400 kA non-reversed plasmas with magnetic perturbations $\tilde{b}/B \approx 0.8\%$ is $\nu_{\perp,exp} = 17 \pm 6$ m^2/s, where the expected Braginskii viscosity for these plasma conditions is $\nu_{\perp,Brag} = 0.05 \pm 0.01$ m^2/s, and the anomalous viscosity due to stochasiticity is calculated to be $\nu_{\perp,st} = 19 \pm 5$ m^2/s. Clearly the stochastic viscosity fits better with the measurement, though it is not clear that the viscosity measured by net rotation, as was done in the experiment, is relevant to the mechanisms governing the evolution of fluctuations. Assuming the

model does extend to fluctuations in the plasma, the Hartmann number resulting from the anomalous viscosity is still orders of magnitude larger than the Hartmann number correlated to QSH states in simulations, and the anomalous viscosity still tends to scale inversely with plasma current, and therefore does not explain the increasing tendency to achieve QSH with increasing plasma current. It is possible that the effective viscosity is locally very large in the QSH plasma between the dominant and sub-dominant tearing modes, possibly even including effects from parallel Braginskii viscosity, but no known model for this currently exists. Given that QSH likelihood and persistence is empirically observed to scale with increasing plasma current, we are well-motivated to find another explanation for the onset of QSH.

A feature of the SH simulations is a single helicity flow profile caused by the electrostatic dynamo. In the SH state of the simulations, the plasma column deforms, and a helical electrostatic potential develops[28, 32]. The dominant velocity field in these simulations is a helical flow corresponding to the electrostatic drift $\boldsymbol{V_D} = (\nabla\phi \times \boldsymbol{B})/B^2$. The projection of the helical flow onto a poloidal cross-section of the plasma is shown in Figure 2.5. The helical flow is significant, global, and matches the helicity of the plasma deformation. This model has been used to explain the components of parallel Ohm's law in both RFPs and tokamaks with islands[25]. The prediction of large single helicity flows that are peaked in the core provides an element of the high-viscosity Single Helicity state that can be verified with local flow measurements.

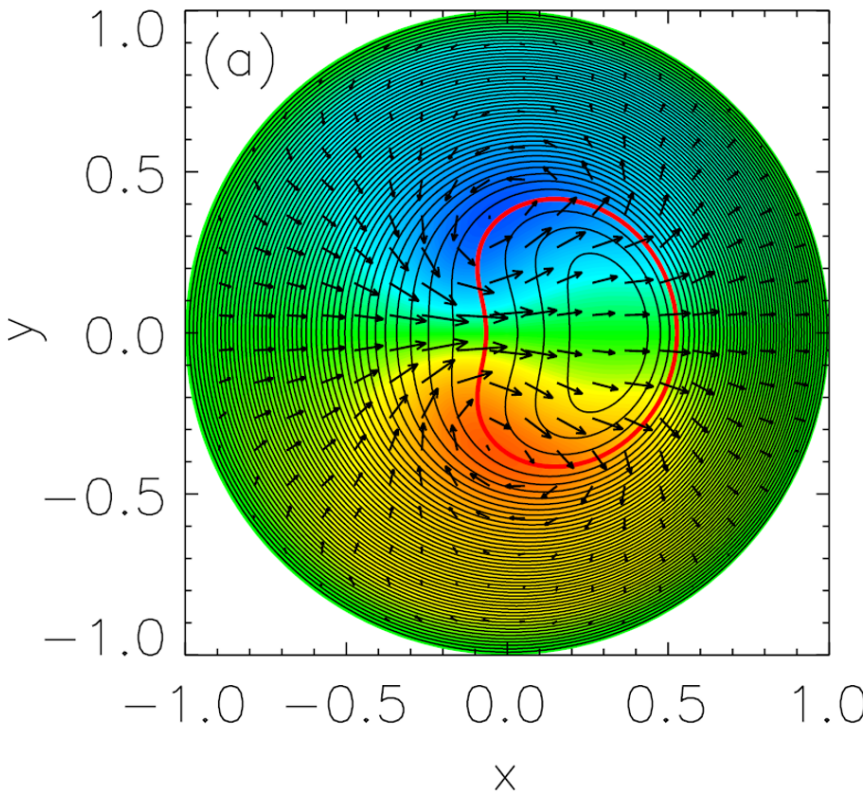

Figure 2.5.: Poloidal cross-section of non-axisymmetric potential (contour colors) and flow (black arrows) in high viscosity specyl simulation reproduced from [32]. Units are normalized to the simulation and are not provided.

2.2.2. Edge magnetic perturbation

Another means to achieve a QSH state in low dissipation simulations is to apply an edge radial magnetic perturbation with the helicity of the desired helical equilibrium[33, 34]. This is motivated by the fact that measurements in RFX-mod indicate a 1.5% - 3.0% radial magnetic field perturbation at the edge of their QSH plasmas. It is hypothesized that this field plays a role in QSH formation. The application of a constant radial magnetic perturbation at the plasma boundary on the order of 2% of the equilibrium field measured at the edge causes QSH plasmas to appear in low dissipation simulations with experimentally relevant Lundquist numbers, $S = 10^7$. While the perturbation is applied, a helical region of

healed flux surfaces forms. The sub-dominant tearing mode amplitudes are reduced within the healed region, similar to what is observed in experiments.

Furthermore, the application of a perturbed magnetic field boundary condition with the same helicity as a sub-dominant tearing mode can cause that mode to become the dominant mode in a QSH plasma[33]. Non-dominant tearing mode QSH states have been achieved experimentally using the application of edge magnetic perturbations as well[35]. Not only was the applied perturbation observed to be the dominant QSH mode, but a reduction of magnetic chaos and a transport barrier was also observed. The states do not, however, persist when the external perturbation is removed, which is not the case with naturally occurring QSH that has the helicity of the dominant tearing mode.

MST has a thick conducting shell that prevents large radial error fields from arising. The largest error fields exist at the poloidal cut in the shell, but it is surrounded by a set of error correction coils keep $\tilde{b}_r$ small. It will be shown later that the local radial magnetic field measured at this poloidal cut is less than 10 G (less than 0.5% of the edge magnetic field). The amplitudes of the n toroidal modes that would describe the local field would be even smaller than this. The error field suppressing attributes of MST make it unlikely that it is the primary cause of QSH onset and sustainment in MST.

2.2.3. Shear suppression of sub-dominant tearing modes

Another paradigm suggested for the cause of the QSH state is through the decoupling of dominant and sub-dominant tearing modes by magnetic or flow shear[36]. Unlike viscosity, the strength of the shear is expected to scale with increasing Lundquist number, thus increasing the likelihood of obtaining a QSH state with increasing plasma current.

Strong shear generally causes a reduction in non-linear energy transfer in plasma tur-

bulence by breaking apart eddies before they can transport material away from the inner plasma, thus reducing the correlation length of turbulent eddies in the shear-wise direction, shown in Figure 2.6. For example, strong poloidal flow shear is the cause for turbulent transport suppression seen in the L to H transition in tokamaks [**?** 37]. Magnetic structures are also subject to turbulence through Aflvén waves. The same mechanism of shear suppression of turbulence is possible through shear in the magnetic field [38].

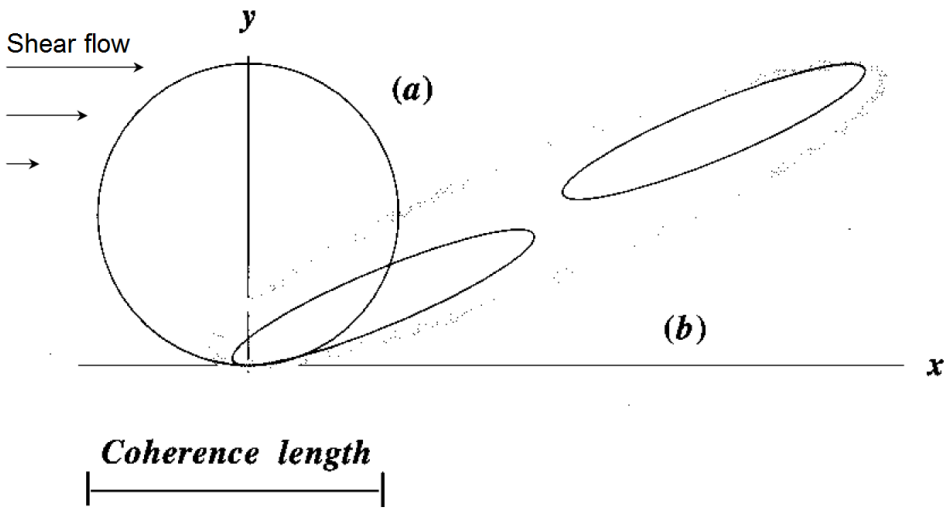

Figure 2.6.: Eddies in a.) unsheared and b.) sheared systems. Shearing in the binormal direction (x) reduces the coherence in radial (y) direction. For a tearing mode, the x direction best describes the helical direction $\chi = m\theta - n\phi$. Adapted from [39] Fig 1.

For shear suppression to occur, the shear strain rate, τ_s^{-1} must be greater than the eddy turnover rate, τ_e^{-1}:

$$\tau_s^{-1} > \tau_e^{-1}. \tag{2.14}$$

The coherence time is generally the time it takes for the eddy to turnover once, the inverse of the eddy turnover rate. It is defined as

$$\tau_e = \frac{\delta x}{u} \tag{2.15}$$

where δx is the coherence length, and u is the velocity in the shear direction. The time it takes to travel that same coherence length due to differential advection is

$$\tau_s = \frac{\delta x}{\delta y \, du/dy} \tag{2.16}$$

where δy is the shear-wise extent of the eddy. When the shear strain rate is greater than the eddy turnover rate, the correlation length in the shear wise (y) direction is reduced compared to the unsheared system, which is the reason for the reduced turbulent transport. Combining Equation 2.16 and Equation 2.15 into Equation 2.14 gives a threshold criterion for shear suppression of turbulence:

$$\frac{u}{\delta y} < \frac{du}{dy} \tag{2.17}$$

In fusion plasma systems, the x direction is typically the direction binormal to the magnetic field and y is in the radial direction. Since x is an angular coordinate in a toroidal system, u is an angular velocity.

The model proposed by Kim and Terry[36] treats tearing modes like turbulent eddies in a cylindrical reduced MHD system. The island width is analogous to the coherence length of an eddy where overlapping islands tend to cause increased transport through the stochasitization of the magnetic field. Sufficient shear would decrease the correlation of the "eddies" such that the coupling is reduced. Between the dominant and sub-dominant fluctuations, a radial boundary layer will form in which fluctuation amplitudes are strongly damped. It is the shear in the dominant tearing mode magnetic or flow field that causes de-correlation with other higher n, sub-dominant tearing mode fluctuations.

The interaction between dominant and sub-dominant modes can be further generalized

and cast as a heuristic predator prey model[40]:

$$\frac{\partial D}{\partial t} = Q_D - \frac{\sigma_1 S^2 + \sigma_2 S D}{\gamma' + a\Omega'} + \alpha_D D, \tag{2.18}$$

$$\frac{\partial S}{\partial t} = \frac{\sigma_2 D S + \sigma_1^{'} D^2 +}{\gamma' + a\Omega'} + \alpha_S S - \beta S^2 \tag{2.19}$$

where D is the dominant mode energy, S is the subdominant mode energy, Q_D is the ohmic drive, α_D is the linear forcing, α_S is the resistive dissipation, β is the coefficient for intra-subdominant mode losses, σ_1, $\sigma_1^{'}$, and σ_2 are the nonlinear coupling coefficients, and the denominator $\gamma' + a\Omega'$ is the shear of the dominant mode. An analysis of the applicable parameter space for the parameters in the predator-prey model to achieve QSH are reviewed in McKinney et al., 2017[41]. By adjusting the shear parameter used in the predator prey model to increasingly large values, the behavior of the analytic system can switch from multi-helicity to a limit cycle QSH, and eventually to steady-state single-helicity. The model includes the predicted response in the electron thermal confinement properties of QSH. Specifically, oscillations in the dominant and secondary mode amplitudes are linked to oscillations in electron temperature, with relative amplitudes and phasing predicted by the theory that agree with previous experimental measurements [42].

For non-reversed plasmas in MST, the magnetic or velocity shear profile of the $(m, n) = (1, 5)$ dominant tearing mode is proposed to prevent energy transfer to the $n > 5$ tearing modes. The projection of the sub-dominant tearing modes on the the helical reference frame of the dominant island is illustrated in Figure 2.7. This is the same concept shown in Figure 2.6, but in the reference frame of an island.

The shear metrics presented are the radial shear in the angular velocity and magnetic field. For an angular velocity, the threshold criterion for shear suppression of turbulence

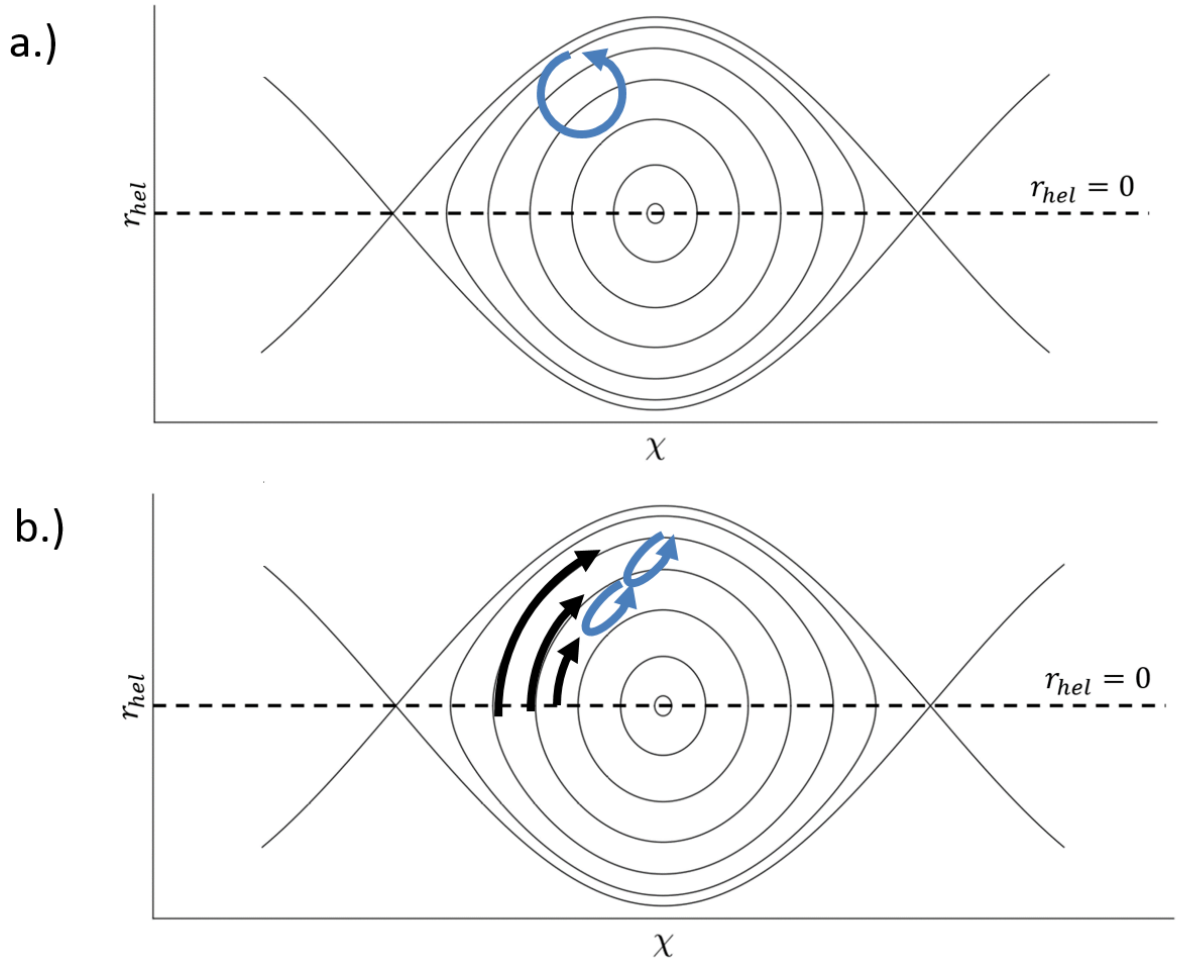

Figure 2.7.: Conceptual illustration of a sub-dominant tearing mode as an "eddy" in the frame of reference the dominant tearing mode island a.) without shear and b.) with shear. The helical angle is $\chi = m\theta + n\phi$, with the m and n modes of the dominant tearing mode, and $r_{hel} = r - r_s$, where r_s is the radial location of the dominant tearing mode rational surface. The blue circles represent the sub-dominant eddies, and the black arrows are the sheared velocity or magnetic field.

given in Equation 2.17 becomes

$$\frac{\partial}{\partial r_{hel}} \frac{\tilde{V}_{\mathrm{Dom}}}{r_{hel}} > \frac{\tilde{V}_{\mathrm{Sub}}}{w^2_{\mathrm{Sub}}} \tag{2.20}$$

and

$$\frac{\partial}{\partial r_{hel}} \frac{\tilde{B}_{\mathrm{Dom}}}{r_{hel}} > \frac{\tilde{B}_{\mathrm{Sub}}}{w^2_{\mathrm{Sub}}} \tag{2.21}$$

for the velocity and magnetic fields respectively. This states that the scale size of the angular shear necessary to suppress turbulence is on the order of the adjacent sub-dominant tearing mode velocity, $\widetilde{V}_{\text{sub}}$, or magnetic field, $\widetilde{B}_{\text{sub}}$, over the square of the length scale of the coherent structure, which is the sub-dominant tearing mode island width, w_{sub}. The radial coordinate used is $r_hel = r - r_s$, where r_s is the dominant tearing mode rational surface. The tearing mode velocity has components in the radial and helical direction, $V_{Dom} = V_r\hat{r} + V_\chi\hat{\chi}$, where $\chi = m\theta + n\phi$, with the m and n mode numbers matching the dominant tearing mode.

The typical velocity of the sub-dominant tearing mode is unknown for a plasma in the SHAx state. David Ennis calculated the velocity correlated with sub-dominant tearing mode fluctuations on the order of 1 km/s in reversed, 400 kA plasmas[43], with tearing island widths between 5 and 10 cm, leading to an angular velocity shear rate on the order of 100's of km/m^{2}s. Alternatively, it has been suggested that shear flows on the order of the V_A/a, the Alfvén speed over the system size are necessary to affect tearing mode structure[40]. The Alfven speed in 500 kA plasma from which data in this thesis is collected is on the order of 10^3 km/s, which would require helical angular shear rates on the order of 1000's of km/m^{2}s. Future analysis will consider the measured tearing mode velocities as opposed to the Alfvén speed when considering the velocity shear threshold.

The theoretical framework for shear suppression is a simplified model. For example, it does not include any effects from three-wave coupling through $m = 0$ mode or geometrical effects. As a heuristic model, however, it does predict internal transport barriers and predicts the increased persistence and strength of the QSH state with increasing plasma current, as is empirically observed in experiments. It can be used as a framework from which to consider results from a magnetic and flow characterization of the QSH state.

2.3. Previous measurements of flow in QSH

The flow in rotating, unsaturated QSH state has been measured both with line-integrated spectroscopy and with local CHERS measurements. There have been no previous measurements of local flows in a saturated QSH state, however. As such, previous measurements cannot help us understand how the helical equilibrium is sustained, or if equilibrium flows look different than flows measured when the mode is growing. Previous measurements relied on the rotation of the QSH state past the diagnostic to correlate the velocity signal with the magnetic phase of the mode in time. Due to the locking of QSH state prior to saturation, this technique is inapplicable for measuring the saturated QSH state, and a new correlation technique must be implemented, which will be covered in Section 3.3. The following section will review measurements of the rotating QSH state.

2.3.1. line-integrated, passive spectroscopic flow measurements

In a rotating $(m, n) = (1, 6)$ unsaturated QSH state, ensembles of line-integrated measurements of carbon impurity emission were taken at various impact parameters[24] on MST. The signal was correlated with the $n = 6$ magnetic mode amplitude measured from the toroidal magnetics array at the wall to find the mode-resolved, line-integrated velocity fluctuations. The local poloidal velocity was estimated by fitting line-integrated measurements to a flow model based on a global $m = 1$, $n = 6$ velocity profile simulated in high-dissipation MHD simulations. Carbon impurity atoms are fully stripped of electrons in MST's core, so the radial emission profile of the carbon impurities is hollow, preventing any strong velocity profile in the core from being observed. More generally, the velocity measurement will be weighted by the detailed emission profile itself, as more light will come from specific regions in the plasma than others[24].

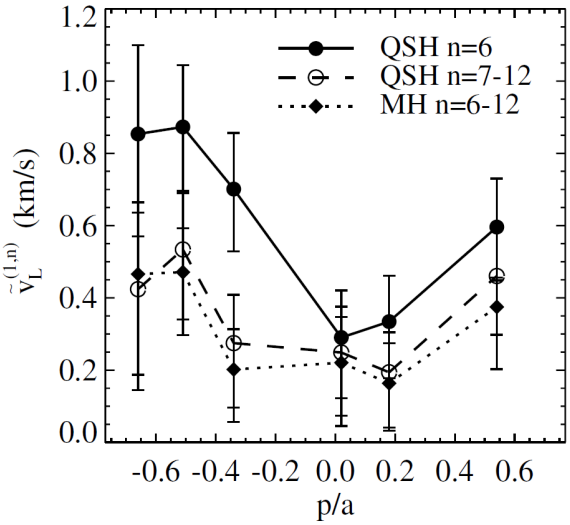

Figure 2.8.: line-integrated velocity perturbations correlating to different magnetic modes, reported in Piovesan et al. (2004)[24].

The same technique was used on RFX using 18 passive spectroscopic chords[44]. Temporal variation in the velocity was observed which correlated to the rotation of the $(m, n) = (1, -7)$ helical state. The data was used to fit to different helical flow models in order to back out the radial profile of a single helicity perturbed flow. Since line-integrated data depends heavily on fitting to a model, the possibility remains that a different model fits the data better. As noted previously, the line-integrated velocity measurements are weighted by the emissivity profile of the carbon species being measured, and is less sensitive to the peaked velocity in the core predicted by high-dissipation simulations because the emissivity is significantly lower there. CHERS measurements can provide local velocity information that is not line integrated over the entire plasma, and does not rely on the peaking of the charge state density profile for radial localization. These measurements will be presented next.

2.3.2. Local, active CHERS flow measurements

On MST, CHERS has successfully been used to measure poloidal velocity fluctuations correlated to magnetic perturbations with radial resolution [43]. The QSH states occurred in reversed plasmas, when the $n = 6$ tearing mode grew large in time before a sawtooth event occurred. It is unlikely that the $n = 6$ mode ever saturated as the $n = 5$ does in the non-reversed state shown in Figure 2.1.

The QSH case, reproduced in Figure 2.9, has an $n = 6$ poloidal velocity profile that is strongest between $0.2 < \rho/a < 0.4$, and weaker at $\rho = 0.55$, where the the contribution from many other $n > 6$ modes grows large. The large contribution from other toroidal modes to the CHERS velocity signal at $\rho/a = 0.58$ was observed in both QSH and MH cases. A total of 200-300 shots were used to correlate the fluctuating velocity signal to the fluctuating magnetic signal at the edge. Both the multi-helicity case and the QSH case had a hollow velocity profile. This is in contrast to the peaked velocity profile observed in high-dissipation simulations, and used to fit to line-integrated measurements.

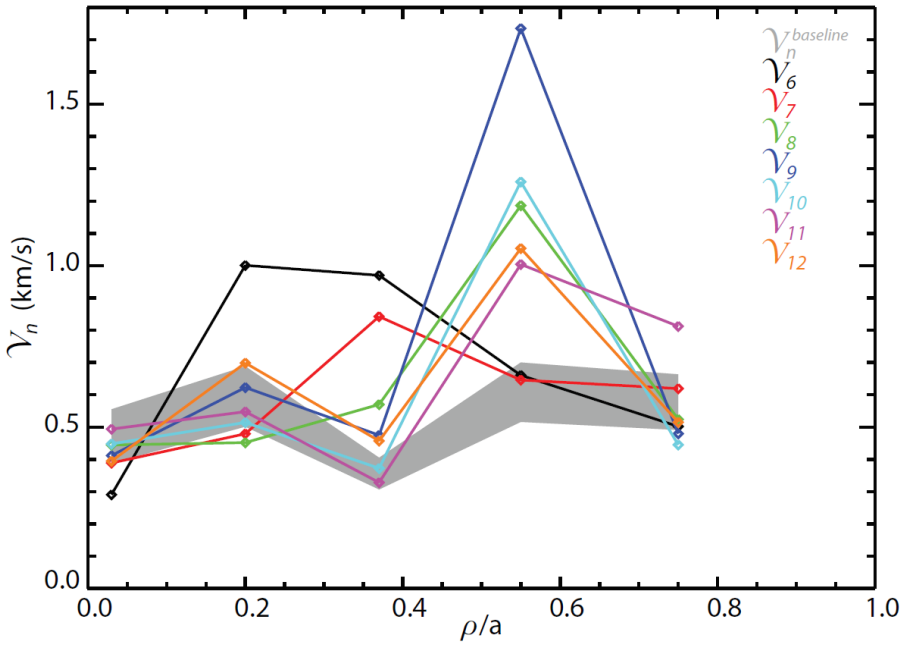

Figure 2.9.: Velocity pseudo n-spectrum of impurity ion poloidal velocity fluctuations measured during QSH plasma periods, reproduced from David Ennis' 2008 thesis. The gray bar represents the noise floor for the analysis technique used.

2.4. Summary

Three possibilities for producing a SHAx state are predicted through computation and theory: mode decoupling through high-dissipation, the presence of edge boundary perturbations, and mode decoupling through magnetic or flow shear.

Past work indicates that momentum transport in MST is dominantly anomalous, but still too small to match the Hartmann number where the transition to QSH and SH states is observed in simulations. The edge magnetic perturbation amplitude in MST is small, and is not expected to be a cause for the spontaneous onset or sustainment of QSH. The strength of the shear in the dominant tearing mode can cause a decoupling of the energy transfer to other sub-dominant modes, and is expected to scale with plasma current. There is currently no experimental measurement for the velocity and magnetic shear of the dominant

tearing mode. The velocity measurements provided in the following chapters can be used as a critical comparison for different simulation parameters, including viscosity. Subsequent shear measurements from the experimental flow profiles provide constraints for a predator-prey model of the QSH/SHAx state.

A means of comparing experimental data to the dissipation and shear suppression models for obtaining QSH is to measure the flow profiles. high-dissipation simulations see strong single helicity flows that are peaked in the core, and shear suppression based on flow shear requires that the flow shear be above the eddy turnover time of the sub-dominant tearing modes. Previous measurements of velocity in QSH were line-integrated and not sensitive to the plasma core, or they were local measurements limited to rotating, unsaturated QSH modes. No flow measurements exist in the saturated SHAx state. The following two chapters will describe the necessary tools to obtain toroidal resolved flow measurements in the saturated SHAx state in MST, and then present the flow measurements themselves.

References

[1] B. Chapman, *Fluctuation Reduction and Enhanced Confinement in the MST Reversed-Field Pinch*. PhD thesis, University of Wisconsin - Madison, 1997.

[2] Y. Hirano, Y. Maejima, T. Shimada, Y. Yagi, S. Sekine, I. Hirota, H. Sakakita, T. Baig, G. Serianni, and H. Ji, "Improved high theta mode and dynamo activity in a Reversed Field Pinch on TPE-1RM20," in *Proceedings of Contributed Papers, 16th IAEA Fusion Energy Conference*, (Vienna), pp. 95–105, 1996.

[3] P. Nordlund and S. Mazur, "Nonlinear dynamics of kink-tearing modes and their inter-

action with the current profiles in a reversed-field pinch," *Physics of Plasmas*, vol. 1, no. 12, pp. 4032–4042, 1994.

[4] L. Marrelli, P. Martin, G. Spizzo, P. Franz, B. E. Chapman, D. Craig, J. S. Sarff, T. M. Biewer, S. C. Prager, and J. C. Reardon, "Quasi-single helicity spectra in the Madison Symmetric Torus," *Physics of Plasmas*, vol. 9, no. 7, pp. 2868–2871, 2002.

[5] D. F. Escande, R. Paccagnella, S. Capello, C. Marchetto, and F. D'Angelo, "Chaos healing by separatrix disappearance and quasisingle helicity states of the reversed field pinch," *Physical Review Letters*, vol. 85, no. 15, pp. 3169–3172, 2000.

[6] Finn J, Nebel R, and Bathke C, "Single and multiple helicity Ohmic states in reversed field pinches," *Physics of Plasmas*, vol. 4, no. 5, pp. 1262–1279, 1992.

[7] S. Cappello and R. Paccagnella, "Nonlinear plasma evolution and sustainment in the reversed field pinch," *Physics of Fluids B*, vol. 4, no. 3, pp. 611–618, 1992.

[8] M. E. Puiatti, A. Alfier, F. Auriemma, S. Cappello, L. Carraro, R. Cavazzana, S. Dal Bello, A. Fassina, D. F. Escande, P. Franz, M. Gobbin, P. Innocente, R. Lorenzini, L. Marrelli, P. Martin, P. Piovesan, I. Predebon, F. Sattin, G. Spizzo, D. Terranova, M. Valisa, B. Zaniol, L. Zanotto, M. Zuin, M. Agostini, V. Antoni, L. Apolloni, M. Baruzzo, T. Bolzonella, D. Bonfiglio, F. Bonomo, A. Boozer, M. Brombin, A. Canton, R. Delogu, G. De Masi, E. Gaio, E. Gazza, L. Giudicotti, L. Grando, S. C. Guo, G. Manduchi, G. Marchiori, E. Martines, S. Martini, S. Menmuir, B. Momo, M. Moresco, S. Munaretto, L. Novello, R. Paccagnella, R. Pasqualotto, R. Piovan, L. Piron, A. Pizzimenti, N. Pomphrey, P. Scarin, G. Serianni, E. Spada, A. Soppelsa, S. Spagnolo, M. Spolaore, C. Taliercio, N. Vianello, A. Zamengo, and P. Zanca, "Helical equilibria and magnetic structures in the reversed field pinch and analogies to the toka-

mak and stellarator," *Plasma Physics and Controlled Fusion*, vol. 51, no. 12, p. 124031, 2009.

[9] L. A. Morton, W. C. Young, C. C. Hegna, E. Parke, J. A. Reusch, and D. J. Den Hartog, "Electron thermal confinement in a partially stochastic magnetic structure," *Physics of Plasmas*, vol. 25, p. 042306, 4 2018.

[10] P. Martin, L. Marrelli, A. Alfier, F. Bonomo, D. F. Escande, P. Franz, L. Frassinetti, M. Gobbin, R. Pasqualotto, P. Piovesan, and D. Terranova, "A new paradigm for RFP magnetic self-organization: Results and challenges," *Plasma Physics and Controlled Fusion*, vol. 49, pp. A177–A193, 5 2007.

[11] R. Lorenzini, D. Terranova, A. Alfier, P. Innocente, E. Martines, R. Pasqualotto, and P. Zanca, "Single-helical-axis states in reversed-field-pinch plasmas," *Physical Review Letters*, vol. 101, no. 2, p. 025005, 2008.

[12] S. Munaretto, B. E. Chapman, M. D. Nornberg, J. Boguski, A. M. DuBois, A. F. Almagri, and J. S. Sarff, "Effect of resonant magnetic perturbations on three dimensional equilibria in the Madison Symmetric Torus reversed-field pinch," *Physics of Plasmas*, vol. 23, no. 3, p. 056104, 2016.

[13] P. Zanca and D. Terranova, "Reconstruction of the magnetic perturbation in a toroidal reversed field pinch," in *Plasma Physics and Controlled Fusion*, vol. 46, pp. 1115–1141, 7 2004.

[14] F. Auriemma, P. Zanca, W. F. Bergerson, B. E. Chapman, W. X. Ding, D. L. Brower, P. Franz, P. Innocente, R. Lorenzini, B. Momo, and D. Terranova, "Magnetic reconstruction of nonaxisymmetric quasi-single-helicity configurations in the Madison Symmetric Torus," *Plasma Physics and Controlled Fusion*, vol. 53, no. 10, p. 105006, 2011.

[15] W. F. Bergerson, F. Auriemma, B. E. Chapman, W. X. Ding, P. Zanca, D. L. Brower,

P. Innocente, L. Lin, R. Lorenzini, E. Martines, B. Momo, J. S. Sarff, and D. Terranova, "Bifurcation to 3D helical magnetic equilibrium in an axisymmetric toroidal device," *Physical Review Letters*, vol. 107, no. 25, p. 255001, 2011.

[16] M. Gobbin, D. Bonfiglio, D. F. Escande, A. Fassina, L. Marrelli, A. Alfier, E. Martines, B. Momo, and D. Terranova, "Vanishing magnetic shear and electron transport barriers in the RFX-mod reversed field pinch," *Physical Review Letters*, vol. 106, p. 025001, 1 2011.

[17] I. Predebon, B. Momo, D. Terranova, and P. Innocente, "MHD spectra and coordinate transformations in toroidal systems," *Physics of Plasmas*, vol. 23, p. 092508, 9 2016.

[18] D. Terranova, L. Marrelli, J. D. Hanson, S. P. Hirshman, M. Cianciosa, and P. Franz, "Helical equilibrium reconstruction with V3FIT in the RFX-mod Reversed Field Pinch," *Nuclear Fusion*, vol. 53, no. 11, p. 113014, 2013.

[19] R. Lorenzini, M. Agostini, A. Alfier, V. Antoni, L. Apolloni, F. Auriemma, O. Barana, M. Baruzzo, P. Bettini, D. Bonfiglio, T. Bolzonella, F. Bonomo, M. Brombin, A. Buffa, A. Canton, S. Cappello, L. Carraro, R. Cavazzana, G. Chitarin, S. Dal Bello, A. De Lorenzi, G. De Masi, D. F. Escande, A. Fassina, P. Franz, E. Gaio, E. Gazza, L. Giudicotti, F. Gnesotto, M. Gobbin, L. Grando, S. C. Guo, P. Innocente, A. Luchetta, G. Manduchi, G. Marchiori, D. Marcuzzi, L. Marrelli, P. Martin, S. Martini, E. Martines, F. Milani, M. Moresco, L. Novello, S. Ortolani, R. Paccagnella, R. Pasqualotto, S. Peruzzo, R. Piovan, P. Piovesan, L. Piron, A. Pizzimenti, N. Pomaro, I. Predebon, M. E. Puiatti, G. Rostagni, F. Sattin, P. Scarin, G. Serianni, P. Sonato, E. Spada, A. Soppelsa, S. Spagnolo, G. Spizzo, M. Spolaore, C. Taliercio, D. Terranova, V. Toigo, M. Valisa, P. Veltri, N. Vianello, P. Zaccaria, B. Zaniol, L. Zanotto, E. Zilli, and M. Zuin, "Improvement of the magnetic configuration in the reversed field pinch through succes-

sive bifurcations," *Physics of Plasmas*, vol. 16, no. 5, p. 056109, 2009.

[20] R. Lorenzini, F. Auriemma, A. Fassina, E. Martines, D. Terranova, and F. Sattin, "Internal Transport Barrier Broadening through Subdominant Mode Stabilization in Reversed Field Pinch Plasmas," *Physical Review Letters*, vol. 116, no. 18, p. 185002, 2016.

[21] D. Biskamp, *Nonlinear Magnetohydrodynamics*. Cambridge: Cambridge University Press, 1st ed., 1997.

[22] Schnack Dalton, *Lectures in Magnetohydrodynamics*. New York: Springer, 2009.

[23] S. Cappello and D. F. Escande, "Bifurcation in viscoresistive MHD: the Hartmann number and the reversed field pinch," *Physical Review Letters*, vol. 85, no. 18, pp. 3838–3841, 2000.

[24] P. Piovesan, D. Craig, L. Marrelli, S. Cappello, and P. Martin, "Measurements of the MHD dynamo in the quasi-single-helicity reversed-field pinch," *Physical Review Letters*, vol. 93, no. 23, p. 235001, 2004.

[25] P. Piovesan, D. Bonfiglio, M. Cianciosa, T. C. Luce, N. Z. Taylor, D. Terranova, F. Turco, R. S. Wilcox, A. Wingen, S. Cappello, C. Chrystal, D. F. Escande, C. T. Holcomb, L. Marrelli, C. Paz-Soldan, L. Piron, I. Predebon, and B. Zaniol, "Role of a continuous MHD dynamo in the formation of 3D equilibria in fusion plasmas," *Nuclear Fusion*, vol. 57, no. 7, p. 076014, 2017.

[26] S. Cappello and D. Biskamp, "Reconnection processes and scaling laws in reversed field pinch MHD," *Nucl. Fusion*, vol. 36, no. 5, p. 571, 1996.

[27] S. Braginskii, "Transport Processess in a Plasma," in *Reviews of Plasma Physics*, vol. 1, pp. 205–311, Consultants Bureau, New York, NY, USA, 1965.

[28] S. Cappello, D. Bonfiglio, and D. F. Escande, "Magnetohydrodynamic dynamo in reversed field pinch plasmas: Electrostatic drift nature of the dynamo velocity field," *Physics of Plasmas*, vol. 13, no. 5, p. 056102, 2006.

[29] A. F. Almagri, J. T. Chapman, C. S. Chiang, D. Craig, D. J. Den Hartog, C. C. Hegna, and S. C. Prager, "Momentum transport and flow damping in the reversed-field pinch plasma," *Physics of Plasmas*, vol. 5, no. 11, pp. 3982–3985, 1998.

[30] J. M. Finn, P. N. Guzdar, and A. A. Chernikov, "Particle transport and rotation damping due to stochastic magnetic field lines," *Physics of Fluids B*, vol. 4, no. 5, pp. 1152–1155, 1992.

[31] R. Fridström, B. E. Chapman, A. F. Almagri, L. Frassinetti, P. R. Brunsell, T. Nishizawa, and J. S. Sarff, "Dependence of Perpendicular Viscosity on Magnetic Fluctuations in a Stochastic Topology," *Physical Review Letters*, vol. 120, p. 225002, 5 2018.

[32] S. Cappello, D. Bonfiglio, D. F. Escande, S. C. Guo, I. Predebon, F. Sattin, M. Veranda, P. Zanca, C. Angioni, L. Chacón, J. Q. Dong, X. Garbet, and S. F. Liu, "Equilibrium and transport for quasi-helical reversed field pinches," *Nuclear Fusion*, vol. 51, no. 10, p. 103012, 2011.

[33] M. Veranda, D. Bonfiglio, S. Cappello, L. Chacón, and D. F. Escande, "Impact of helical boundary conditions on nonlinear 3D magnetohydrodynamic simulations of reversed-field pinch," *Plasma Physics and Controlled Fusion*, vol. 55, p. 074015, 7 2013.

[34] D. Bonfiglio, M. Veranda, S. Cappello, D. F. Escande, and L. Chacón, "Experimental-like helical self-organization in reversed-field pinch modeling," *Physical Review Letters*, vol. 111, no. 8, p. 085002, 2013.

[35] M. Veranda, D. Bonfiglio, S. Cappello, D. F. Escande, F. Auriemma, D. Borgogno,

L. Chacón, A. Fassina, P. Franz, M. Gobbin, D. Grasso, and M. E. Puiatti, "Magneto-hydrodynamics modelling successfully predicts new helical states in reversed-field pinch fusion plasmas," *Nuclear Fusion*, vol. 57, p. 116029, 8 2017.

[36] J. H. Kim and P. W. Terry, "Magnetic turbulence suppression by a helical mode in a cylindrical geometry," *Physics of Plasmas*, vol. 19, no. 12, p. 122304, 2012.

[37] H. Biglari, P. H. Diamond, and P. W. Terry, "Influence of sheared poloidal rotation on edge turbulence," *Physics of Fluids B*, vol. 2, no. 1, pp. 1–4, 1990.

[38] P. W. Terry and K. W. Smith, "Coherence and Intermittency of Electron Density in Small Scale Interstellar Turbulence," *The Astrophysical Journal*, vol. 665, no. 1, pp. 402–415, 2007.

[39] P. W. Terry, "Suppression of turbulence and transport by sheared flow," *Reviews of Modern Physics*, vol. 72, pp. 109–165, 1 2000.

[40] P. W. Terry and G. G. Whelan, "Time-dependent behavior in a transport-barrier model for the quasi-single helcity state," *Plasma Physics and Controlled Fusion*, vol. 56, no. 9, p. 094002, 2014.

[41] I. J. McKinney and P. W. Terry, "Thermal transport dynamics in the quasi-single helicity state," *Physics of Plasmas*, vol. 24, no. 6, p. 062303, 2017.

[42] P. Franz, M. Gobbin, L. Marrelli, A. Ruzzon, F. Bonomo, A. Fassina, E. Martines, and G. Spizzo, "Experimental investigation of electron temperature dynamics of helical states in the RFX-Mod reversed field pinch," *Nuclear Fusion*, vol. 53, no. 5, p. 053011, 2013.

[43] D. A. Ennis, D. Craig, S. Gangadhara, J. K. Anderson, D. J. Den Hartog, F. Ebrahimi, G. Fiksel, and S. C. Prager, "Local measurements of tearing mode flows and the magne-

tohydrodynamic dynamo in the Madison Symmetric Torus reversed-field pinch," *Physics of Plasmas*, vol. 17, no. 8, p. 082102, 2010.

[44] F. Bonomo, D. Bonfiglio, P. Piovesan, L. Piron, B. Zaniol, S. Cappello, L. Carraro, R. Cavazzana, M. Gobbin, L. Marrelli, E. Martines, B. Momo, M. Puiatti, and M. Valisa, "Flow measurements and modelling in helical RFX-mod equilibria," *Nuclear Fusion*, vol. 51, p. 123007, 12 2011.

3. Tools for SHAx Characterization

In this chapter, we will discuss key tools used to characterize the SHAx state. In order to probe the detailed velocity structures in the SHAx state, two diagnostics are key: the toroidal magnetic array, a CHarge Exchnage Recombination Spectroscopy (CHERS) diagnostic, as well as one control system: the resonant magnetic perturbation. The computational tool, V3FIT, is used to provide a reconstruction of nested MHD flux surfaces of the SHAx state using a variety of diagnostic inputs as constraints.

3.1. Magnetics arrays

A critical diagnostic for all MST experiments are the arrays of magnetic diagnostic coils (also known as Mirnov coils) at the plasma boundary. While the full magnetic mode profile in a plasma is not measured, the mode amplitude measured at the wall allows comparison of the perturbation levels between modes and between plasmas discharges. An excellent, in depth review of the hardware setup exists in J. Koliner's thesis[1]. The measurement of magnetic fields, B, at the wall is obtained using Faraday's law of induction and integrating the emf ϵ produced in a loop of wire encompassing a changing magnetic flux, Φ:

$$\epsilon = -\frac{\partial \Phi}{\partial t} \tag{3.1}$$

$$B(t) = -\frac{1}{A}\int \epsilon \, dt \tag{3.2}$$

where A is the area of the coil. Only the magnetic field perpendicular to the area encompassed by the wire is measured this way, so three coils are needed at any one location to obtain the full magnetic field vector at that location. There are four magnetics arrays on MST. A toroidal array at $\theta_{MST} = 241$ deg, and three poloidal arrays at $\phi_{MST} = 0$ deg, $\phi_{MST} = 155$ deg., and $\phi_{MST} = 177$ deg, as represented in Figure 3.1. Only the toroidal array and the poloidal gap array at $\phi_{MST} = 0$ are used in this thesis. The subscript MST here refers to the machine coordinates used by the MST group. The toroidal array consists of evenly spaced sets of three pick-up coils which measure $\widehat{b}_r$, $\widehat{b}_\theta$, and $\widehat{b}_\phi$. Sixty-four B_ϕ signals and thirty-two B_θ signals are digitized on a 200 kHz timescale and Fourier decomposed to provide mode amplitudes $\tilde{b}_n$, and phases, δ_n, according to:

$$B(\phi) = \sum_{n=0}^{n=15} \tilde{b}_n \cos\left(n\phi - \delta_n\right) \tag{3.3}$$

where $n = 15$ is the maximum number of modes resolvable for the poloidal magnetic field. The toroidal magnetic field coils are calibrated against a vacuum magnetic field applied prior to each plasma shot. The poloidal magnetic field is calibrated every shot using the time averaged plasma magnetic field from 10-15 ms. The intrinsic rotation of the plasma during this time period is important for the calibration procedure to average out magnetic perturbations present in the plasma. For the 500 kA non-reversed plasma analyzed in this work, it is possible, but rare, for the plasma rotation to halt in the 10-15 ms time-frame. Such discharges are excluded from the dataset.

The poloidal gap magnetics array has 32 b_r and 16 b_θ coils. The radial sensing coils are important for measuring error fields that arise at the poloidal gap also located at $\phi_{MST} = 0$.

The signal is used by the active feedback system to cancel out the error fields. The coils are further used to apply a controlled resonant magnetic perturbation (RMP), which will be discussed later. The b_θ coils are only used in this work as input signals to constrain the V3FIT equilibrium reconstruction.

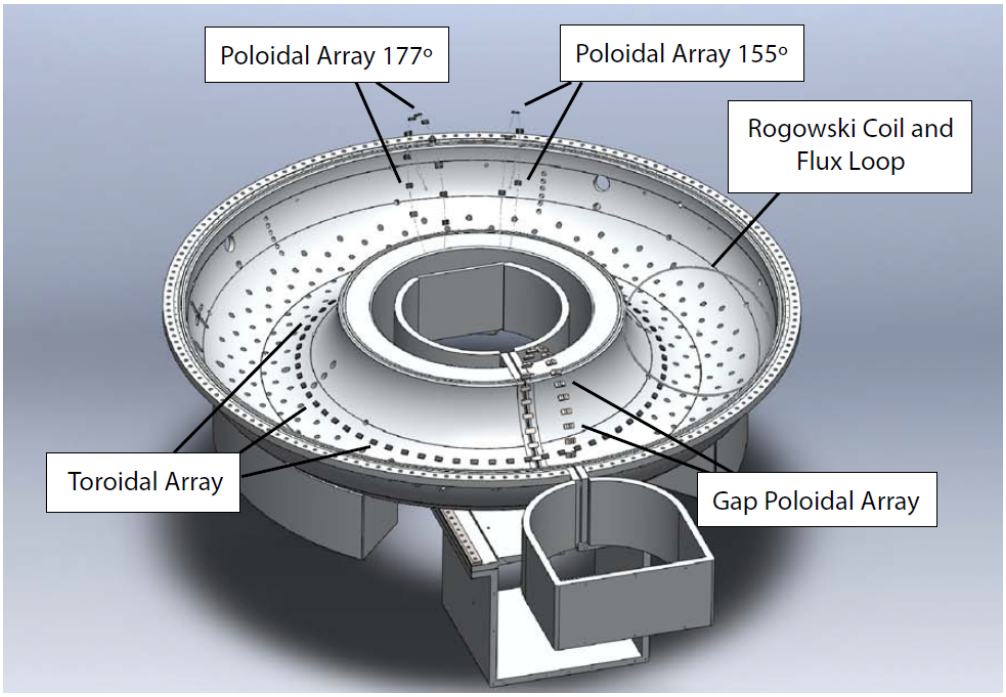

Figure 3.1.: Magnetics arrays on MST, reproduced from [1].

3.2. Charge Exchange Recombination Spectroscopy

3.2.1. Optical spectroscopy background

In order to understand the ion dynamics, the light from line radiation emitted by impurity ions can be analyzed and key parameters such as the density, velocity, and temperature of ions in the plasma can be obtained. Spectroscopy in general is a critical non-invasive diagnostic for plasmas.

Line radiation, the emission of light from an atom due to the transition of electrons between bound states, in a magnetically confined plasma is dominated by electron impact excitation and charge exchange recombination. Electron impact excitation occurs when free electrons impart energy to bound electrons through a collision, raising the bound electron to a higher energy state. Charge exchange occurs when an electron from a neutral atom is donated to an ionized atom. The donated electron is initially in an excited state and quickly de-excites, emitting line radiation whose wavelength depends on the ionization state of the atom. The de-excitation process for both charge exchange and electron impact is on the nanosecond timescale, much faster than any ion dynamics of interest in the plasma. For charge exchange between a fully stripped impurity ion and a neutral particle, for example, this means the line radiation emitted from the donated electron is most representative of the fully stripped impurity ion population, not the lower charge state ion it has become.

The distribution of ionization states of impurity atoms depends on the temperature and density of the plasma. Since the temperature and density in toroidally confined plasmas have a radial profile, so too does the ionization state density of impurity atoms. The core of MST in 500 kA plasma is hot and dense enough that the impurity species tend to be fully ionized. The ionization state, and therefore line radiation associated with that state, tends to peak in certain radially localized regions referred to as emission shells. The bulk plasma species, Deuterium, is fully ionized over most of the plasma, and therefore its emission shell is at the edge of the plasma.

Although optical spectroscopy is inherently a line-integrated measurement, there are two methods of obtaining localized information from the measurement. The first is to determine the radial profiles of the different charge states of impurity atoms through collisional-radiative modelling. This provides an estimate of the location of the emission shell from which most of the light at the wavelength under consideration is being gathered. Without extensive

modelling, the localization is generally limited by the degree of peaking of the radial profile of the specific charge state of interest and the modelling itself requires detailed measurements of the electron temperature and density profiles. The second method is to use a neutral beam injected perpendicular to the optical line of sight to actively provide a local source of charge exchange emission that, when analyzed, provides information specific to the region of plasma located at the intersection of the neutral beam and the optical line-of-sight.

The line radiation emitted from the plasma contains valuable information about the dynamics of the ion species. Electrons transition between bound states at discrete wavelengths, but the emission profile of a collection of ions spreads into a Gaussian shape whose central peak and width depend on the Doppler shift and broadening of the plasma respectively. The emission profile for a single line emission can be described by:

$$L(\lambda) = \frac{I}{\sqrt{2\pi}\sigma}\exp\left(-\frac{(\lambda-\lambda_c)^2}{2\sigma^2}\right) \tag{3.4}$$

where $L(\lambda)$, is the spectral radiance, I is the total radiance, λ_c is the central wavelength, and σ is the spreading parameter. The average velocity of the plasma causes a Doppler shift in the central wavelength according to

$$\lambda_c = \lambda_0(1 - v/c), \tag{3.5}$$

where λ_0 is the un-shifted wavelength of the line radiation under consideration, v is the average velocity of the plasma, and c is the speed of light. The broadening in the emission is caused by random motion of the ions relative to the average velocity, and is related to the

temperature of the plasma according to:

$$\sigma = \sqrt{\frac{kT}{m}}\lambda_c \tag{3.6}$$

where T is the temperature of the ions and m is the mass of the ions. The radiance is related to the number density of the emitting ion species according to:

$$I = n_i n \langle \sigma v \rangle \tag{3.7}$$

where n_i is the ion density, n is the density of the interacting species and $\langle \sigma v \rangle$ is the average interaction cross-section between them (σ is different than the σ denoted in Equation 3.6). For electron impact $n = n_e$, and for charge exchange $n = n_0$, the density of the neutral species.

Due to very strong emission from neutral particles at the edge, it is infeasible to observe charge exchange with the bulk species, deuterium. Instead, the light from impurity ions is analyzed and, for equilibrium characteristics, attributed to the bulk ion species. This is appropriate for the equilibrium flow being studied since the equilibration time is on the order of the ion-ion collision time, which for MST conditions is on the order of 0.2 ms.

3.2.2. The CHERS diagnostic on MST

The spectrometer used for CHERS measurements on MST is a high-throughput, double-grating spectrometer, shown in Figure 3.2. The gratings can rotate to measure wavelengths between 200 nm and 470 nm, but the optics are optimized to measure the carbon C^{+5} 343.383 nm line. It has both high etendue (0.8 mm^{2}sr) and high spectral resolution ($\lambda/\Delta\lambda = 5600$)[2]. The full design details of the spectrometer and previous work done to characterize

the background and charge exchange spectrum at 343.383 nm are well described in theses by David Ennis[3], as well Rich Magee[4], and Takashi Nishizawa[5]. Thirty-two photomultiplier tubes are used to record the light from the exit slit, and their signal is digitized at 1 MHz and filtered at 400 kHz[**?**]. Two fiber optic bundles are coupled to the spectrometer entrance, each taking up half the light collecting area of the spectrometer entrance slit.

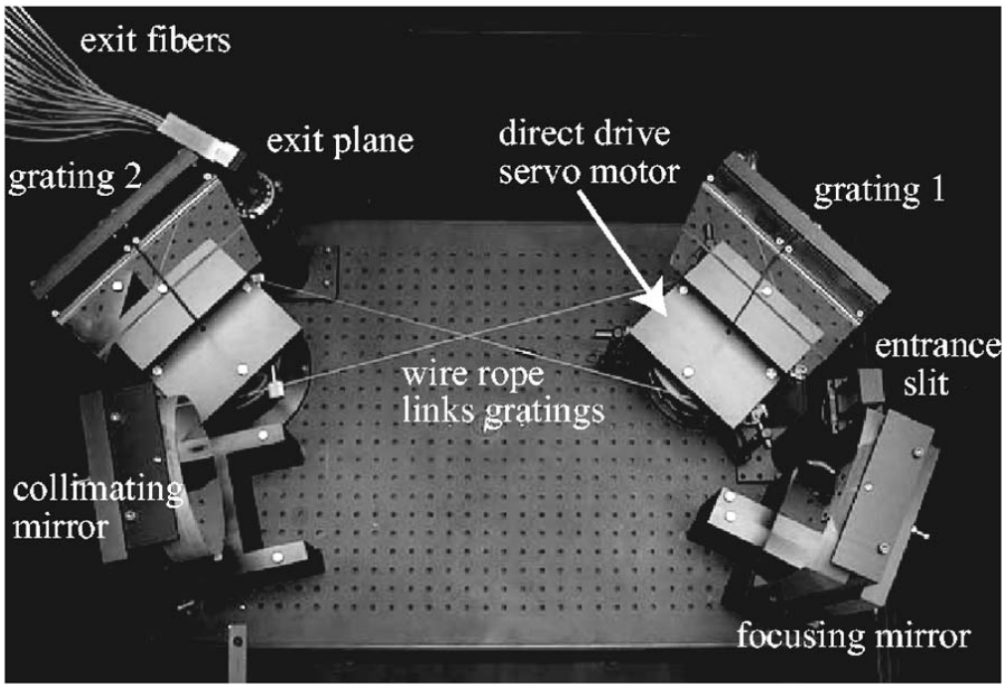

Figure 3.2.: Ion Doppler Spectrometer used for CHERS measurements on MST. Figure is reproduced from Craig et al. (2007) [2]

For this work, one fiber is used to view the neutral beam, and the second is placed next to the first so that their lines-of-sights are nearly identical, but the second fiber is displaced so that it does not see the light emitted from the neutral beam path. The background light of the displaced fiber still collects very similar background light compared to the first, however, making it an important reference for distinguishing the charge exchange and background electron impact signals for the fiber that sees both background light and charge exchange from the neutral beam.

Poloidal viewing Locations											
Chord #:	1	2	3	4	5	6	7	8	9	10	11
r/a:	-0.91	-0.76	-0.58	-0.41	-0.24	-0.07	0.11	0.28	0.45	0.62	0.79

Table 3.1.: Poloidal viewing chord locations measured from the geometric axis.

Toroidal viewing Locations							
Chord #:	1	2	3	4	5	6	7
r/a:	-0.21	0.05	0.11	0.19	0.28	0.45	0.62

Table 3.2.: Toroidal viewing chord locations measured from the geometric axis.

The diagnostic neutral beam (DNB) provides 20 ms of 4.0 A equivalent at 50 kV[6]. It is optimized for the 48 keV charge exchange cross-section peak between Hydrogen and fully-stripped carbon. The beam diameter is 4 cm with a divergence of 35 mrads. The beam intersects the $Z = 0$ midplane 6 cm from the geometric axis, which is the approximate location of the Shafranov shifted magnetic axis in axisymmetric plasmas in MST. The beam is injected radially into the machine 22.5 degrees below the midplane.

There are eleven total poloidal viewing ports, spaced 8.9 cm apart with a line-of-sight perpendicular to the diagnostic neutral beam line-of-sight. Of the eleven total view, nine were used. All the CHERS chord locations are listed in Table 3.1, where the chords used measurements are chords 3 - 11. The toroidal view consists of a rotating stage that can cover a 20 cm span along the DNB path. The optical stage for the toroidal view was realigned multiple times in order to view different sections of the beam path at a time, giving a total sampling range of 44 cm. The spot size of the intersection of the optical line-of-sight at the DNB is on the order of 1 cm. Seven discrete locations were chosen, given in Table 3.2, with an emphasis on trying to measure the same radial location as the poloidal chords. Representations of both view are shown in Figure 3.3.

The impurity species of interest for CHERS is in MST is fully stripped carbon, C^{+6},

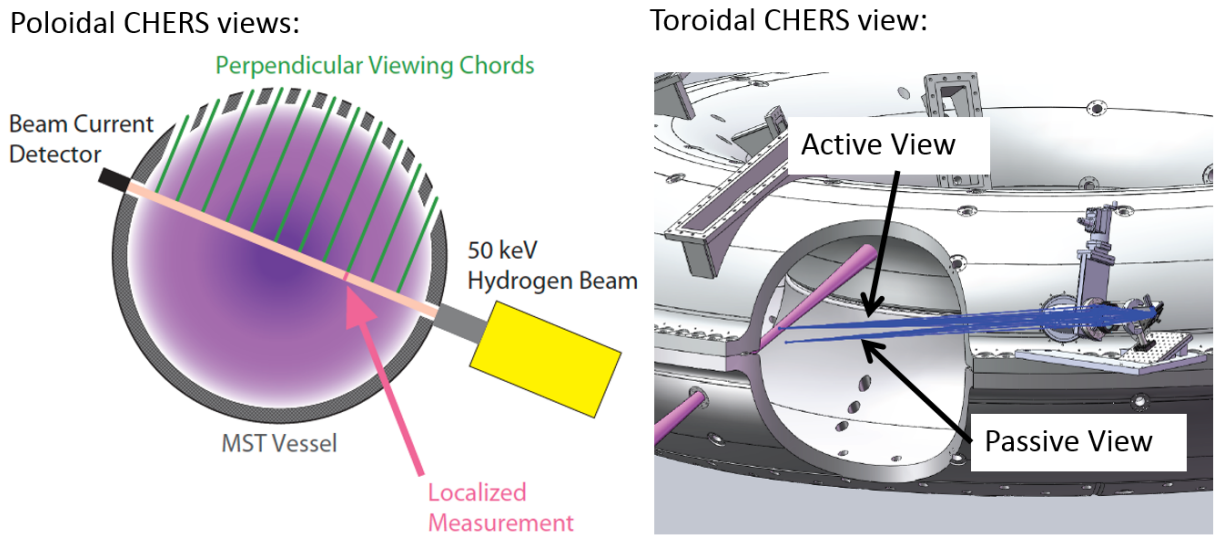

Figure 3.3.: The left figure is the poloidal cross-section showing the poloidal optical views (green lines) intersecting the diagnostic neutral beam. The line-of-sights are perpendicular to the neutral beam, which extends radially through the machine at a -22.5 degree angle. The right figure shows the toroidal CHERS optical views, both the "active" view which sees the charge exchange from the neutral beam, and the background electron impact emission, and the "passive" view which only sees the background electron impact emission.

which becomes C^{+5} when an electron is donated by atoms in the neutral beam. The emission line of interest for excited C^{+5} is the $n = 7 \rightarrow 6$ transitions at 343.383 nm. However, the total light emitted by the plasma at this wavelength is dominated by the electron impact emission of O^{+5}. Due to spin-orbit coupling effects, the fine-structure degeneracy is broken, and both electron impact of O^{+5} and charge exchange with C^{+6} emit a range of wavelengths around 343.4 nm. The total spectral radiance is a summation over all of these emission profiles. The charge exchange and electron impact emit from different locations in the plasma, and so have independent radiance, velocity, and temperature. They are distinguished by modeling

each contribution to the total spectral radiance

$$L(\lambda) = \sum_{w_{i,CX},\lambda_{i,CX}} w_{i,CX} L(\lambda, \lambda_{i,CX}, I_{CX}, T_{CX}, V_{CX}) + \sum_{w_{i,CX},\lambda_{i,CX}} w_{i,EI} L(\lambda, \lambda_{i,EI}, I_{EI}, T_{EI}, V_{EI}) \tag{3.8}$$

where the individual contributions to spectral radiance from charge exchange (CX) and electron impact (EI) follow Equation 3.4. The weighting factors, $w_{i,CX}$ and $w_{i,EI}$ are the fine structure line strength ratios calculated from ADAS[7, 8]. They quantify the relative population of the different fine structure levels, and sum to one: $\sum_i w_i = 1$. The charge exchange amplitude (I_{CX}), velocity (V_{CX}), and temperature (T_{CX}) are the localized parameters, while the electron impact amplitude (I_{EI}), velocity(V_{EI}), and temperature (T_{EI}) correspond primarily to an undetermined emission shell in the plasma, and are not well localized.

Of the data provided from CHERS spectroscopy, this thesis will focus on the localized velocity obtained from the charge exchange signal, V_{CX}, from both the poloidal and toroidal CHERS views. Typically, the point of origin for the poloidal coordinate is the Sharfanov shifted magnetic axis. As mentioned, this is about 6 cm shifted outboard from the geometric axis in MST, and is where the DNB crosses the $Z = 0$ mid-plane. In the SHAx state, this location is not the location of the magnetic axis, but instead it is the axis around which the helical magnetic axis rotates in the R, Z plane as one moves toroidally around the machine. In the proceeding analysis, instead of reporting velocities as poloidal, they are referred to as "out-of-plane" from the plane made by the DNB line-of-sight and the ϕ direction, where velocity in the positive R and Z direction move in the positive out-of-plane direction. As a consequence of not referencing a poloidal coordinate, the direction of positive flow stays the same on both sides of the point of origin. With this nomenclature, the toroidal measurements would be "in-plane" measurements, but will continue to be referred to as toroidal measurements. The coordinate system used to specify velocity directions is

shown in Figure 3.4. To the extent that poloidal directions are referred to in future analysis, it will be in reference to the axis of the former Shafranov shifted magnetic axis, as will the distinction between inboard and outboard.

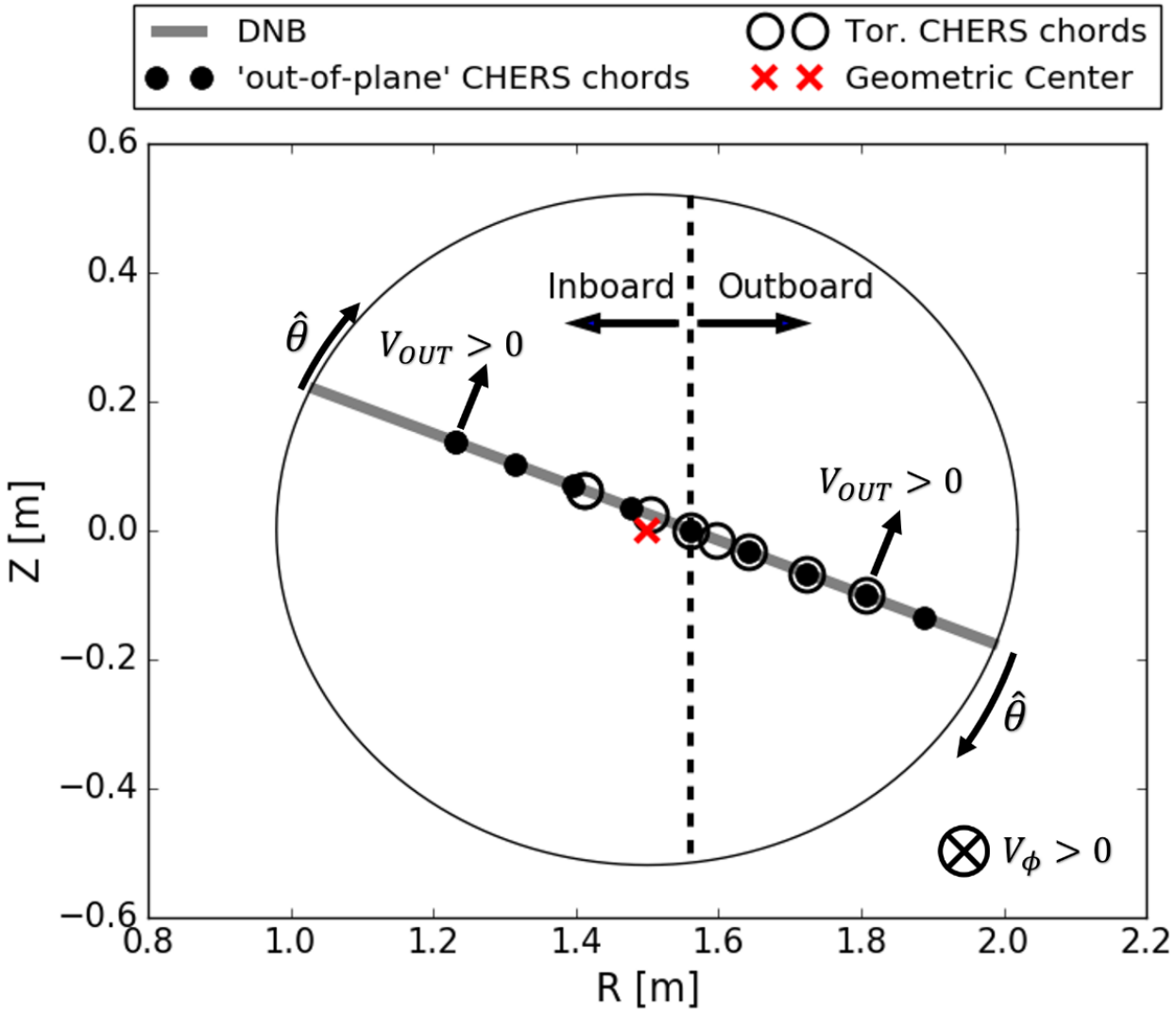

Figure 3.4.: Poloidal cross-section of MST showing DNB and CHERS viewing chords. The direction of the "out-of-plane" flow is specified as moving in the positive R, Z direction, towards the CHERS optics. The plane referred to is the one made by the DNB line-of-sight and the toroidal angle, ϕ, which is extends out of the page for the view shown here. Positive toroidal velocity is specified as moving into the page, the same direction as the MST ϕ coordinate.

3.2.3. Absolute wavelength calibration

Obtaining absolute velocity measurements with ~km/s scale sensitivity requires a well calibrated spectrometer. The velocity fitting parameter is entirely correlated with the absolute wavelength used in the fit to the data, as can be seen from Equation 3.5. Any systematic offset in the measured wavelength of each line from the spectrometer maps directly to a systematic offset in the velocity measurement. For perspective, at the wavelength of 343.383 nm, the Doppler shift that occurs from 1 km/s plasma velocity is:

$$\Delta\lambda = \frac{v}{c}\lambda = \frac{1 \text{ km/s}}{3 \times 10^5 \text{ km/s}} * 343.383 \text{ nm} = 1.1 \text{ pm} \tag{3.9}$$

So, to know the absolute velocity with ~km/s resolution, picometer scale calibration is required of the spectrometer. The next section will describe the technique used to calibrate the spectrometer day-to-day.

The spectral range of the spectrometer is set by a stepper motor that rotates the gratings in the spectrometer to the desired angle relative to the entrance and exit slits. The gratings themselves are coupled by a taught wire, so that when the stepper motor rotates one grating, the other rotates with it. The precision of the mechanical system involved in rotating the gratings is too course to provide reliable knowledge of the absolute wavelength range measured by the PMTs, which is necessary for absolute velocity measurements in the plasma. For example, a single step in the stepper motor in the 343.4 nm range corresponds to 5 pm shift in the wavelength range. Over multiple days the calibration can drift on the order of 20 pm. Instead of relying on the mechanics of the spectrometer, the spectrometer is calibrated every day at a fixed motor position using our knowledge of the intrinsic plasma flow.

The absolute wavelength can be determined by measuring the emission from plasma that experiences no net Doppler shift. The magnetic axis acts as the point of plasma rotation in toroidal plasmas, and has no poloidal flow. A highly reproducible, zero flow reference point is therefore obtained by viewing the poloidal velocity at the magnetic axis in PPCD discharges. PPCD discharges were chosen since the perturbations from tearing modes are at a minimum during PPCD periods, as is the background electron impact emission. The zero-net poloidal flow method of calibration was verified using a custom light source that uses a UV LED coupled to a Fabry-Perot interferometer to provide a calibration line in the 343.4 nm region of interest[9]. The light source was used to independently calibrate the fibers and verify the zero net poloidal flow method of calibration. The method of calibration was also recently implemented in measurements of the average velocity profiles in PPCD[10].

Generally, the absolute wavelength calibration is determined from fitting multiple PPCD discharges. PPCD calibration shots are performed at the beginning and end of every run day to ensure the calibration has not drifted substantially over the course of the day. Typically, no more than a 3 pm drift occurs over the run day. The uncertainty of the calibration technique, determined from the statistical spread in velocity fits due to shot-to-shot variability, results in an overall $\pm$ 3 pm wavelength ($\sim$ 3 km/s) uncertainty.

3.3. Phase locking control

Phase locking of the dominant tearing mode naturally occurs as the dominant mode grows into a saturated SHAx state. While this is problematic for correlation techniques that rely on the rotation of the plasma past diagnostics to infer spatial structure, if the phase locking can be controlled, spatial structure can still be obtained on a shot-by-shot basis. The technique developed for controlling phase locking is described in this section.

The process by which tearing modes decelerate and lock has been well studied in MST[11]. The deceleration and eventual locking of large tearing modes is caused by a braking torque localized to the tearing mode's resonant surface due to eddy currents in the shell. The eddy currents induce a magnetic perturbation, which in turn generates a sheet-like current near the tearing mode's resonant surface, and ultimately produces a phase-lagged $\boldsymbol{j}_{sheet} \times \boldsymbol{b}_{mode}$ electromagnetic torque that opposes tearing mode rotation. Deceleration and mode-locking of tearing modes is ubiquitous in the saturated SHAx state, as well as most high-current, low density QSH states. Since the breaking torque is proportional to the tearing mode amplitude, the very large helical perturbation of a QSH state ensures that mode-locking occurs.

The active feedback system at the poloidal gap on MST can be used to apply an external resonant magnetic perturbation (RMP) to induce a large braking torque as well[12]. The active feedback system is typically used to control the error fields arising from the poloidal cut in MST's conducting shell. An array of 32 sense coils measure the radial magnetic field at the cut (see Figure 3.5), and 38 correction coils apply a radial magnetic field to cancel out the error field. The same coils can also be used to add a specific radial magnetic field perturbation in addition to correcting the error field resulting in a user-controlled magnetic perturbation of defined poloidal m harmonic. The n spectrum of the magnetic perturbation flux is very broad since the perturbation is applied through a narrow cut in the conducting shell.

The locking phase resulting from the torque generated by eddy currents in the conducting shell is quasi-random. By applying an $m = 1$ RMP, the torque generated by the RMP can overpower the torque from the eddy currents, and the mode will lock to the same phase as the RMP. This allows the operator to control the final orientation of the 3D state. This method of using an $m = 1$ RMP to control the orientation of the mode-locking in the growing

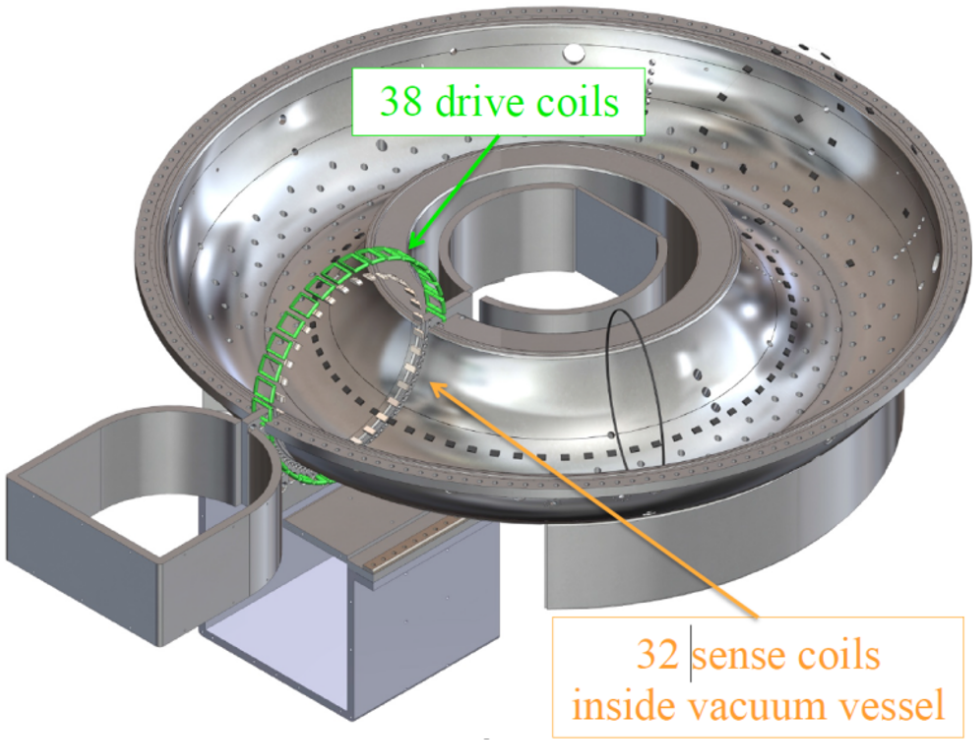

Figure 3.5.: RMP drive and sense coils shown at the poloidal cut in MST's conducting shell.

QSH state has been studied and optimized in MST[12]. For any given QSH discharge, there is a high likelihood of obtaining the desired mode-locked phase, to within 15 degrees. In practice, the method consists of applying an $m = 1$ RMP between 10-15 ms of the plasma discharge, which is the time period where the $n = 5$ tearing mode amplitude grows strong enough to create a braking torque that causes mode-locking.

Care was taken to apply an RMP that was minimally disruptive to the QSH state, specifically in the saturation phase. Two examples of mode locking with and without the RMP are shown in Figure 3.6. By the time the QSH state saturates, the RMP is off, or at very low levels, where the peak values are applied between 15-17 ms, shown in Figure 3.6 c.). The locking of the plasma tends to occur earlier in time with the RMP applied than

without the RMP. Figure 3.7 a.) and b.) shows a density scatter plot for locking times and the mode amplitudes locking occurs at for a number of shows with and without and RMP respectively. One noticeable difference was the tendency for the radial magnetic field at the poloidal gap to be larger in shots with the RMP applied than without, shown in Figure 3.7 c.) and d.). Even the increased b_r values are still small, on the order of 1-2% of the edge magnetic field.

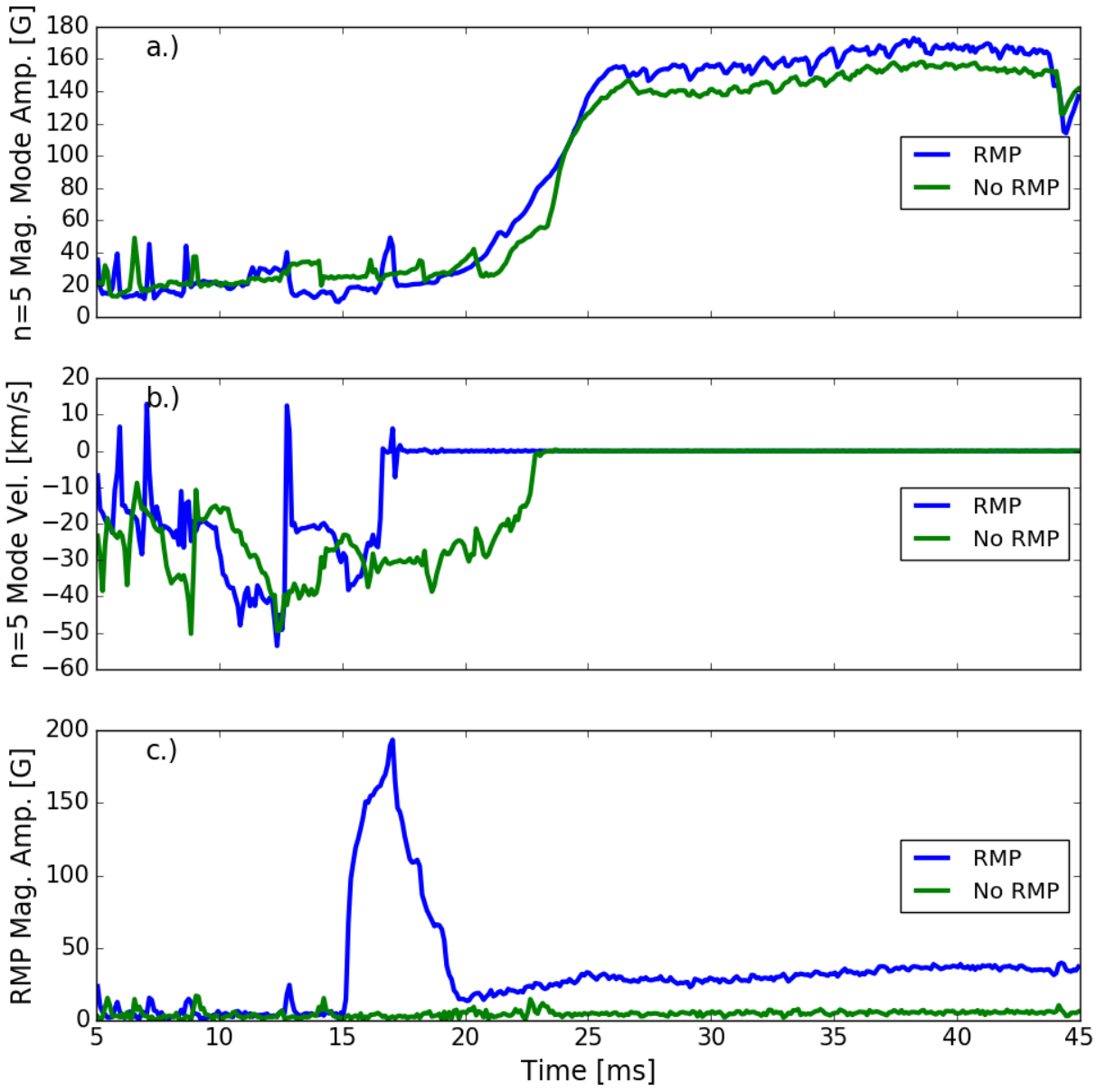

Figure 3.6.: Examples of SHAx evolution with and without the application of the RMP. The $n = 5$ mode amplitude (a) and mode velocity (b) vs time are plotted as well as the measured b_r (c) at the poloidal gap.

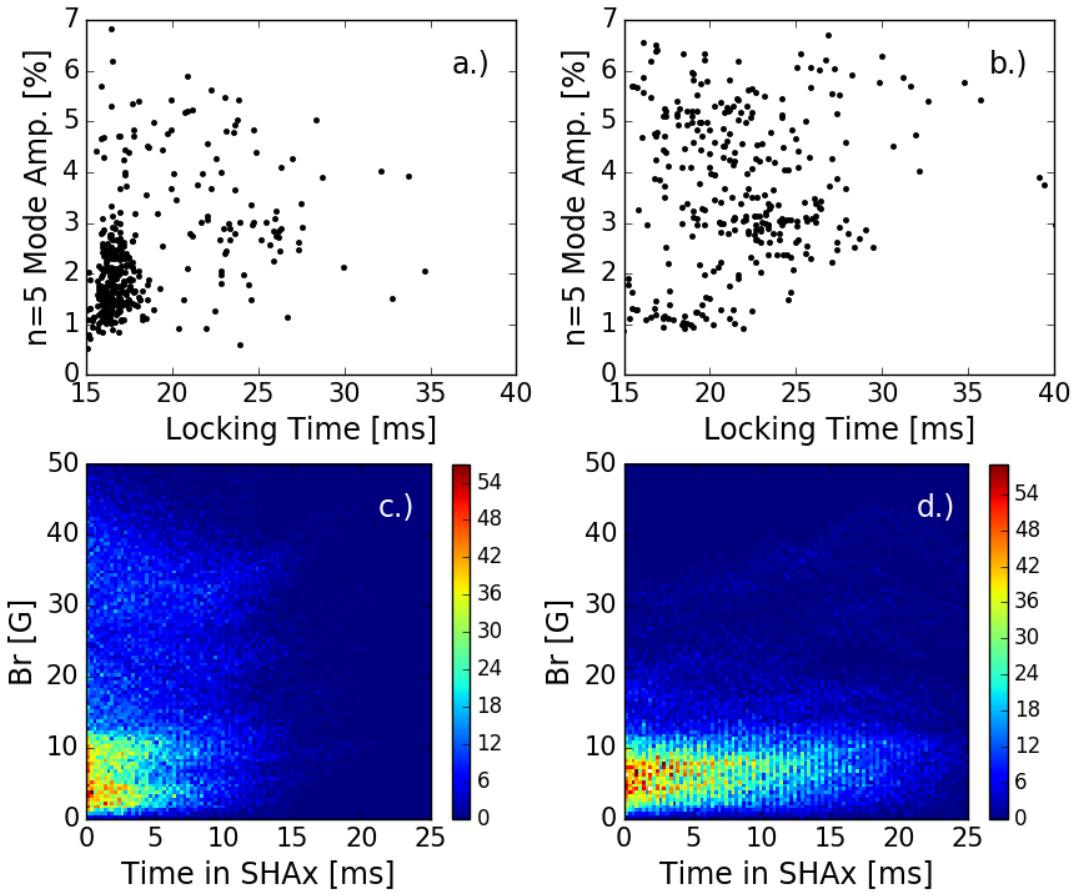

Figure 3.7.: Dominant mode amplitude vs locking time for a large sample of shots with a.) the RMP on between 15-20 ms and b.) when no RMP is used. The typical radial magnetic field measured at the wall is represented as a density plot of time points vs the time since the plasma entered the SHAx state for a number shots where c.) an RMP was used, and d.) no RMP was used. The RMP was off for the time when the plasma was in the SHAX state.

3.4. V3FIT

V3FIT is a three-dimensional equilibrium reconstruction solver constrained by experimental measurements[13]. V3FIT equilibrium profiles have been successfully obtained in both MST with a close conducting shell, and RFX [14, 15]. It has also been successfully employed in the tokamak hybrid scenario[16], and is widely used with stellarators. While it is agnostic as to the magnetic equilibrium solver it employs, so long as it is a 3D solver, this implementation uses VMEC[17]. VMEC solves the ideal MHD equation $\nabla P = \boldsymbol{J} \times \boldsymbol{B}$ along with Ampere's law and the requirement for a divergence-free magnetic field for given user input q and pressure profiles, total magnetic flux, and geometric specifications of the system. VMEC finds solutions by minimizing the total plasma energy

$$W = \int \left(\frac{B^2}{2\mu_0} + P \right) dV. \tag{3.10}$$

V3FIT uses VMEC input profiles as part of its parameter set in a forward model to reproduce measured diagnostic signals. A χ^2 minimization between computed and measured diagnostic signals is used to find the ideal 3D MHD magnetic reconstruction that best fits the measured signals:

$$\chi^2 = \sum_i \left(\frac{S_i^o(\boldsymbol{d}) - S_i^m(\boldsymbol{p})}{\sigma_i} \right)^2 \tag{3.11}$$

where $S_i^o(\boldsymbol{d})$ is a vector of diagnostic signals for diagnostics $\boldsymbol{d}$ with associated uncertainty σ_i, and $S_i^m(\boldsymbol{p})$ is a vector of synthetic diagnostic signals calculated from flux surfaces calculated from input parameters $\boldsymbol{p}$. Diagnostics signals include MST's Thomson scattering, FIR interferometry and polarimetry, soft-x-ray, and edge magnetic diagnostics. Figure 3.8 overviews these diagnostics and their locations on the machine; more information can be found in [14]. The work flow to find an optimized equilibrium profile is overviewed in Figure 3.9.

To obtain a helical magnetic equilibrium in MST, only the $n = 0$ and $n = 5$ modes from the Fourier decomposition of the edge magnetics signal are used instead of the raw toroidal magnetics array data, which would include $n > 5$ contributions. In VMEC, a periodicity of $N = 5$ is also chosen, such that the equilibrium must have five-fold toroidal symmetry. As a note, capital N denotes the periodicity of the system, and lower case n specifies a mode within the equilibrium. All $n > 0$ toroidal modes are harmonics of a base $N = 5$ periodicity. Multiple m modes are still allowed, but this simplification greatly reduces the computational complexity of the problem and makes solutions tractable.

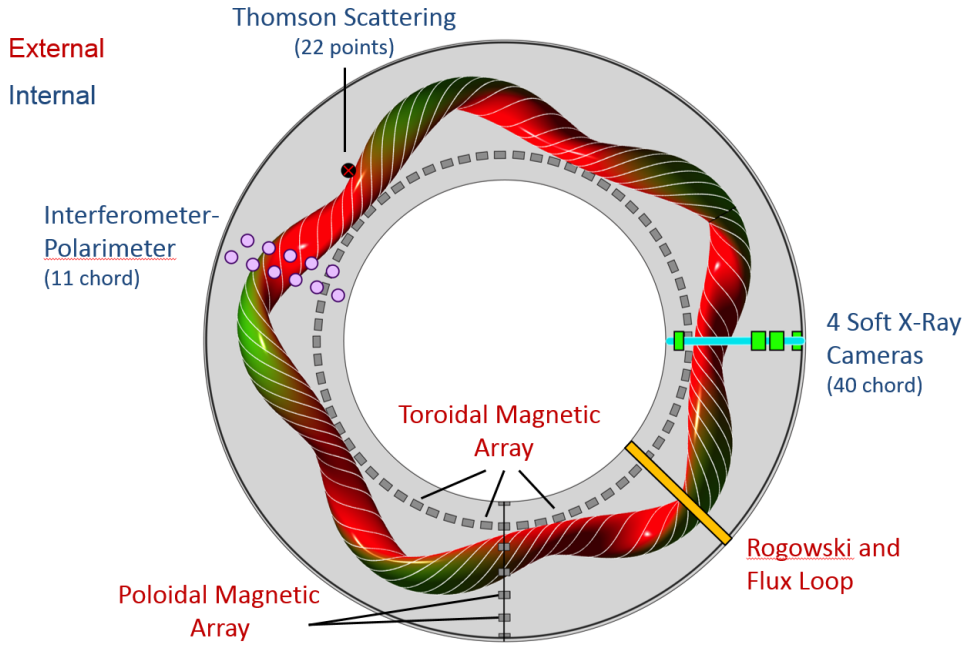

Figure 3.8.: Figure showing diagnostic signals important to the V3FIT reconstruction. Internal diagnostics are optical diagnostics that probe the core of the plasma. External diagnostics are magnetic b-dot coils at the edge of the plasma. CHERS is not used in V3FIT.

Since VMEC uses ideal MHD, ideal nested flux surfaces are assumed, which means it cannot represent QSH states that have not yet become SHAx. With any method of magnetic reconstruction, it is important to remember that it is still a simplified representation

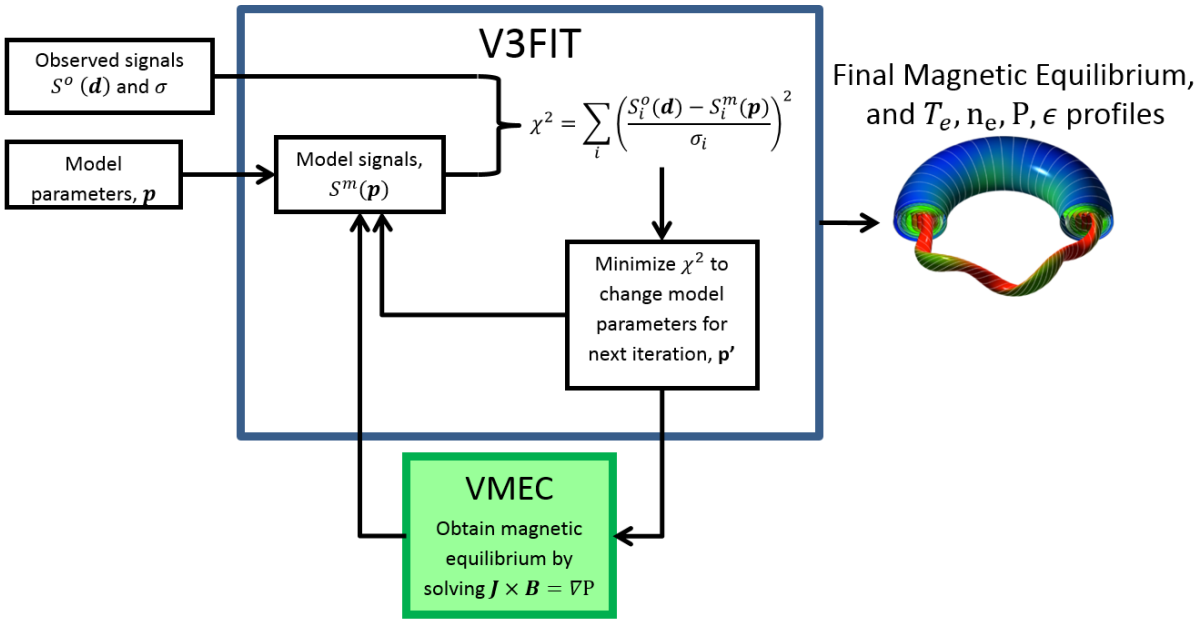

Figure 3.9.: Flowchart of basic fitting procedure done by V3FIT to arrive at parameterized profiles of temperature, density, soft-x-ray emissivity, and a VMEC MHD equilibrium using χ^2 minimization

of the plasma equilibrium given the constraints of the method, and that the true plasma is inherently dynamic with stochastic regions. Still, the 3D ideal MHD flux surfaces generated by V3FIT-VMEC do a better job at representing the diagnostic signals from Thomson scattering, soft x-ray, FIR interferometry and polarimetry, and the magnetics arrays than an axisymmetric reconstruction.

3.5. Toroidal sampling by correlating to $n = 5$ magnetic locking phase

The standard practice for approximating the structure of local perturbations from toroidally averaged values such as velocity, temperature, and density is to correlate a diagnostic time-

series signals with the magnetic modes measured at the wall. The global tearing mode perturbations measured at the wall are frozen into the plasma and are dragged along with it as it rotates. It is a natural assumption that probing a rotating spatial perturbation in time with a stationary diagnostic is equivalent to spatially probing the 3D structure of a plasma. Typically, the correlated signal strength of a measurement with the rotating magnetic mode phase is poor, so many shots have to be taken in order to obtain good statistics for the observation.

The saturated SHAx state presents a unique challenge since it consistently mode-locks before the dominant mode saturates. This motivated the development of the RMP system that could control the orientation of the QSH state's final locked position. Each shot only gives information about a single position in 3D space, and the helical structure must be moved toroidally through the diagnostic on a shot by shot basis. Velocity profiles in the saturated SHAx state are obtained using three simplifying assumptions: the helical equilibrium velocity is constant in time, it is $N = 5$ symmetric, and the experiment produces essentially the same equilibrium regardless of the locking phase.

One way of testing the reproducibility of SHAx plasmas at different locking angles is by analyzing the steady state dominant and sub-dominant tearing mode amplitudes. Figure 3.10 shows that the average dominant and sub-dominant mode amplitudes depend slightly on the locking phase. However, the magnetic amplitude variation with locking phase is within the typical window for the saturated SHAx state mode amplitude, and no clear correlation was seen between these mode amplitude variations and the velocity profiles.

Ideally, for an ensemble of shots correlated to the $n = 5$ locking phase, the phase of the sub-dominant modes would be sampled sufficiently randomly that any effect would average to zero. However, as seen by the density plot in Figure 3.11 comparing sub-dominant tearing

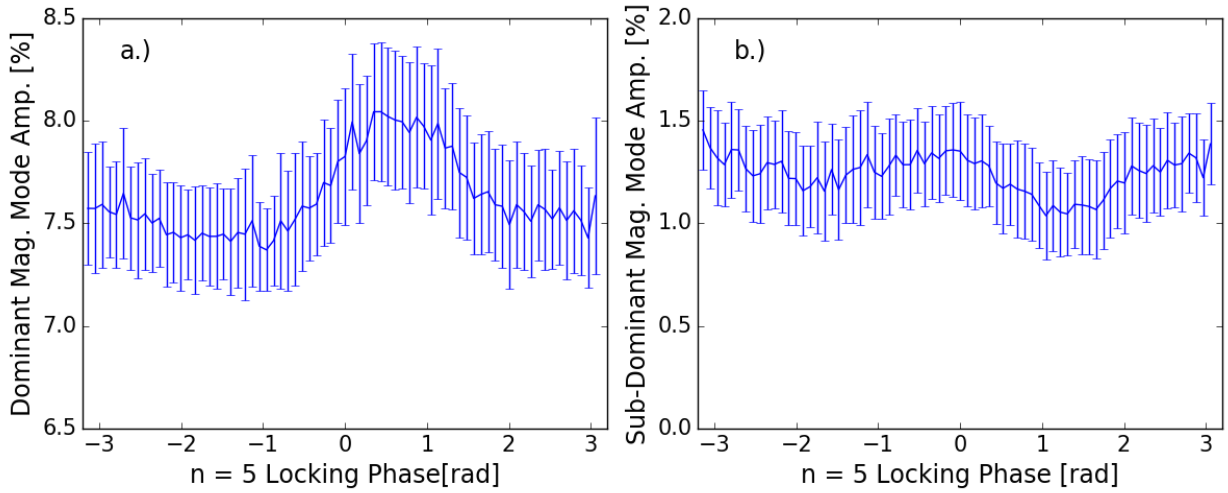

Figure 3.10.: Mode amplitude of the aggregated a.) dominant and b.) sub-dominant magnetic modes in the SHAx state *vs.* $n = 5$ locking phase. Mode amplitudes are reported as a percent of the edge magnetic field measured, and the error bars are the standard deviation of data binned in five degree increments.

mode phases to the $n = 5$ locking phase, there is relatively strong correlation between the $n = 5$ locking phase, and the phase of the sub-dominant tearing modes. One might consider this to be due to the RMP, which exerts a braking torque on all tearing modes, not just the $n = 5$, but the correlation is present in SHAx discharges that did not use and RMP as well, as shown in Figure 3.12. Some of the correlations between sub-dominant tearing modes and the $n = 5$ modes have changed, however. Despite the correlation of the $n > 5$ tearing modes with $n = 5$ locking phase, the contribution of the higher n modes velocity profiles is expected to be small. The strength of the tearing mode velocities is expected to scale with magnetic mode amplitude, which is significantly smaller for the $n > 5$ modes.

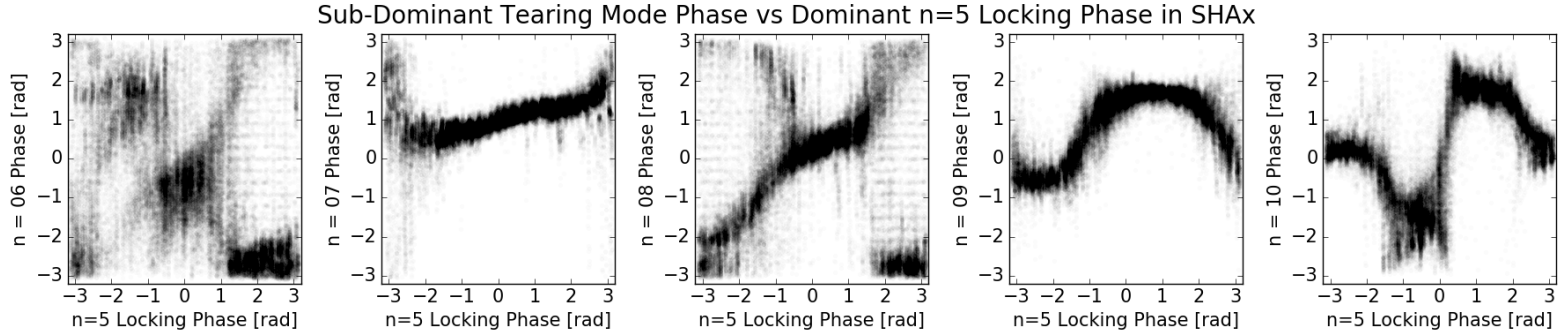

Figure 3.11.: Density plots of tearing mode phase correlations between the n = 5 locking phase and sub-dominant mode phases in the SHAx state.

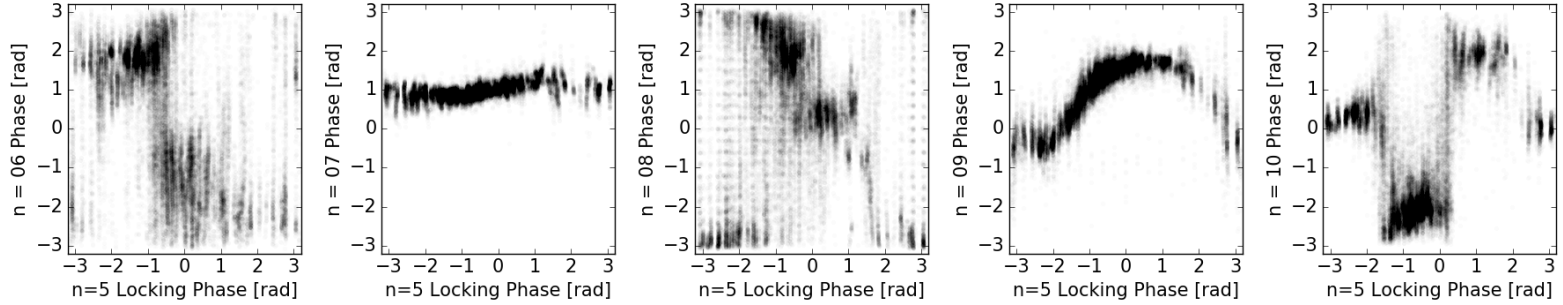

Figure 3.12.: Density plots of tearing mode phase correlations between the n = 5 locking phase and sub-dominant mode phases in the SHAx state for set of shots where the RMP was not used.

3.5.1. Mapping between $n = 5$ locking phase and the helical equilibrium

The orientation of the helical equilibrium relative to MST's diagnostics can be deduced through the $n = 5$ magnetic phase, and the helical equilibrium can be described with its own toroidal angle, ϕ_{hel}. It is useful to discuss measurements in terms of the toroidal angle of the helical equilibrium because it makes comparisons to simulations and magnetic reconstructions more straightforward. The relationship between this angle and the MST coordinates through the $n = 5$ magnetic phase measured at $\phi_{MST} = 0°$, $\theta_{MST,LH} = 241°$, where LH stands for left-handed coordinates commonly used within the MST group. In this way, the $n = 5$ magnetic phase is used as a proxy for the toroidal angle of the helical equilibrium, ϕ_{hel}. While it is not necessary to cast measurements in terms of the helical toroidal angle, it is a useful quantity for comparisons to simulations and reconstructions where data is presented relative to a toroidal angle. The relations between the chosen coordinate system will now be discussed.

While the magnetic phase being referenced is defined relative to $\phi_{MST} = 0°$, $\theta_{MST,LH} = 241°$, we are free to choose where $\phi_{hel} = 0$. It is most convenient to choose the zero point when the helical magnetic axis intersects the DNB line-of-sight on the outboard side, at $\phi_{MST} = 270°$, $\theta_{MST,LH} = -22.5°$. The helical magnetic axis (which evolved from the tearing mode island O-point) occurs at the same location as the maximum of $\tilde{b} = \tilde{b}_{n,m}\cos(k)$, where the argument of the cosine is

$$k = n\phi + m\theta - \delta_{m,n}. \tag{3.12}$$

The magnetic amplitude and phase measured at the wall only determines a 1D perturbation at fixed θ, described in Equation 3.3. By assuming the 2D perturbation can be described as a

1D helical perturbation, the mapping from magnetic phase measurement to helical magnetic axis can be made. Technically, the measured perturbation includes contributions from other poloidal modes which can introduce constant phase shifts in the measurements[18], but this effect is relatively small and ignored here. At $\theta_{MST,LH} = 241$:

$$\tilde{b}\cos\left(n\phi - \delta_n\right) = \tilde{b}\cos\left(n\phi + m(241) - \delta_{m,n}\right)b \tag{3.13}$$

We can relate the phase δ_n measured by the toroidal magnetics array to a global 2D perturbation phase:

$$n(0) - \delta_n = n(0) + m(241) - \delta_{m,n} \tag{3.14}$$

$$\delta_{m,n} = \delta_n + m(241). \tag{3.15}$$

The magnetic axis follows the helical path where the argument of the cosine function, Equation 3.12, is zero. The phase measured by the toroidal magnetics array, δ_n, when the magnetic axis is located at any specified toroidal and poloidal location is determined by combining Equation 3.15 with Equation 3.12 and setting the argument to zero:

$$\delta_n = n\phi + m(\theta - 241) \tag{3.16}$$

where we are specifically interested in the $m = -1$, $n = 5$ mode in the MST (r, θ, ϕ) left-handed reference frame, where $\hat{\theta}$ is pointed in the positive Z direction at the outboard mid-plane. The phase measured by the toroidal array when the helical magnetic axis is at the outboard side of the DNB is $\delta_n = 173.5^o$. The new toroidal angle describing the helix is equivalent to the argument of the cosine term above, $\cos(n\phi_{hel}) = \cos(k)$, or

$$5\phi_{hel} = -\delta_n + 173.5^o. \tag{3.17}$$

It should be emphasized in case of confusion that there is nothing helical about the actual coordinate ϕ_{hel}, it is simply describing the toroidal location of the helical equilibrium with respect to some reference point.

As the helical equilibrium sweeps toroidally through the DNB line-of-sight, a slice of the equilibrium in the DNB-ϕ plane can be probed by the CHERS diagnostic. The puncture plot of representative flux surfaces probed in the DNB-ϕ plane is shown in Figure 3.13, where for the plot the "hel" label for ϕ is dropped. Four poloidal cross-sections of the flux surfaces are shown in Figure 3.14 that correspond to the colored lines in Figure 3.13 at constant ϕ. Comparing the two plots, it is clear that at $\phi = \pi/2$ and $-\pi/2$, the helical core is not in the view of the DNB path, shown as the grey line in the poloidal cross-section plots, and correspond to the disappearance of the helical magnetic axis in Figure 3.13 at those toroidal locations.

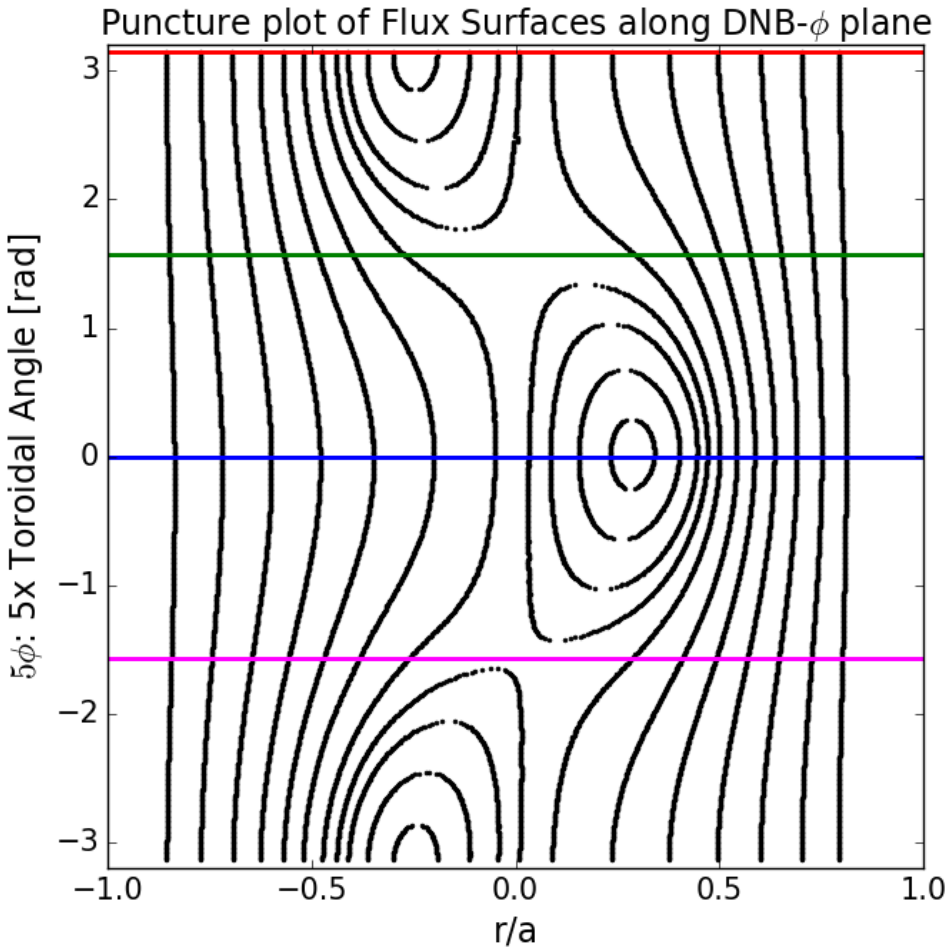

Figure 3.13.: Representative flux surfaces probed in the DNB-ϕ plane, obtained from V3FIT reconstruction. The toroidal angle has been chosen so that the magnetic axis aligned with the outboard DNB location. Colored lines match the color of the flux surfaces in the poloidal cross-sections of flux surfaces in Figure 3.14.

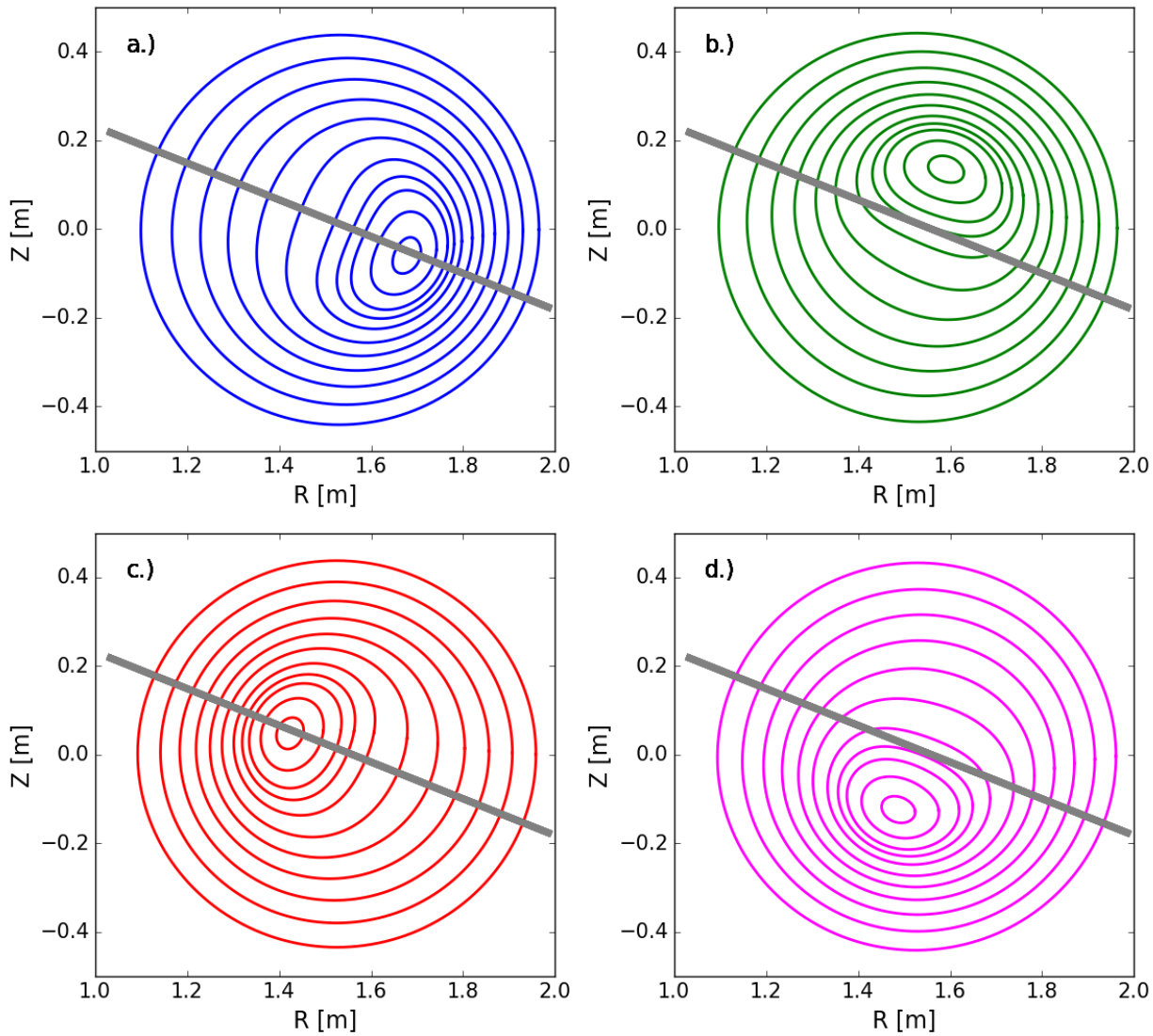

Figure 3.14.: Poloidal cross-section of flux surfaces at 4 toroidal angles: a.) $\phi_{hel} = 0$ rad., b.) $\phi_{hel} = \pi/2$ rad., c.) $\phi_{hel} = \pi$ rad., d.) $\phi_{hel} = -\pi/2$ rad. The gray line through the machine represents the path of the DNB. Notice that at $\pi/2$ and $-\pi/2$ rad., the helical core is not sampled by the DNB.

3.6. Summary

The CHERS diagnostic and resonant magnetic perturbation system are used to obtain flow measurements at any desired toroidal location in the helical equilibrium of the saturated SHAx state. Using the toroidal magnetics array and representative V3FIT reconstructions, the data from these measurements is mapped onto an $N = 5$ symmetric helical magnetic equilibrium. With these tools in hand, the next chapter will present shot aggregated measurements as toroidal and radial profiles of toroidal flow and out-of-plane flow.

References

[1] J. Koliner, *Neutral Beam Excitation of Alfven Continua in the Madison Symmetric Torus Reversed Field Pinch.* PhD thesis, University of Wisconsin - Madison, 2013.

[2] D. Craig, D. J. Den Hartog, D. A. Ennis, S. Gangadhara, and D. Holly, "High throughput spectrometer for fast localized Doppler measurements," *Review of Scientific Instruments*, vol. 78, no. 1, p. 013103, 2007.

[3] D. Ennis, *Local Measurements of Tearing Mode Flows and the MHD Dynamo in the MST Reversed-Field Pinch.* PhD thesis, University of Wisconsin - Madison, 2008.

[4] R. Magee, *Ion energization during tearing mode magnetic reconnection in a high temperature plasma.* PhD thesis, University of Wisconsin - Madison, 2011.

[5] T. Nishizawa, *Characterizing the Role of Drift-Wave turbuence in a Reversed Field Pinch.* PhD thesis, University of Wisconsin - Madison, 2018.

[6] G. F. Abdrashitov, V. I. Davydenko, P. P. Deichuli, D. J. Den Hartog, G. Fiksel, A. A. Ivanov, S. A. Korepanov, S. V. Murakhtin, and G. I. Shulzhenko, "A diagnostic neu-

tral beam system for the MST reversed-field pinch," *Review of Scientific Instruments*, vol. 72, pp. 594–597, 1 2001.

[7] H. P. Summers and M. G. O'Mullane, "Atomic data and modelling for fusion: The ADAS Project," in *AIP Conference Proceedings*, vol. 1344, pp. 179–187, 2011.

[8] S. Gangadhara, D. Craig, D. A. Ennis, and D. J. Den Hartog, "Modeling fast charge exchange recombination spectroscopy measurements from the Madison Symmetric Torus," in *Review of Scientific Instruments*, vol. 77, p. 10F109, 2006.

[9] M. M. Baltzer, D. Craig, D. J. Den Hartog, T. Nishizawa, and M. D. Nornberg, "Absolute wavelength calibration of a Doppler spectrometer with a custom Fabry-Perot optical system," *Review of Scientific Instruments*, vol. 87, p. 11E509, 11 2016.

[10] D. Craig, E. H. Tan, B. Schott, J. K. Anderson, J. Boguski, D. J. Den Hartog, T. Nishizawa, M. D. Nornberg, and Z. A. Xing, "Intrinsic flow and tearing mode rotation in the RFP during improved confinement," *Physics of Plasmas*, vol. 26, p. 072503, 7 2019.

[11] B. E. Chapman, R. Fitzpatrick, D. Craig, P. Martin, and G. Spizzo, "Observation of tearing mode deceleration and locking due to eddy currents induced in a conducting shell," *Physics of Plasmas*, vol. 11, no. 5, pp. 2156–2171, 2004.

[12] S. Munaretto, B. E. Chapman, D. J. Holly, M. D. Nornberg, R. J. Norval, D. J. Den Hartog, J. A. Goetz, and K. J. McCollam, "Control of 3D equilibria with resonant magnetic perturbations in MST," *Plasma Physics and Controlled Fusion*, vol. 57, no. 10, p. 104004, 2015.

[13] J. D. Hanson, S. P. Hirshman, S. F. Knowlton, L. L. Lao, E. A. Lazarus, and J. M. Shields, "V3FIT: A code for three-dimensional equilibrium reconstruction," *Nuclear Fusion*, vol. 49, no. 7, p. 075031, 2009.

[14] J. J. Koliner, M. R. Cianciosa, J. Boguski, J. K. Anderson, J. D. Hanson, B. E. Chapman, D. L. Brower, D. J. Den Hartog, W. X. Ding, J. R. Duff, J. A. Goetz, M. McGarry, L. A. Morton, and E. Parke, "Three dimensional equilibrium solutions for a current-carrying reversed-field pinch plasma with a close-fitting conducting shell," *Physics of Plasmas*, vol. 23, no. 3, p. 032508, 2016.

[15] D. Terranova, L. Marrelli, J. D. Hanson, S. P. Hirshman, M. Cianciosa, and P. Franz, "Helical equilibrium reconstruction with V3FIT in the RFX-mod Reversed Field Pinch," *Nuclear Fusion*, vol. 53, no. 11, p. 113014, 2013.

[16] A. Wingen, R. S. Wilcox, S. K. Seal, E. A. Unterberg, M. R. Cianciosa, L. F. Delgado-Aparicio, S. P. Hirshman, and L. L. Lao, "Use of reconstructed 3D equilibria to determine onset conditions of helical cores in tokamaks for extrapolation to ITER," *Nuclear Fusion*, vol. 58, no. 3, p. 036004, 2018.

[17] S. P. Hirshman, W. I. Van Rij, and P. Merkel, "THREE-DIMENSIONAL FREE BOUNDARY CALCULATIONS USING A SPECTRAL GREEN'S FUNCTION METHOD," tech. rep., 1986.

[18] J. Sauppe, *Extended Magnetohydrodynamic Modeling of Plasma Relaxation Dynamics in the Reversed Field Pinch*. PhD thesis, University of Wisconsin - Madison, 2015.

4. SHAx velocity measurements

This chapter presents the velocity data from local CHERS measurements taken in the saturated SHAx regime. The data from many toroidal and radial locations are aggregated in time across many shots to provide toroidally and radially resolved profiles of flow in the toroidal and poloidal plane. The data is also Fourier decomposed with respect to the toroidal angle of the helical equilibrium to provide amplitude and phase values for a parameterized velocity profile, allowing the axisymmetric and non-axisymmetric components of the flow to be analyzed separately.

As mentioned in Section 2.1, the saturated SHAx regime is chosen to be when the dominant mode is 7% of the magnetic field measured at the wall, and the spectral index is less than 1.2. Figure 4.1 a.) and b.) show example data from a discharge that enters a saturated SHAx state. The evolution of the velocity in time for the specific discharge plotted in Figure 4.1 a.) and b.) shows a significant change in velocity as the plasma transitions from multi-helicity to SHAx. Strong changes such as these are observed consistently at specific radial and toroidal locations, but are not ubiquitous to the entire plasma. There is insufficient velocity data in the multi-helicity state to appropriately characterize its flow profile, and the regime will not be considered here.

The saturated SHAx region of interest during the discharge is highlighted in red. The

velocity measurements made in that time window are plotted in blue in Figure 4.1 c.). The figure also shows the rest of the out-of-plane velocity measurements for all other discharges at this radial location, $r/a = 0.62$. As discussed in Section 3.5, toroidal resolution is achieved on a shot-by-shot basis using the RMP to control the toroidal angle of the helical equilibrium relative to the CHERS diagnostic.

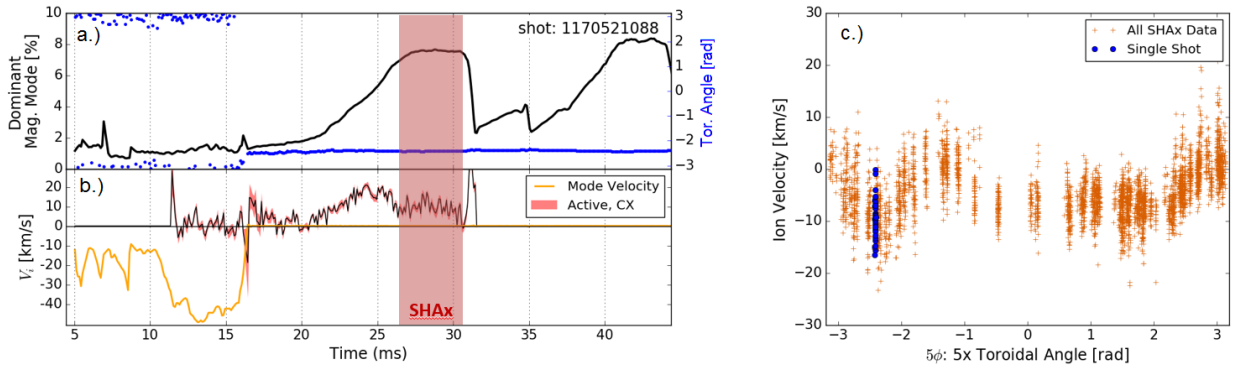

Figure 4.1.: a.) Time evolution of a SHAx discharge showing the dominant, $n = 5$ magnetic mode(black) and phase (blue). b.) The $n = 5$ mode velocity and local CHERS velocity at $r/a = 0.62$. c.) The velocity profile *vs.* relative toroidal angle for $r/a = 0.62$. The velocity timeseries data in the shaded SHAx region in a.) is plotted in c.) in blue indicating the scatter in the velocity measurements. All other data points are obtained from SHAx regions from other discharges.

4.1. Fit to the $n = 5$ magnetic tearing mode and its harmonics

The velocity profiles can be decomposed into a Fourier series with respect to the toroidal angle of the helical equilibrium at each radial location. Since the $n = 5$ magnetic phase is used to infer the location of the helical equilibrium relative to the CHERS diagnostic, all Fourier harmonics will be a multiple of five. Specific harmonics will be referred to with lower case n. When referring to the periodicity inherent to the Fourier decomposition, capital N

will be used, where $N = 5$. The harmonic multiple of N is k such that $n = Nk$. The profile used to fit to the data is:

$$V(r, \theta, \phi_{hel}) = V_0(r, \theta) + \sum_{k=1}^{k_{\max}} \widetilde{V}_{Nk}(r, \theta) \cos\left((Nk)\phi_{hel} - \Delta_{Nk}\right). \tag{4.1}$$

The measured local velocity is V, V_0 is the axisymmetric flow, and $\widetilde{V}_{Nk}$ is the component of the velocity correlated with toroidal mode number. The phase, Δ_{Nk}, is relative to the toroidal angle of the helical equilibrium, and does not use $n > 5$ magnetic phase data. The maximum number of harmonics is $k_{\max} = 5$. The fit was cut off at five harmonics because that was the largest number of harmonics necessary to adequately reproduce the fit at any location from an analysis of variance; after five harmonics, there is little reduction in variance when more harmonics are added to the fit. Other locations are well described with even fewer harmonics. Higher harmonic amplitudes are typically ~ 1 km/s. An example of the fit to the data is given by the dotted black line in Figure 4.2 for $r/a = 0.62$. The other lines show the individual harmonics that combine to give the total fit, and the orange crosses are the raw data used in the fit.

The uncertainty reported for the amplitudes and phases of the Fourier decomposition is determined by finding the spread in amplitude and phase parameters from fitting ten random subsets of the total dataset. The size of the uncertainty in the parameters in the Fourier decomposition are directly related to the spread in the velocity measurements in real space, which is the subject of the next section.

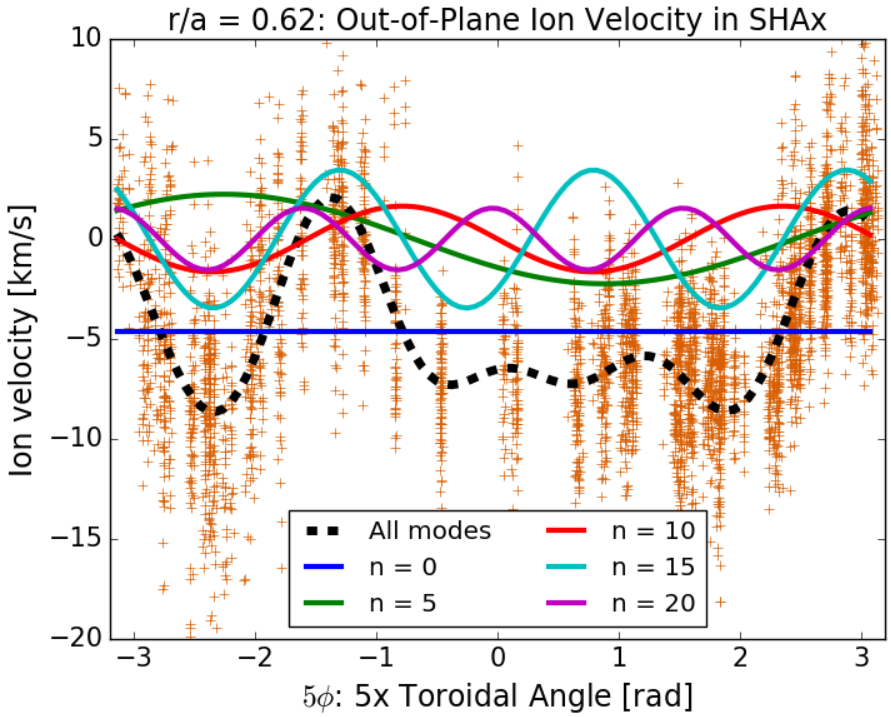

Figure 4.2.: Velocity data aggregated over time and repeated discharges. The Fourier components of the best fit are shown (colored lines) as well as the combination of the harmonics to provide an overall fit (dotted black line).

4.2. Statistical uncertainties in velocity measurements

There are two dominant sources of error in the spectroscopic velocity measurements. The first comes from the uncertainty in the absolute wavelength calibration measurement obtained each day. As discussed previously, this introduces, on average, a $\pm$ 3 km/s systematic uncertainty for the day. The second source of error comes from the noise in the measurement signal itself, which will be the subject of consideration for this section. There is significant spread in the velocity fits of the SHAx state aggregated in time. The spread, however, is consistent with the spread that would occur due to the Poisson noise in the measurement of the photon flux by the spectrometer. This was verified by fitting synthetic spectra con-

structed using plasma parameters similar to those seen in the 500 kA SHAx regime. Poisson noise was added to the signal and it was run through the fitting routine. The electrical signal recorded by the CHERS spectrometer PMTs is proportional to the incident photon flux and the noise is Poisson in nature[**?**]. Without added noise, the parameters are perfectly recovered by the fitting routine. When the noisy signal is input to the fitting routine, the resulting distribution in the velocity fitting parameter has a spread similar to that seen in the experiment. This supports the notion that the noise in the system is statistical in nature, and that the steady state assumption is valid for the time averaging done on the data.

The procedure described above is illustrated in Figure 4.3, where the spread in the fitted velocity parameter for experimental and synthetic data for two different cases is given. Two takeways are made clear: The spread in velocity fits from experimental data increases with decreasing charge exchange signal, and the spread is consistent with fitting a noisy spectrum with constant plasma parameters. Figure 4.3 a.) shows the spread in the experimental data for high radiance (green distribution, $I_{CX} = 18$ nW/sr cm^2) and low radiance (blue distribution, $I_{CX} = 8$ nW/sr cm^2). A "count" in these histograms is a single fit. As is clear, the higher radiance signal has less spread because the signal-to-noise ratio is larger. Figure 4.3 b.) shows the spread in fits from synthetic data with similar parameters as the experimental data for the two different cases, high and low radiance CHERS signals. Comparing distributions with the same radiance (color coded in the plots) between experimental and synthetic data plots, it can be seen that the spread in the experimental data is similar to fitting a spectrum with constant velocity, but subject to Poisson noise.

The scaling of the spread in velocity fits with the strength of the charge exchange recombination signal, I_{CX}, and background electron impact signal, I_{BG}, is further explored in Figure 4.4. For data in this thesis, the figure shows how the spread in velocity fits of synthetic data increases non-linearly with decreasing charge exchange signal. The effect is

enhanced as the background electron impact signal level increases relative to the charge exchange signal. The typical signal levels range between 8 and 20 nW/sr cm^2 for charge exchange, and between 20 and 50 nW/sr cm^2 for the background electron impact in the 500 kA SHAx regime. A cut off of 5 nW/sr cm^2 is applied to charge exchange data, below which data is rejected from the ensemble.

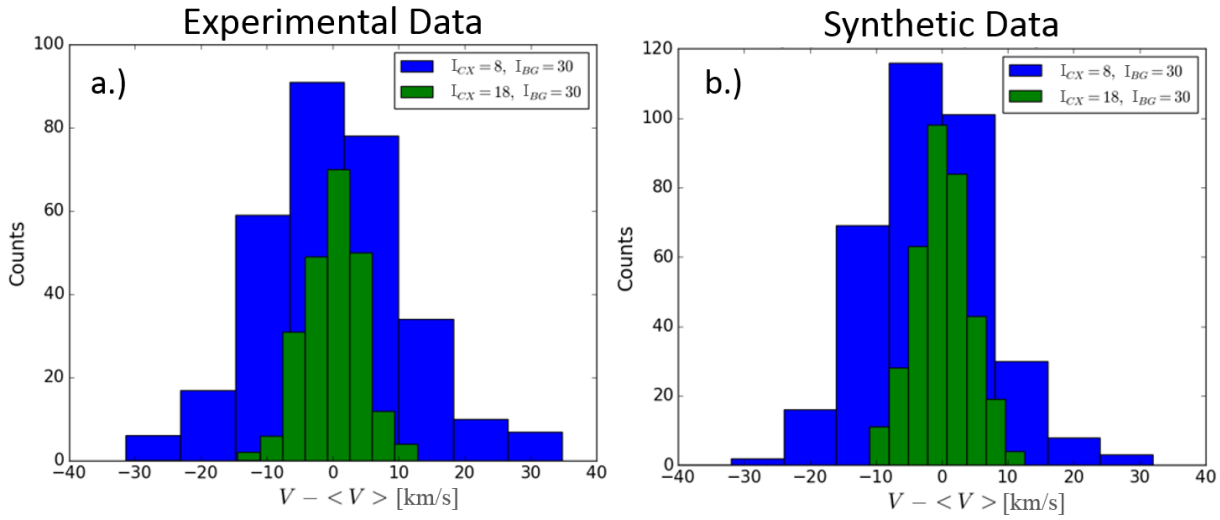

Figure 4.3.: Comparison of noise in fits of a.) real and b.) synthetic IDSII data. The spread in the parameter fits from synthetic data with Poisson noise is similar to the spread in the time-averaged data in the saturated SHAx state, shown in table c.). The radiance parameters I_{CX} and I_{BG} represent the charge exchange and background electron impact parameters fit in Equation 3.4. The units in the given values are nW/(sr cm^2)

At most locations for the dataset collected, the dominant source of uncertainty is the day-to-day calibration uncertainty. This is because the focus for any one day was to gather CHERS data for a specific radial location. Had many radial and toroidal locations been sparsely measured each day, the day-to-day calibration uncertainty could be significantly reduced, possibly to the level of the statistical uncertainty.

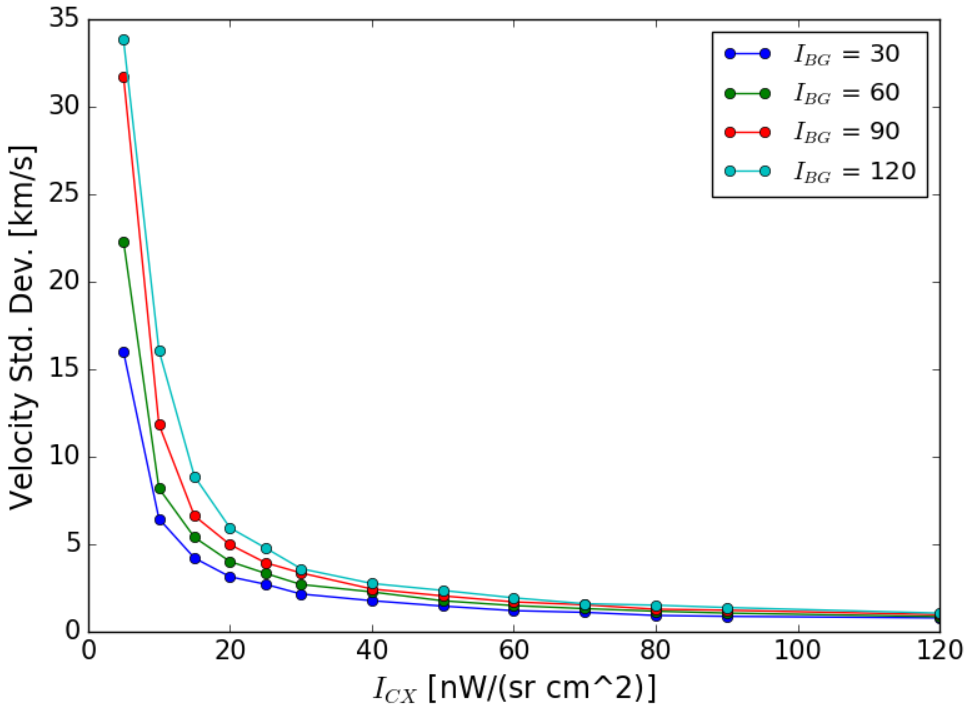

Figure 4.4.: The spread in velocity fits of synthetic data is plotted against charge exchange intensity, I_{CX}, for different electron impact intensities, I_{BG}, in units of nW/(sr cm^2). Each data point represents the standard deviation of 500 velocity fits. The uncertainty scales inversely with the charge exchange signal, and increases with increasing I_{BG} signal for a given I_{CX}.

4.3. Resilience of flow profiles to impurity density

This section will explore the dependence of the flow profile on the total impurity density inferred from the radiance of the charge exchange and electron impact signals. The total light the CHERS diagnostic sees depends on the impurity density of carbon for charge exchange, and oxygen for electron impact excitation, as described by Equation 3.7. The correlation of impurity levels as measured by the charge exchange radiance with velocity profiles in the core and mid-radius is investigated here, as is a simple procedure for adding carbon to the machine to increase light levels and improve velocity resolution in the inboard-most radial

location.

Different machine conditions can cause very different overall impurity levels in the plasma. Figure 4.5 a.) shows the toroidal profile of charge exchange radiance at $r/a = 0.62$, where a day that had particularly high radiance due to high carbon impurity density is highlighted in red. It can be inferred that the increased carbon impurity is proportional to the impurity density levels everywhere in the plasma, since the background electron impact signal increased as well, such that the ratio of the two signals for the CHERS view is the same between high and low radiance days, as shown in Figure 4.5 b.).

The velocity profile is robust to changes in the impurity content of the plasma at the mid-radius of the plasma. The velocity measurements for the same dataset presented in Figure 4.5 are presented in Figure 4.6. During a run day with high impurity density, shown in red in the figure, the radiance from charge exchange was nearly double the average amount. It can be seen that the velocity profiles of data at high and low radiance overlap.

An exception to the robustness of velocity profiles to impurity density is observed in one group of outlier data at $r/a = 0.11$, where higher charge exchange signal correlates to a systematic offset in the axisymmetric velocity of about 4 km/s, as shown in Figure 4.7. The data measured at high radiance at this location was all taken in one day using one absolute wavelength calibration for the day. The importance of the correlation with axisymmetric velocity and the impurity content in the plasma core is muddled by the uncertainty in the absolute wavelength calibration used to obtain absolute velocity measurements. As mentioned previously, the calibration technique has an uncertainty on the order of $\pm$ 3 km/s.

Since the statistical uncertainty depends on the total charge exchange signal, as shown in Figure 4.4, and given that increasing the carbon impurity content increases the charge exchange signal, but does not noticeably affect the flow profiles in the mid-radius, carbon

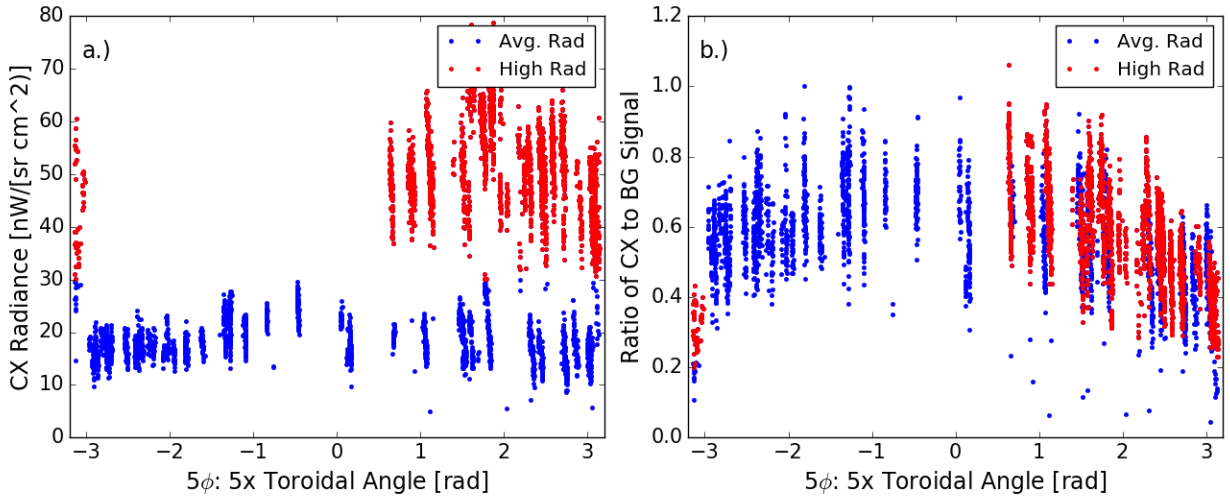

Figure 4.5.: a.) Charge exchange radiance vs. toroidal angle at r/a = 0.62. b.) Ratio of radiance due to charge exchange emission and background electron impact emission. Charge Exchange radiance above 30 nW/sr cm^2 is highlighted in red. The ratio of the charge exchange to background electron impact radiance stays the same despite the higher charge exchange signal levels.

was purposely added to the machine to improve the resolution of inboard most velocity measurements, at $r/a = -0.58$. Charge exchange radiance is weakest here due to attenuation of the neutral beam density. Carbon density in the plasma was increased using an insertable probe with a 1 cm diameter, 3.3 cm long solid graphite tip, shown in Figure 4.10.

Inserting the probe deeper into the plasma caused a proportional increase in carbon signal. Figure 4.8 shows different charge exchange signal for different insertion depths into the plasma, measured from the wall. The overall effect was to increase the total carbon signal when the probe was inserted more than 4 cm beyond the wall. The fall off in the charge exchange signal in time shown in Figure 4.8 is attributed to a fall off in the neutral beam strength, either through attenuation in the plasma, or decrease in the initial beam strength. A similar increase in the background electron impact signal was detected, in line with the previously documented observation that the ratio of charge exchange and electron impact

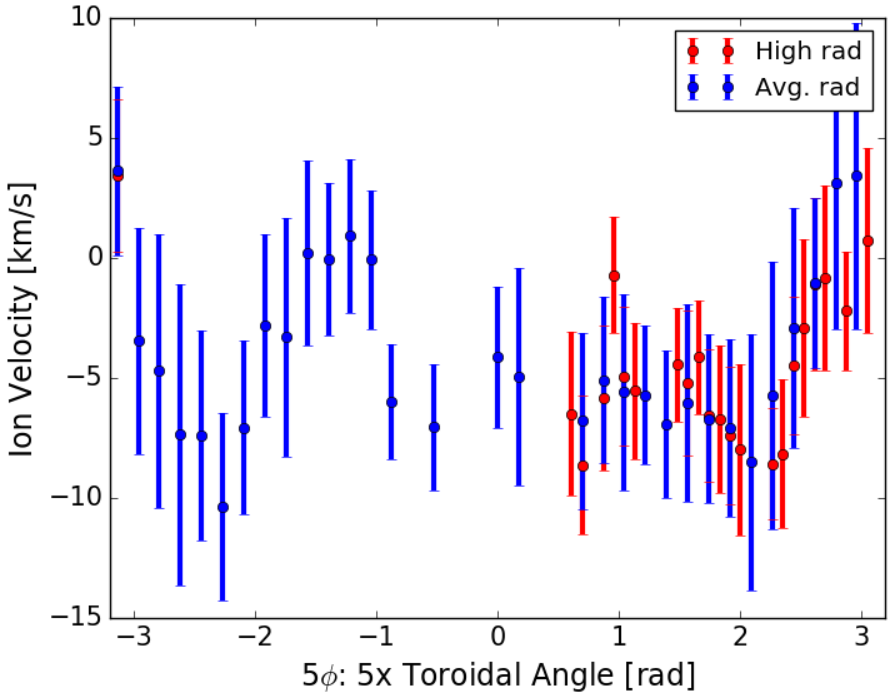

Figure 4.6.: Out-of-plane velocity vs. toroidal angle at r/a = 0.62. Red data indicates high radiance from charge exchange, and blue indicates measurements with average radiance.

signal tends to remain the same. The velocity between the probe insertion and non-insertion seems to not be strongly affected, as is shown in the histogram in Figure 4.9. The spread in velocity at a fixed toroidal angle is centered on the same velocity for days with and without the carbon probe.

In summary, velocity profiles at the mid-radius are not noticeably affected by the impurity content of the plasma. This observation motivated the insertion of a carbon tip into the plasma to increase the overall signal levels in at $r/a = -0.58$ and improve the resolution in velocity measurements. A 4 km/s systematic offset in axisymmetric out-of-plane velocity correlates to high impurity density in the plasma core at $r/a = 0.11$, possibly indicating that the axisymmetric velocity in the plasma core depends on the impurity content of the

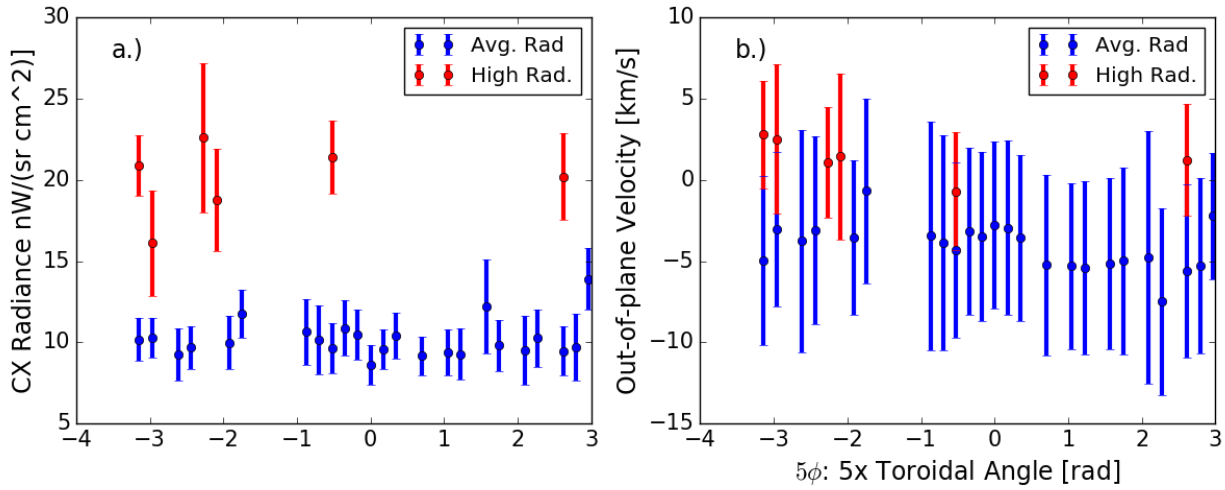

Figure 4.7.: a.) Charge exchange radiance vs. toroidal angle at r/a = 0.11. b.) Out-of-plane velocity vs. toroidal angle at r/a = 0.62. Red data indicates high radiance from charge exchange, and blue indicates measurements with average radiance.

plasma. The data at $r/a = 0.11$ at high radiance was a sufficiently strong outlier that it was removed from consideration in the dataset used to create parameterized profiles of flow at that location.

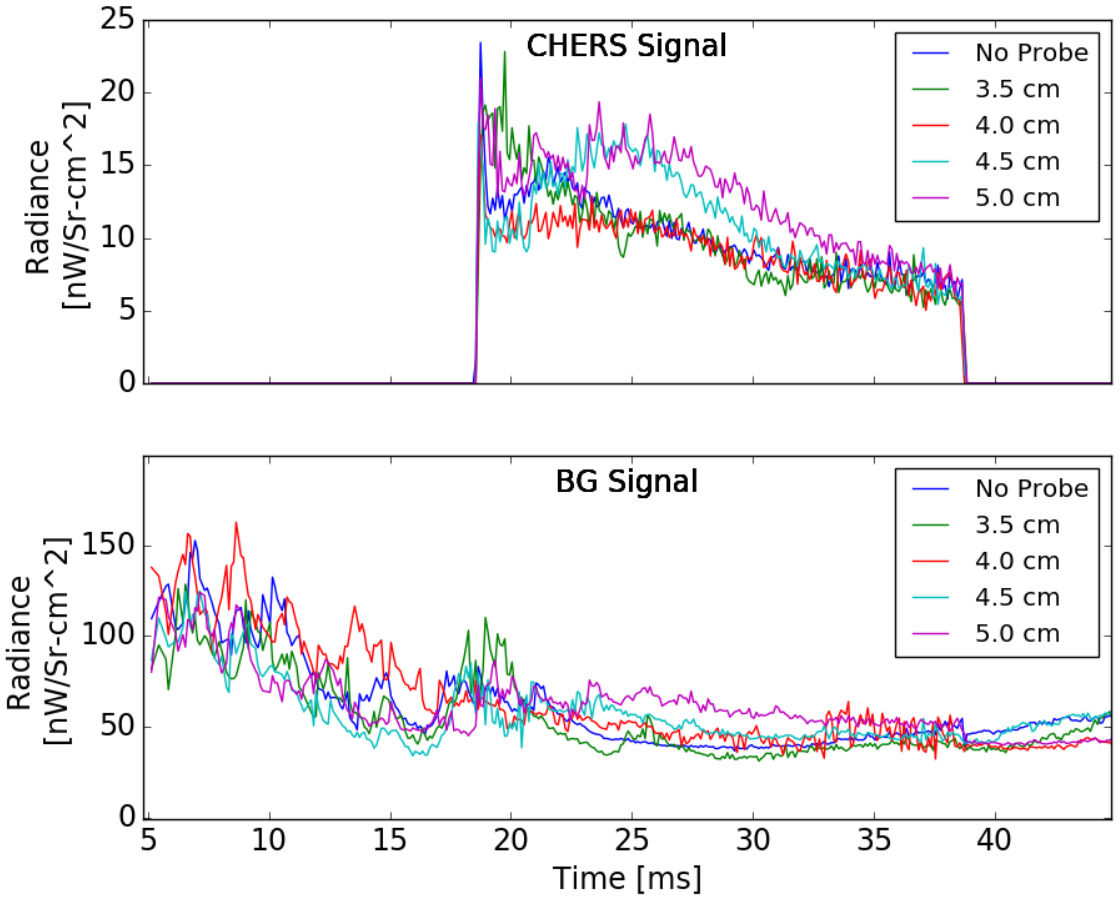

Figure 4.8.: Charge exhange radiance vs. time (top) and electron impact radiance from background emission vs. time (bottom) measured at at $r/a = -0.58$ for different carbon probe insertion depths. Insertion depth measurements are relative to the inner surface of the Aluminum shell.

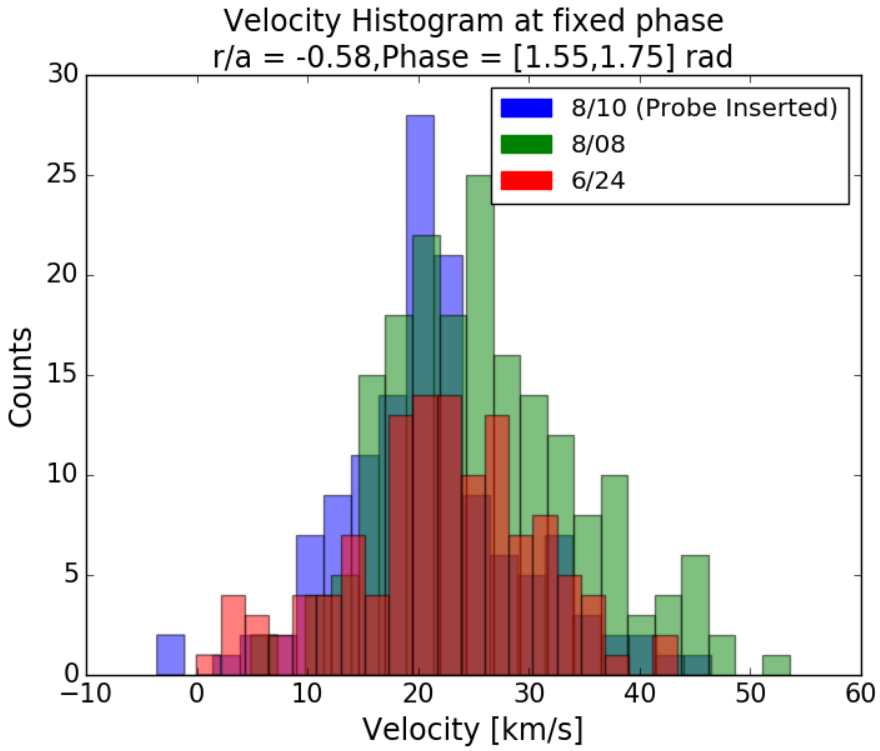

Figure 4.9.: Histogram of velocity at a fixed n=5 locking phase for different days, including when the carbon probe was inserted.

Figure 4.10.: 1 cm diameter, 3.3 cm long solid graphite tip of an insertable probe used to increase carbon levels in the machine. Deformation in the tip of the graphite is due to plasma exposure after two run days with 500 kA QSH plasmas.

4.4. Characterization of 3D flows in SHAx

In this section the toroidal flow and out-of-plane flow data are presented. Toroidal profiles for both flow directions at different radial locations are shown, and then the data is Fourier decomposed along the toroidal direction. Radial profiles of the harmonic amplitudes are presented and discussed.

The velocity profiles obtained by scanning helical toroidal angle at different radial locations for the out-of-plane and toroidal velocity are shown in Figure 4.11 and Figure 4.12 respectively. The error bars represent the standard deviation in the data, while the error bar colors represent data collected on different days for a given radial location. There is good overlap in the flow measurements between data from different days at the same location. The agreement of the data between days is important because absolute wavelength calibration ends up being the largest source of uncertainty in the profile measurements, as is discussed in Section 4.2. The standard deviation of the mean is on the order of the circular symbol size for the large majority of the data. The parameterized profiles are shown in dotted black lines through each profile.

The relation between the toroidal profiles of velocity can be seen more clearly in Figure 4.13 which show the data as a contour plot overlaid on a puncture plot of representative helical flux surfaces for the DNB-ϕ plane. The contour plots do not use the parameterized profile to fill empty spaces between data, but instead interpolates between the data using an unstructured triangular grid. For the out-of-plane velocity, flow out of the page is positive. For toroidal velocity flow in the direction of the helical toroidal angle is positive. Negative values of r/a denote the inboard side of the machine.

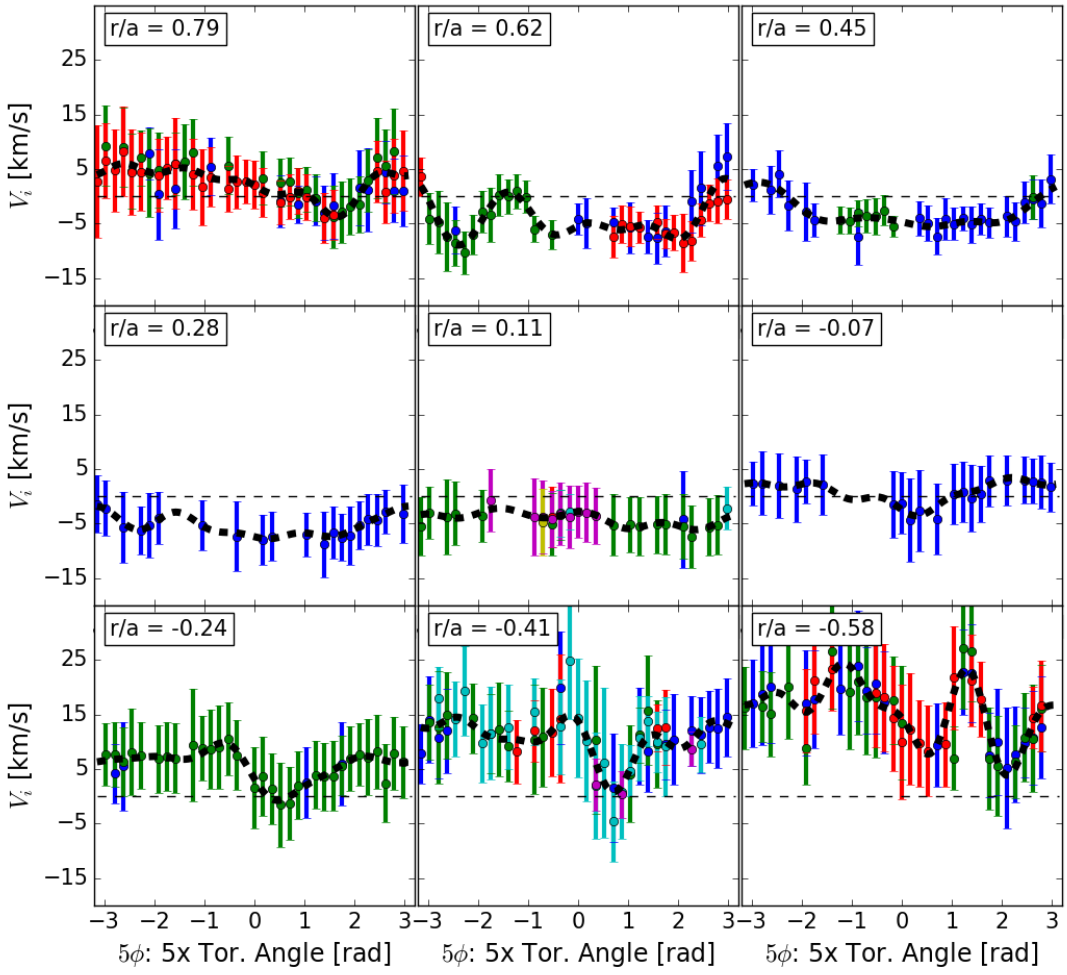

Figure 4.11.: Out-of-plane velocity measurements for different radial locations. Different colors within each plot represents different days on which data was taken for that location. Data that is the same color between plots are not necessarily taken on the same day. Error bars represent the standard deviation in the data, the standard deviation in the mean is on the order of the circular data points for the large majority of the data.

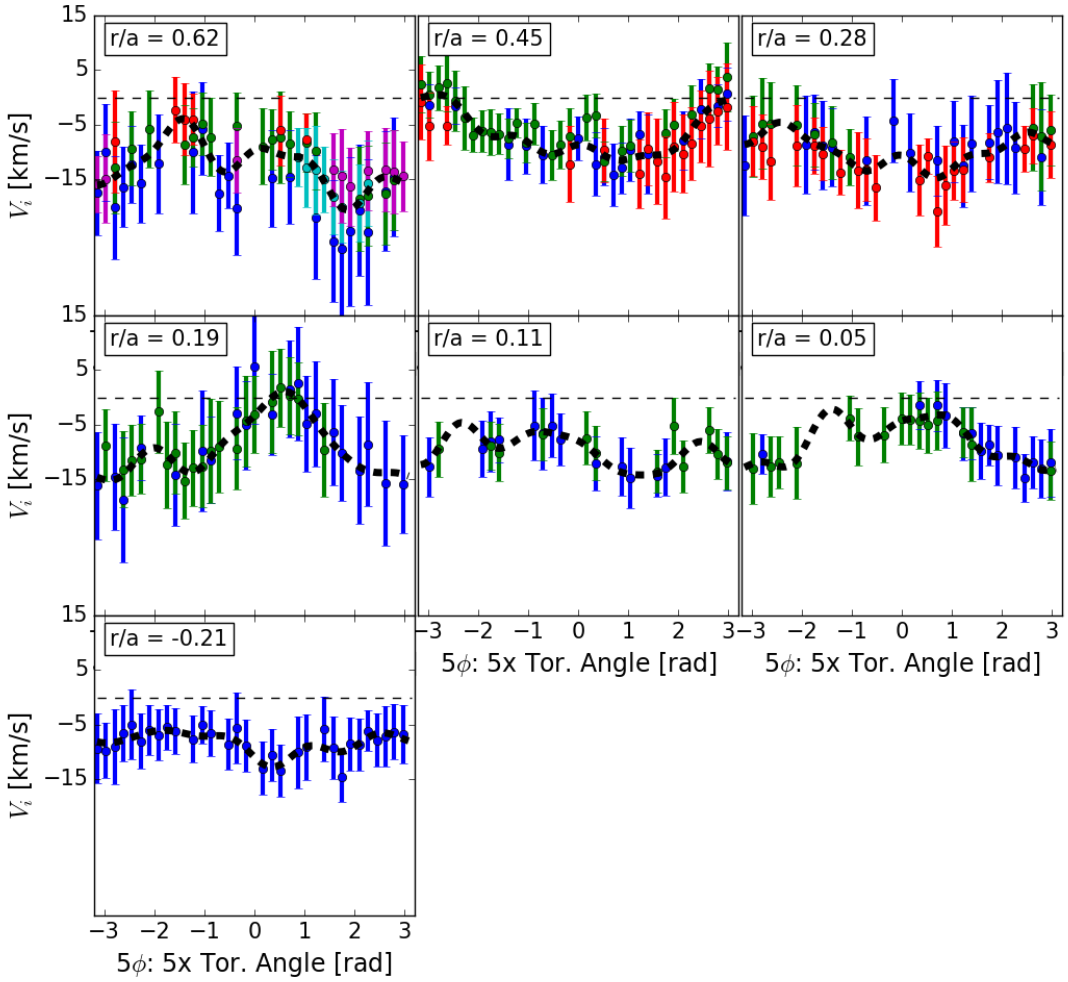

Figure 4.12.: Toroidal velocity measurements for different radial locations. Different colors within each plot represents different days on which data was taken for that location. Data that is the same color between plots are not necessarily taken on the same day. Error bars represent the standard deviation in the data, the standard deviation in the mean is on the order of the circular datapoints for the large majority of the data.

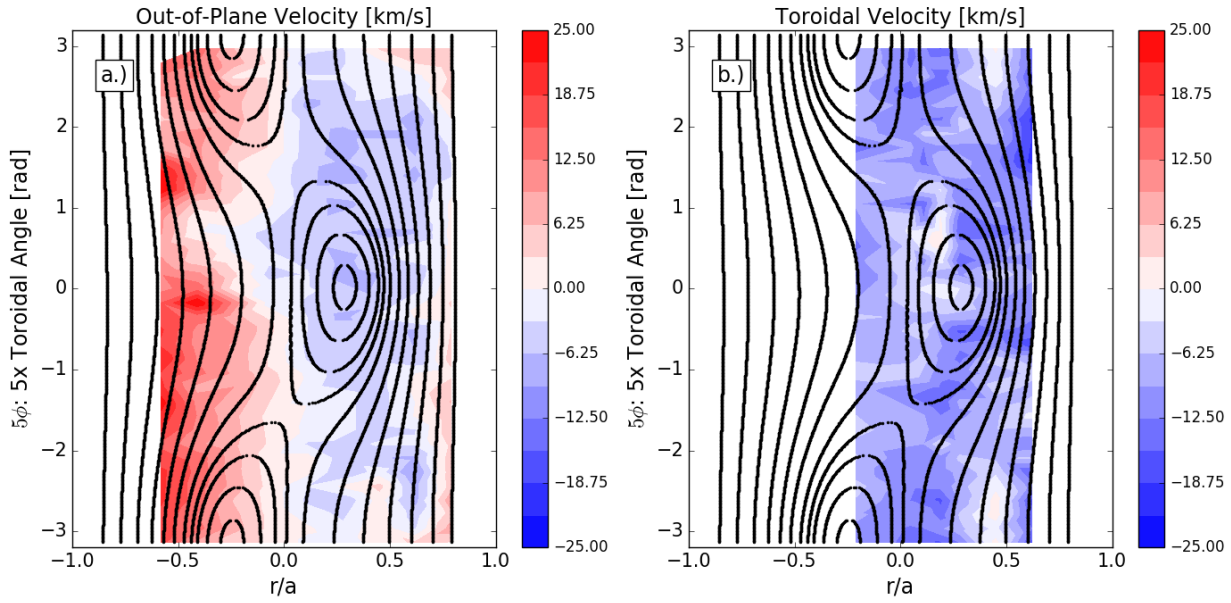

Figure 4.13.: a.) Out-of-plane velocity contours, where flow out of the page is positive. b.) Toroidal velocity contours. Flow in the positive helical toroidal angle is positive. Negative r/a denotes the inboard side of the machine. The colorbar step size represents the ± 3 km/s systematic uncertainty.

4.4.1. Axisymmetric component of the flow

This section will cover the axisymmetric flow obtained from the $n = 0$ component of the parameterized profiles described in Section 4.1. The radial profiles of the axisymmetric out-of-plane flow and the axisymmetric toroidal flow are presented in Figure 4.14. The error bars on the harmonic amplitudes and phases represent the spread in the those parameters from fitting the parameterized profile to ten random subsets of the total dataset. The toroidal flow profiles are relatively uniform throughout the measurement region. It should be noted that there was an axisymmetric offset measured between two profiles at $r/a = 0.28$, discussed in Appendix A. The out-of-plane flow, however, shows strong changes over radius, with significant asymmetry between the inboard ($r/a < 0$) and outboard sides. This may be related to the toroidal geometry of MST, where incompressible flow arguments suggest that the flow would be stronger on the inboard side where the volume is smaller compared to the outboard, although density profile measurements are not available to fully test this. Inboard/outboard flow asymmetry will be addressed again in Section 5.3.3. Not only is the inboard flow significantly stronger than the outboard, but it is also rigid-rotor-like, whereas the outboard out-of-plane flow turns over at the mid-radius. The outboard flow also reverses in the edge, though this is measured at $r/a = 0.79$, so it is possible the inboard flow reverses as well, but in the region that has not been measured.

The out-of-plane flow profile is very similar to the poloidal velocity profile recently measured in PPCD[1], including the inboard/outboard asymmetry and sign reversal at the outboard edge. The PPCD flow profiles are reproduced in Figure 4.15. The PPCD flow is reported in terms of poloidal flow vs flux surface, ρ. The poloidal flow results in a change in sign on the outboard side relative to the "out-of-plane" measurements reported here, as shown in Figure 3.4. The overall similarities in the axisymmetric flow between PPCD and

SHAx suggests that the factors influencing the poloidal axisymmetric flow are not unique to SHAx, but instead generic to the RFP.

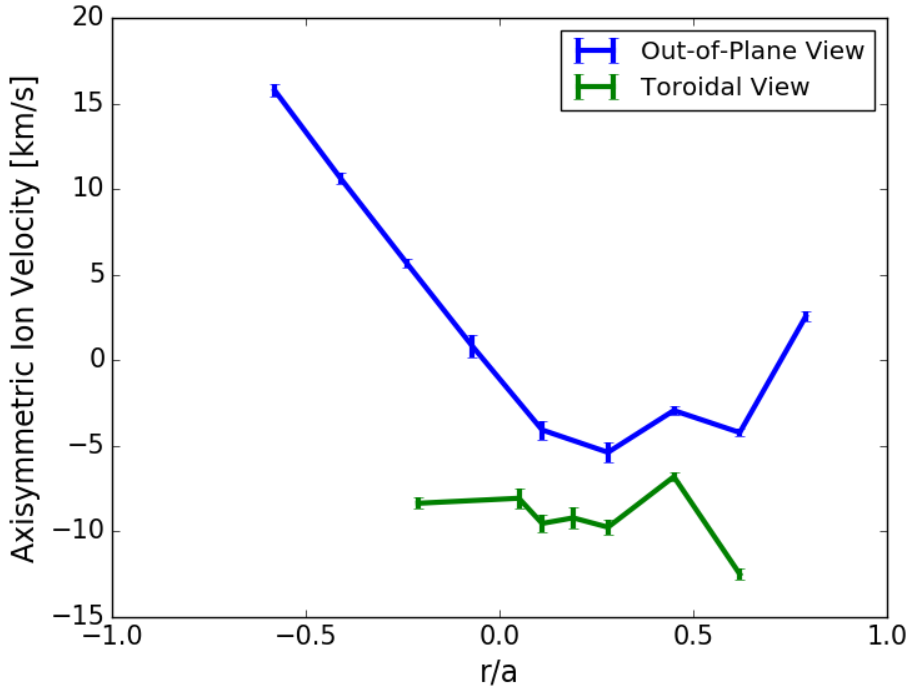

Figure 4.14.: Axisymmetric out-of-plane (blue) and toroidal (green) flow profile. Error bars represent the variation in the V_0 parameter from fitting ten random subsets of the total data.

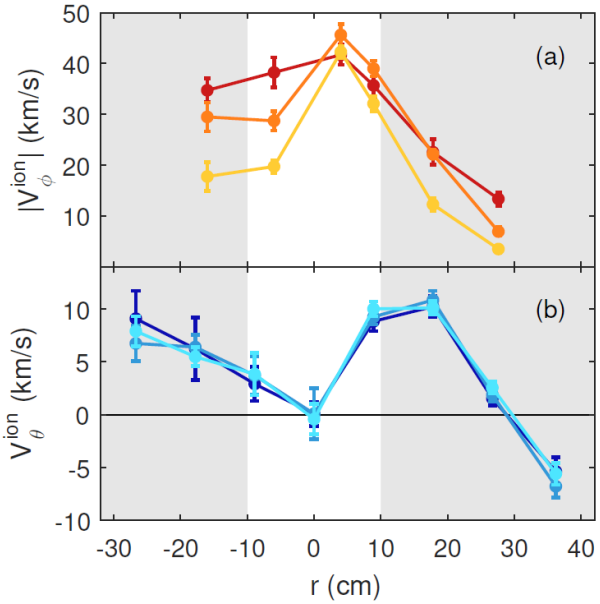

Figure 4.15.: Axisymmetric (a) toroidal and (b) poloidal flow profiles. The different profile lines indicate the profile evolution in time, where each line indicate 2 ms time windows from darkest to lightest, starting at 12 ms. The shaded region indicates where tearing modes are resonant. The poloidal flow is opposite in sign from the out-of-plane flow presented in SHAx plasmas due to the sign reversal of $\hat{\theta}$ moving from inboard to outboard. Figure reproduced from Craig *et al.* (2019)[1].

4.4.2. Non-axisymmetric component of the flow

The non-axisymmetric component of the data is shown as contours in Figure 4.16. Comparing to Figure 4.13, it can be seen clearly that the localized regions of reduced flow in Figure 4.13 are locations the non-axisymmetric flow is canceling out the axisymmetric flow.

The profiles of the harmonic amplitude and phase from the fit to Fourier harmonics described in Section 4.1 are given in Figures 4.17, 4.18 and 4.19. As with the axisymmetric profiles, the error bars for the harmonic amplitude and phases come from the spread in fitting ten equally sized but randomly selected subsets of the total dataset. The error bars on the harmonic amplitudes are comparable to the uncertainty in the mean for the data at individual locations in real space.

The $n = 5$ harmonic of the toroidal flow is dominant at all measured locations. Generally, it is phase aligned with the magnetic axis, and appears to phase flip when moving across the radial location of the helical magnetic axis, seen visually in Figure 4.16 b.). The out-of-plane velocity is dominated by the $n = 5$ velocity for $|r/a| < 0.5$. For all harmonics, the radial profile is hollow. This is inconsistent with the peaked profile results in high-dissipation computations, discussed in Section 2.2.1. The hollow $n = 5$ profile is, however, similar to the one measured previously in growing, rotating $n = 6$ QSH modes on MST in reversed plasmas[2], shown in Figure 2.9. In both the locked, $n = 5$ saturated SHAx case and the rotating $n = 6$ growing QSH case, the velocity peaks off-axis, is small near the center, and has strong contribution from higher n harmonics at $r/a = 0.62$ ($\rho/a = 0.55$ for axisymmetric flux surfaces in Figure 2.9). The saturated SHAx flow is more global, and there is still strong $n = 5$ flow at the outermost CHERS measurement location, $r/a = 0.79$.

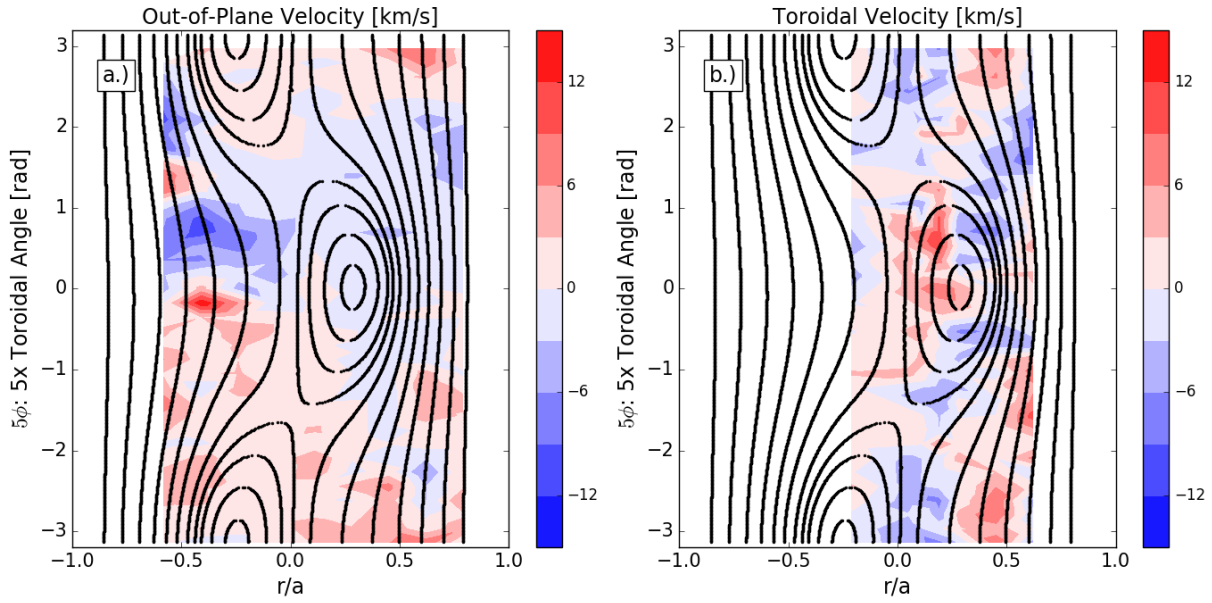

Figure 4.16.: a.) Out-of-plane velocity contours, where flow out of the page is positive, and b.) toroidal velocity contours with axisymmetric flow removed. where flow in the positive helical toroidal angle is positive. Colorbar intervals represent typical systematic uncertainty.

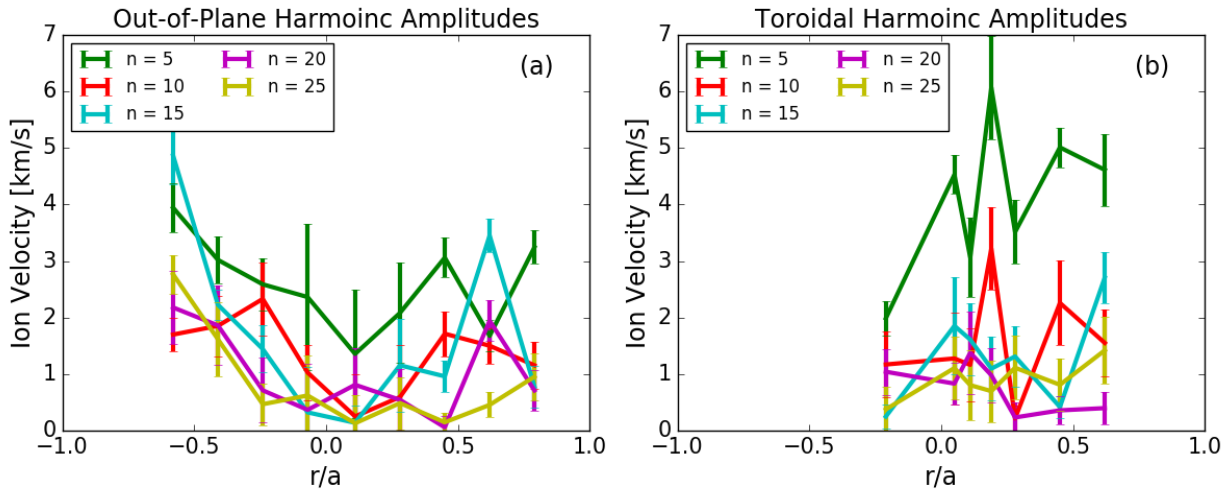

Figure 4.17.: Out-of-plane harmonic velocities,(a), and toroidal harmonic velocities, (b).

As can be inferred from Figure 4.11, the $n > 5$ harmonics at $r/a < 0.5$ act to shape a single extremum in the toroidal profiles. At $r/a = 0.62$ and $r/a = -0.58$, however, there are two well resolved peaks in the out-of-plane flow. Both locations have very similar features. Figure 4.20 shows a comparison of the two toroidal profiles of out-of-plane flow side-by-side. This is the same data that is presented in Figure 4.11, but the axes have been changed from out-of-plane flow to poloidal flow, and the the x-axis of the inboard chord, $r/a = -0.58$, is shifted by π so that its zero angle aligns with the helical magnetic axis on the inboard side. The two extrema of the profiles occur within 1/2 a radian of eachother toroidally. The similarity between the two profiles measured on opposite sides of the geometric axis suggests that the $n > 5$ flow structure is radially localized, but not poloidally localized.

The $n > 5$ structure is also robust to changes in plasma current. The velocity profile at $r/a = 0.62$ was measured in lower plasma current SHAx states to see if the double-peaked structure observed at that location persists. The profiles were measured at 340 kA and 420 kA. The profile was very similar between 500 kA and 420 kA, but then relaxed significantly for 340 kA, as shown in Figure 4.21.

These observations show strong evidence that $n > 5$ structure is present, and it is dominant at certain radial locations in the saturated SHAx state. This result is inconsistent with the high-dissipation computation of an SH state where dominant helicity $\boldsymbol{E} \times \boldsymbol{B}$ flow is the sole source of the flow. It should be noted that the region where the two peaks are measured is the same region where the $n = 7 - 10$ tearing modes are resonant. It is possible that one or more of these sub-dominant tearing modes are responsible for the observed double peaked structure. The gyration of the resonant flux surfaces obtained from V3FIT and plotted at four different toroidal locations in Figure 4.22 illustrate how the surfaces sweep in and out of view for the two locations under discussion. The nine out-of-plane viewing locations are plotted as dots along the DNB beam path, where $r/a = 0.62$ and $r/a = -0.58$ are red dots, and the other seven are black dots.

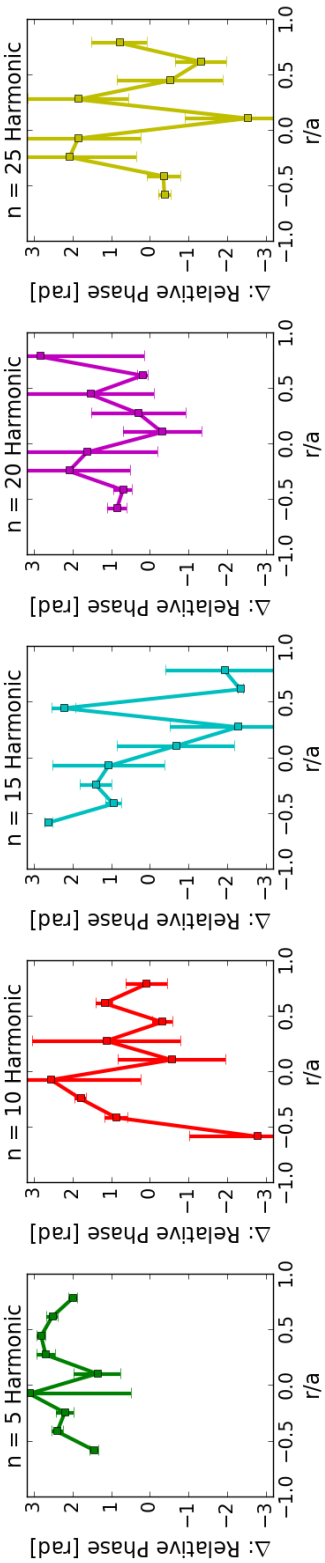

Figure 4.18.: Profiles of measured phases for the out-of-plane velocity harmonics

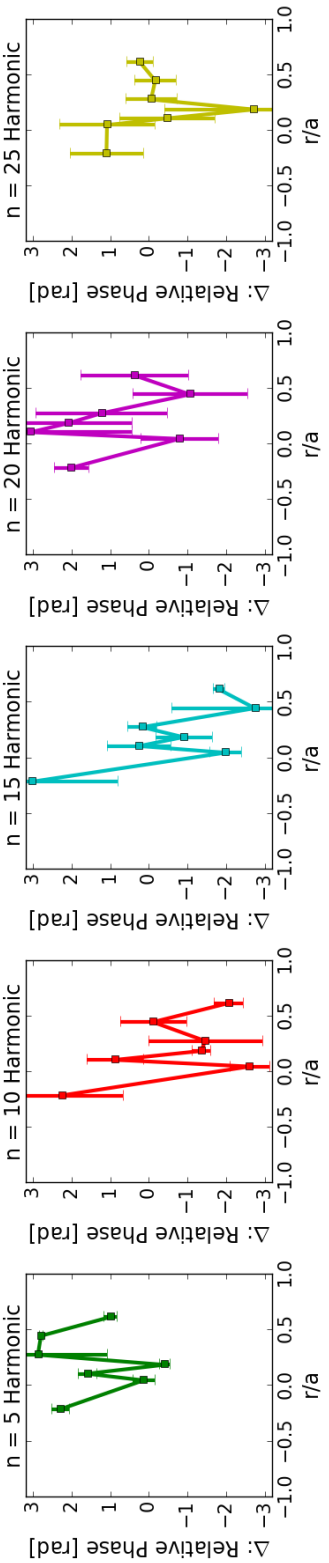

Figure 4.19.: Profiles of measured phases for the toroidal velocity harmonics

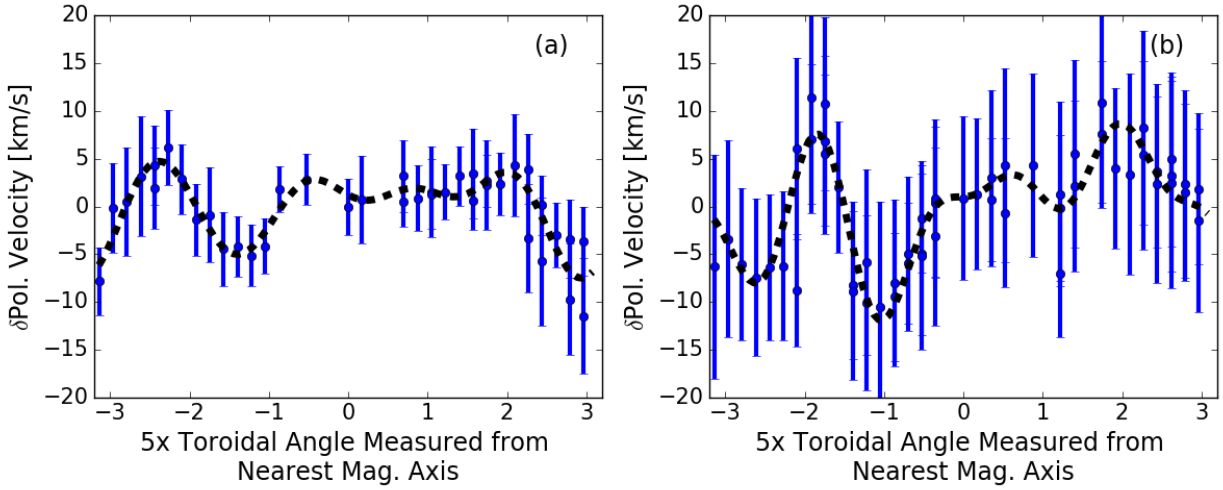

Figure 4.20.: (a) r/a = 0.62 and (b) r/a = -0.58 non-axisymmetric velocity vs toroidal angle comparison. The velocity has been converted from out-of-plane velocity to poloidal velocity, and the x-axis of (b) has been shifted by π so 0 rad aligns with the inboard helical magnetic axis.

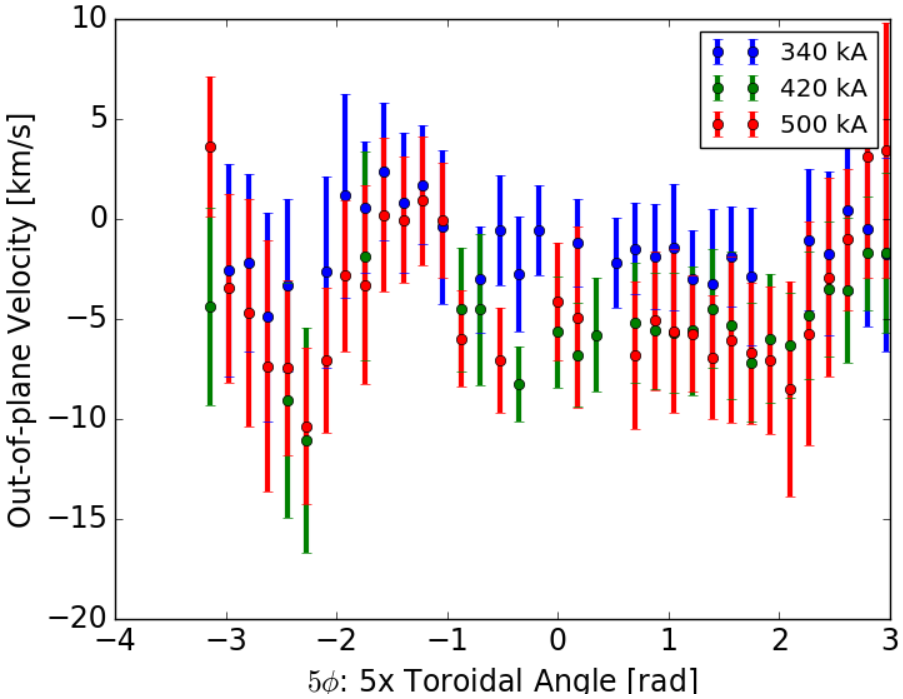

Figure 4.21.: Average velocity profile for different plasma currents at $r/a = 0.62$.

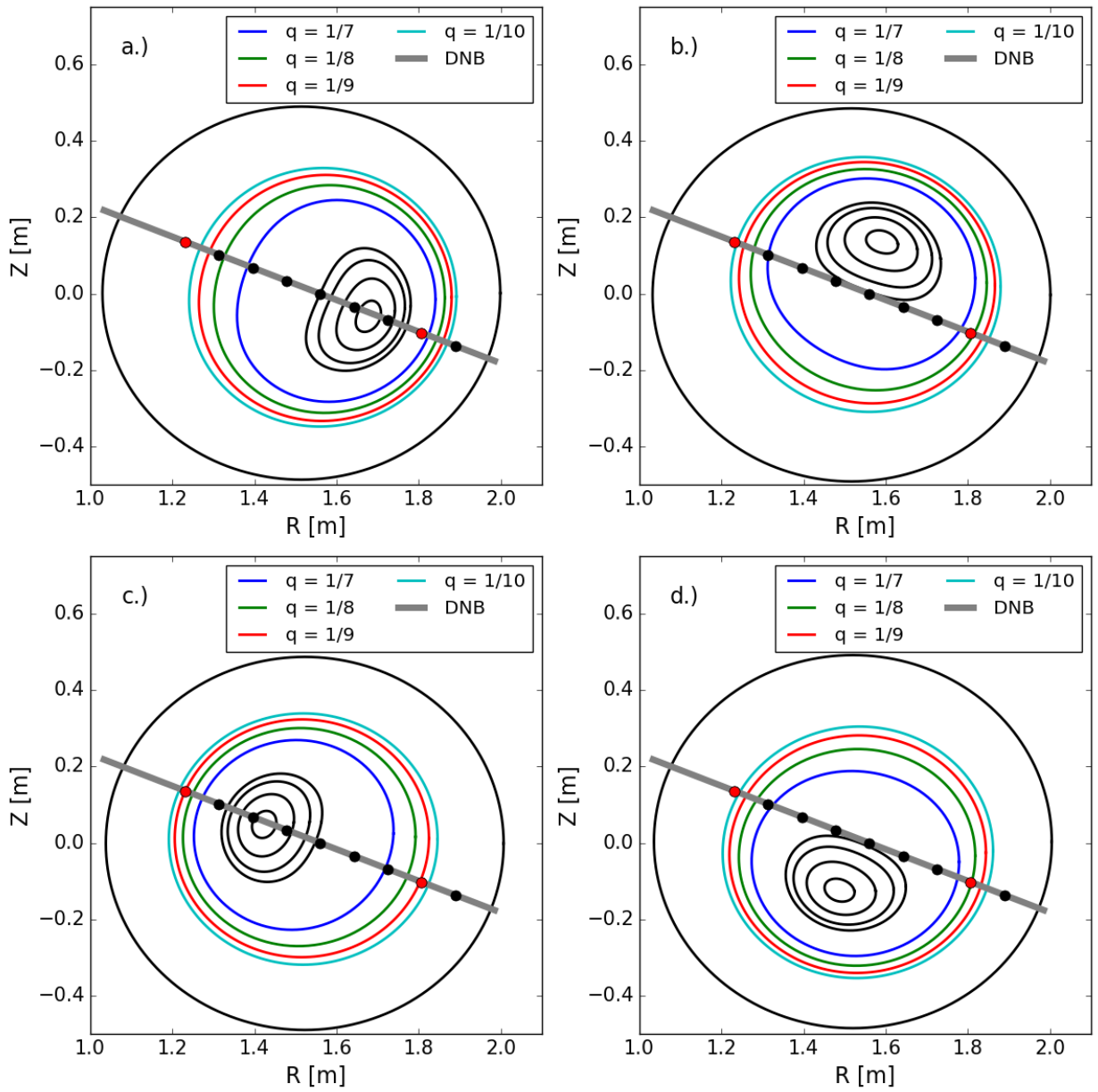

Figure 4.22.: Rational flux surfaces where tearing modes are resonant are plotted at a.) $\phi_{hel} = 0$ rad, b.) $\phi_{hel} = \pi/2$ rad, c.) $\phi_{hel} = \pi$ rad, and d.) $\phi_{hel} = -\pi/2$ rad. The DNB line-of-sight is shown as the gray line, the two out-of-plane viewing chords, $r/a = 0.62$ and $r/a = -0.58$, that see the majority of the rational flux surfaces plotted as red dots, and the other seven measurement locations are plotted as black dots

4.5. Summary

Toroidal and radial profiles of the toroidal and the out-of-plane plasma flow are obtained by aggregating local CHERS velocity measurements over the saturated SHAx time period for many plasma shots. The axisymmetric part of the radial profiles reveal a relatively uniform toroidal flow and an asymmetric flow out-of-plane from the plane mapped out as the plasma is rotated through the DNB line-of-sight. The out-of-plane flow is rigid-rotor-like on the inboard side, but on the outboard side it peaks at the mid-radius and reverses sign at the edge. The similarity of the out-of-plane flow to PPCD flows suggest that the profile is not unique to the SHAx state.

The non-axisymmetric flow profile is dominantly $n = 5$ and hollow in both the toroidal and out-of-plane directions for $r/a < 0.5$. At $r/a = 0.62$ and $r/a = -0.58$, the toroidal profile of the out-of-plane flow has two well resolved extrema. The $n = 7 - 11$ tearing modes are resonant in the vicinity of these two measurement locations, possibly contributing to the $n > 5$ structure.

The analysis of the experimental data up to this point is done in the absence of interpretation of key physics at play. To further understand the influence of specific physical effects on the flow profiles, such as toroidicity, two-fluid effects, and dissipative effects, input is needed from simulations and modeling. The next chapter will investigate these topics using comparisons to NIMROD simulations that have achieved a QSH state through dissipative means, or by application of a limited periodicity boundary condition in cylindrical or toroidal geometries.

References

[1] D. Craig, E. H. Tan, B. Schott, J. K. Anderson, J. Boguski, D. J. Den Hartog, T. Nishizawa, M. D. Nornberg, and Z. A. Xing, "Intrinsic flow and tearing mode rotation in the RFP during improved confinement," *Physics of Plasmas*, vol. 26, p. 072503, 7 2019.

[2] D. A. Ennis, D. Craig, S. Gangadhara, J. K. Anderson, D. J. Den Hartog, F. Ebrahimi, G. Fiksel, and S. C. Prager, "Local measurements of tearing mode flows and the magnetohydrodynamic dynamo in the Madison Symmetric Torus reversed-field pinch," *Physics of Plasmas*, vol. 17, no. 8, p. 082102, 2010.

5. Comparison to NIMROD simulations

5.1. Introduction

To further interpret the experimental results and help develop metrics for the importance of toroidicity, dissipation, and two-fluid effects on flow, it is useful to compare the measured flow to predictions from simulations. No simulation that has achieved a QSH state has done so without simplification of the problem in some way. This is partly because running simulations at experimentally relevant Lundquist number and Prandtl number is too computationally expensive. As mentioned previously, SpeCyl simulations either relies on very high dissipation to damp sub-dominant modes and create an SH state, or the constant application of a helical perturbation at the plasma boundary to create a QSH state. In this chapter, QSH simulations run at both high and low Hartmann number using the initial-value extended-MHD NIMROD code[1] are presented. Details of running NIMROD can be found in the theses of Josh Sauppe[2] and Jake King[3], whose work are on NIMROD simulations relevant to MST. In order to achieve QSH at high Hartmann number, a special limited periodicity boundary condition is used. The NIMROD code uses a 2D finite element mesh and a periodic Fourier components in the third direction. NIMROD is used to solve the extended MHD system of

equations:

$$\frac{\partial n}{\partial t} = -\nabla \cdot (n\boldsymbol{V}) + \nabla \cdot (D_n \nabla n) \tag{5.1}$$

$$\rho\Big(\frac{\partial \boldsymbol{V}}{\partial t} + \boldsymbol{V} \cdot \nabla \boldsymbol{V}\Big) = \boldsymbol{J} \times \boldsymbol{B} - \nabla p + \nu\rho\underline{\mathbf{W}} \tag{5.2}$$

$$\frac{3}{2} n\Big(\frac{\partial T}{\partial t} + \boldsymbol{V} \cdot \nabla T\Big) = -p/2\nabla \cdot \boldsymbol{V} + \nabla \cdot \chi n \nabla T + \eta \boldsymbol{J}^2 \tag{5.3}$$

$$\frac{\partial \boldsymbol{B}}{\partial t} = -\nabla \times \boldsymbol{E} + \kappa \nabla \nabla \cdot \boldsymbol{B} \tag{5.4}$$

$$\boldsymbol{E} = -\boldsymbol{V} \times \boldsymbol{B} + \eta \boldsymbol{J} \tag{5.5}$$

$$\mu_0 \boldsymbol{J} = \nabla \times \boldsymbol{B} \tag{5.6}$$

where $\underline{\mathbf{W}} = \nabla \boldsymbol{V} + (\nabla \boldsymbol{V})^T - \frac{2}{3}\underline{\mathbf{I}}(\nabla \cdot \boldsymbol{V})$. Direct comparisons to the experiment are made by analyzing output velocities in simulations at comparable locations to the experimental CHERS measurements. Effects of toroidal geometry, high and low dissipation, and two-fluid physics are a subset of the all of the parameters that could be important to the plasma, but the analysis operates under the paradigm that these will have the largest effects on the observable non-axisymmetric plasma flows. The simulations were developed by Urvashi Gupta, who ran the low-viscosity cases, and then high-viscosity cases based on those simulations were run by Karsten McCollam.

5.2. Simulation Setup

Four simulations are presented and compared to the experimental data to directly test the impact of toroidicity, high dissipation, and a limited periodicity boundary condition. Every simulation has in common the parameters listed in Table 5.1. The viscosity is uniform, while the resistivity is flat over the majority of the core, but then increases sharply at the edge.

The thermal conductivity is isotropic, and the plasma beta is an artificially low 0.01% in order to avoid pressure driven modes.

Three of the four simulations use a limited periodicity boundary condition. Similar to V3FIT, these NIMROD computations limit the simulation to 1/5 of the torus or cylinder to enforce an $N = 5$ periodic boundary condition. Since the 2D mesh is in the R, Z plane and the periodic Fourier harmonics are in the toroidal direction, the effect is that all of the toroidal modes have an $N = 5$ periodicity to them. By removing many sub-dominant modes, the strength of the $n = 5$ mode is enhanced, and QSH is achieved during parts of the simulated evolution. The Fourier components in the parameterized flow profiles constructed from experimental data can easily be compared to the NIMROD Fourier components.

The simulations differ according to Table 5.2. Simulations A and B in Table 5.2 switch between cylindrical and toroidal geometry, testing the impact of toroidal effects on the flow profiles. Simulations B and C change from a low viscous dissipation (Pm = 20) to high viscous dissipation (Pm = 2000), while keeping the resistivity the same, in a toroidal geometry to test the impact of viscosity on the flow profiles. The mechanisms that cause net axisymmetric flow in MST plasma are not adequately simulated in NIMROD, so the axisymmetric flow is not considered in these comparisons. From previous work[4] we know to expect that the high dissipation simulations should achieve QSH without a limited periodicity boundary condition. Simulations C and D are run at high viscosity with and without the limited periodicity boundary condition to test what effects it has on the velocity profiles.

The magnetic and kinetic energy evolution for each simulation are shown in parts a-d of Figure 5.1 and Figure 5.2 respectively. The time points used in the direct comparisons to the experiment is shown for each plot as dotted black lines which will be used in averaging radial profiles of mode amplitudes. The time dynamics for each simulation show features that are

Parameter	Value
Resistivity: η_0	2.5×10^{-5}
Resistivity profile: $\eta(r)$	$\eta_0(1 + 9r^{30})^2$
Viscosity profile: $\nu(r)$	flat
Thermal Conduction	Isotropic
Lundquist #	4×10^4
β	0.01 %
R_0/a	3.0

Table 5.1.: Relevant simulation run parameters.

	Sim. A	Sim. B	Sim. C	Sim. D
Periodicity B.C.	N = 5	N = 5	N = 5	N = 1
Geometry	Cyl.	Tor.	Tor.	Tor.
Hartmann #	8900	8900	894	894
Prandtl #	20	20	2000	2000

Table 5.2.: Key parameter changes between simulations.

interesting in their own right, such as the dithering of the $n = 5$ and $n = 10$ modes in plot c.) of the two figures, but the scope of analysis is limited to comparison to experimental data, which is in a saturated SHAx state. The most important aspect of the time evolution is that the $n = 5$ magnetic field is dominant over other modes during the time for which velocity data is being considered. As shown in Figure 5.1, in the high Hartmann number simulations, $n = 5$ magnetic energies reach saturated values of about 3%, whereas in the low Hartmann number simulations, they are double that at about 6%. The simulations at low Hartmann number do not strictly reach a steady $n = 5$ QSH state, but it does reach a flat top for many Alfvén times.

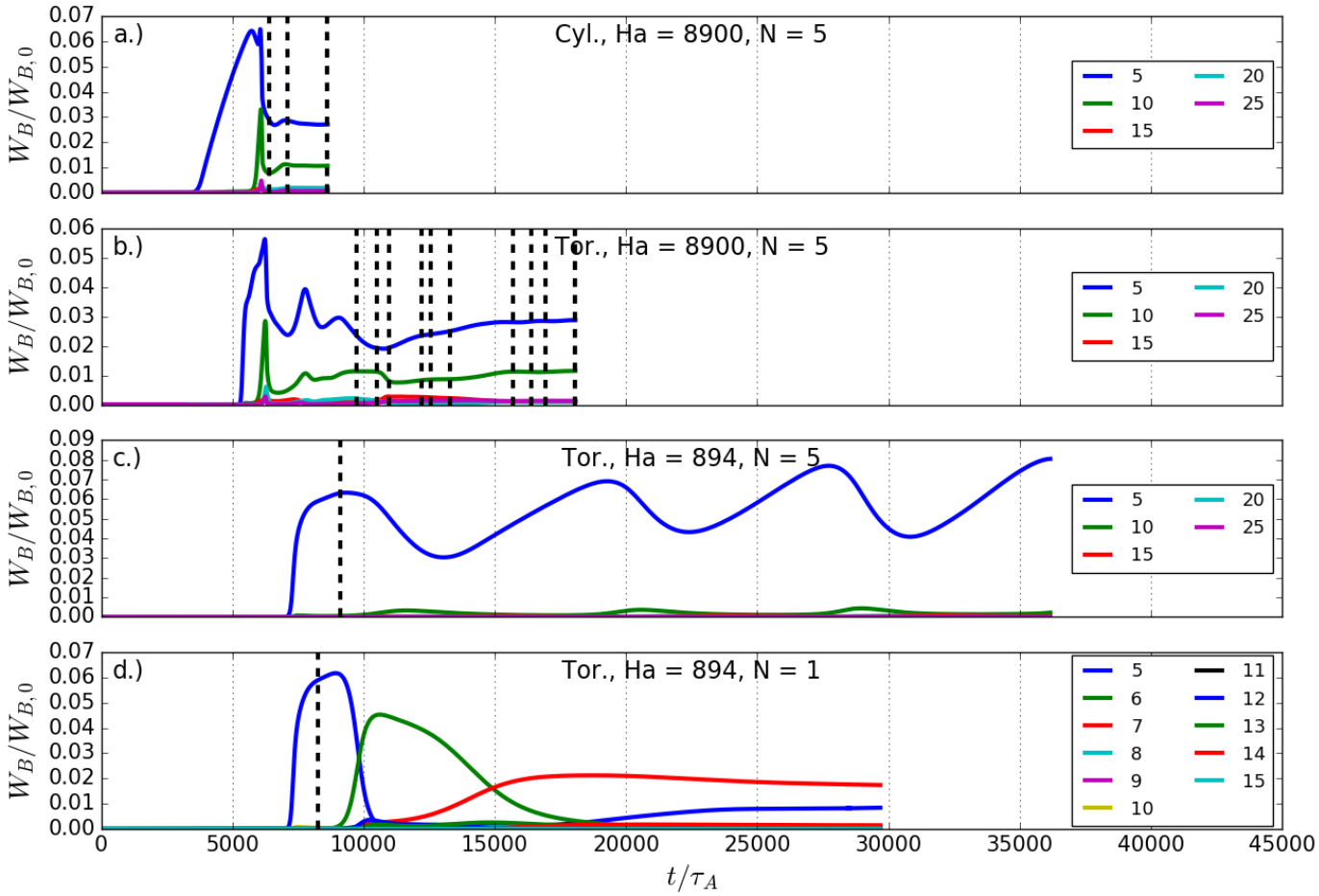

Figure 5.1.: Time evolution of the total magnetic energy per mode, normalized by the axisymmetric magnetic energy, $W_{B,0}$, for NIMROD simulations in a.) cylindrical geometry, Ha = 8900, N = 5 periodicity, b.) toroidal geometry, Ha = 8900, N = 5 periodicity, c.) toroidal geometry, Ha = 894, N = 5 periodicity, d.) toroidal geometry, Ha = 894, N = 1 periodicity. Note the difference in y-axis scales. Dotted black lines indicate the time points NIMROD is evaluated at for average mode amplitudes.

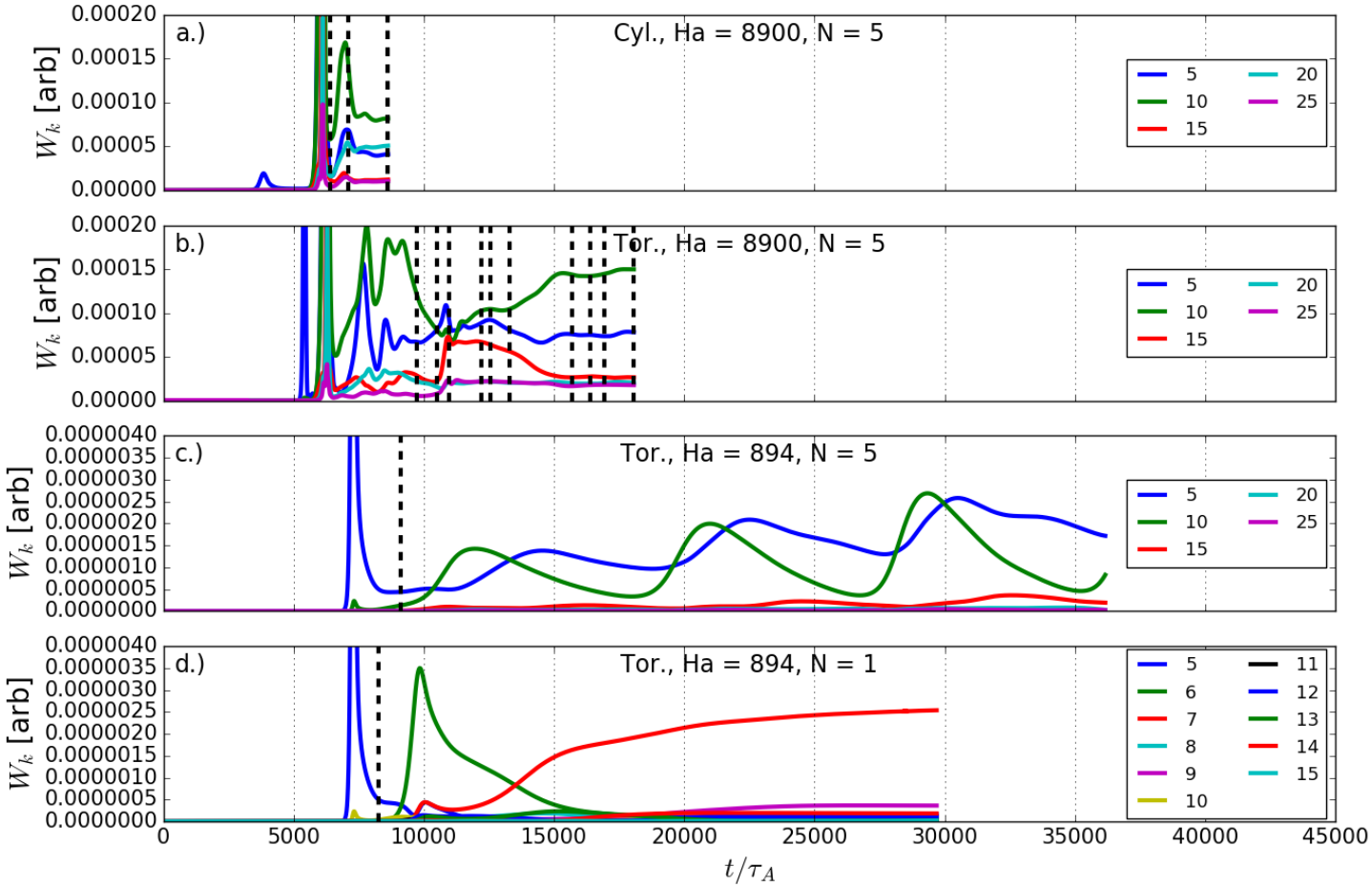

Figure 5.2.: Time evolution of the total kinetic energy for NIMROD simulations in a.) cylindrical geometry, Ha = 8900, N = 5 periodicity, b.) toroidal geometry, Ha = 8900, N = 5 periodicity, c.) toroidal geometry, Ha = 894, N = 5 periodicity, d.) toroidal geometry, Ha = 894, N = 1 periodicity. Note the difference in y-axis scales. Dotted black lines indicate the time points NIMROD is evaluated at for average mode amplitudes.

5.2.1. NIMROD to MST conversions

To compare NIMROD and MST results, several conversions must be made to compare measurements. The first is converting between the standard coordinate systems used between the two. The NIMROD ϕ and θ directions are flipped relative to the typical MST right-handed coordinate system. The simulation results will be reported in the MST right-handed system. The profiles that are reported with respect to toroidal angle use the same toroidal angle with respect to the helical equilibrium as was used for the experimental data, where $\phi_{hel} = 0$ is chosen to be where the magnetic axis is in line with the DNB line-of-sight on the outboard side.

These simulations were run with a positive λ profile, whereas MST operates with a negative λ profile. The sign of the λ relates to the sign of the q profile, which in turn determines the helicity of the unstable tearing modes that develop. Equal but opposite λ profiles will have equal but opposite tearing modes helicities: $(1, n)$ vs $(1, -n)$. This in turn affects the helicity of the velocity profiles, which will be apparent in figures in Section 5.3. Figure 5.3 compares the two coordinate systems, and the sign of λ is apparent from the orientation of J_ϕ and B_ϕ relative to each other in the two systems, where $\lambda \propto \boldsymbol{J} \cdot \boldsymbol{B}/B^2$.

Lastly, simulations advance non-dimensionalized MHD equations, and so the velocity reported by the simulation is in normalized units, with $V_A = 1$. Since the simulation is run at a different Lundquist number than the experiment, the velocity cannot technically be scaled to the machine parameters exactly by multiplying by the experimentally relevant Alfvén speed. This would cause a mismatch in the resistive diffusion time, which scales with the Lundquist number $\tau_r/\tau_A = S$. The resistive diffusion time will affect the overall velocity profiles, and therefore a compromise scaling formula related to the hybrid relaxation time is

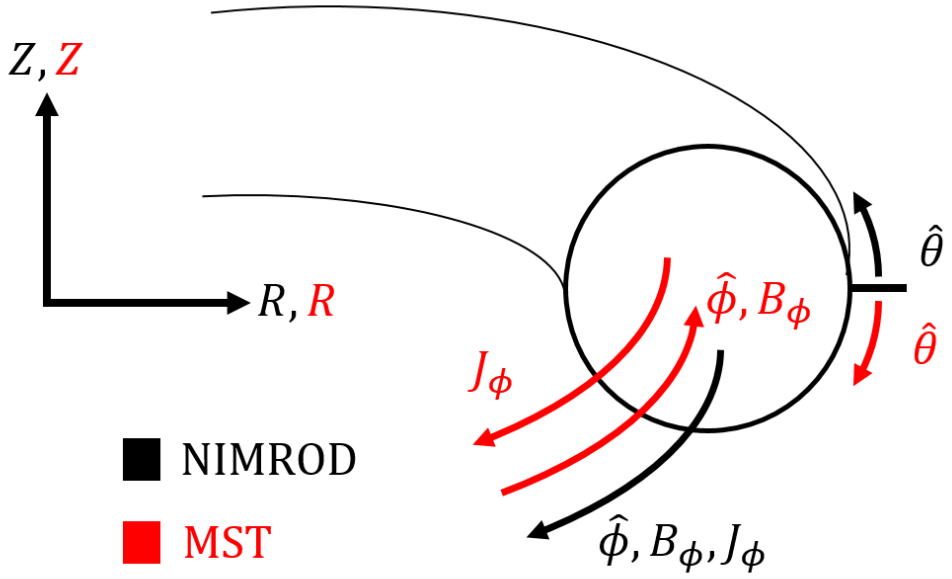

Figure 5.3.: Coordinate systems used in MST and NIMROD. NIMROD results are reported in MST coordinate system.

used to take this into account:

$$V_{scaled} = V_{NIM} * V_{A,MST} \sqrt{\frac{S_{NIM}}{S_{MST}}} \tag{5.7}$$

where V_{NIM} is the normalized velocity reported in NIMROD, $V_{A,MST} \approx 10^6$m/s is the characteristic Alfvén velocity in MST, S_{NIM} is the NIMROD Lundquist number, and $S_{MST} = 10^6$ is the characteristic MST Lundquist number in 500 kA QSH plasmas. Velocities from NIMROD simulations will be reported as V_{scaled} in Equation 5.7 with units of km/s.

5.2.2. Identification of Axes

Flux surfaces on which to parameterize plasma quantities are not easily identifiable in the NIMROD output data. To the extent that a helical magnetic axis forms, it is not inherent

to the problem set-up, as it is in a V3FIT reconstruction, and therefore identifying the axis is nontrivial. Knowing the location of the helical magnetic axis is important for comparing simulation results to experiment. The helical magnetic axis appears to correspond closely to a peak in the pressure profile for the very small beta simulations. The region of maximum pressure also corresponds to the region of healed flux surfaces and the null point in the $n = 5$ magnetic field in the R, Z plane, shown in the rightmost plot of Figure 5.4. This is strong enough evidence to call the location of maximum pressure the location of the helical magnetic axis, and it is pressure that is used to identify the helical axis in all NIMROD simulation analysis.

It is interesting to note that in the region of the helical axis, the velocity is consistently very small, shown in Figure 5.4 d.), where contours are the toroidal velocity and the arrows show the velocity in the R, Z plane.

In Figure 5.5, showing the pressure contours in a cut through the simulation that mirrors the plane sampled as the helical equilibrium rotates through the DNB line-of-sight in the experiment, an inboard and outboard peak are observed. The helical axis points are marked by the black x's here and in all subsequent figures of this type.

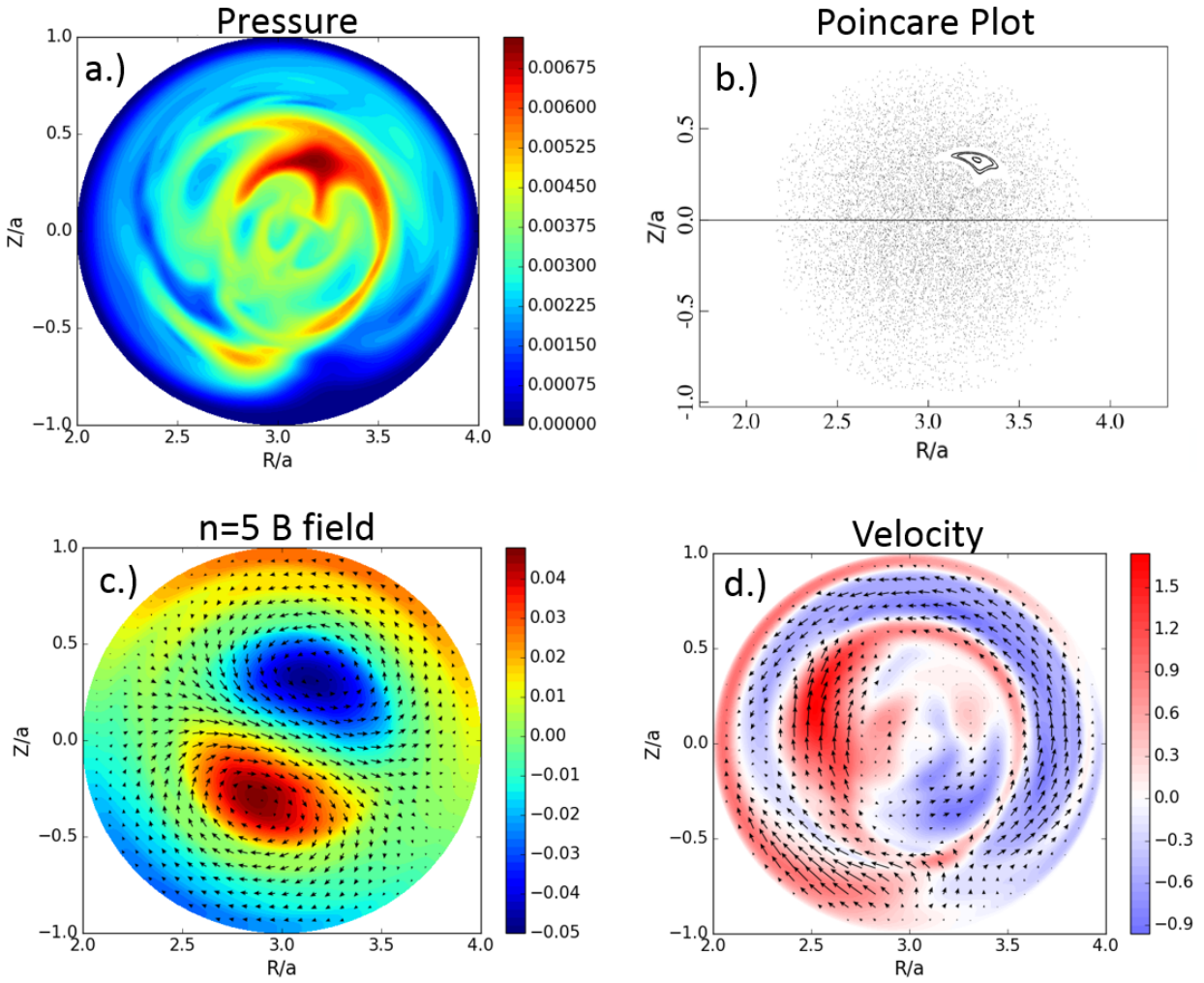

Figure 5.4.: a.) Poloidal cross-section of pressure contours, b.) Poincare plots of magnetic field lines, c.) $n = 5$ magnetic field in-plane (arrows) and toroidal field contours, and d.) the velocity in the poloidal plane (arrows) and toroidal velocity contours for the $N = 5$ periodic, Ha = 8900 NIMROD simulation. The healed flux surface region in the poincare plot matches the region of highest pressure, and the poloidal $n = 5$ magnetic field null.

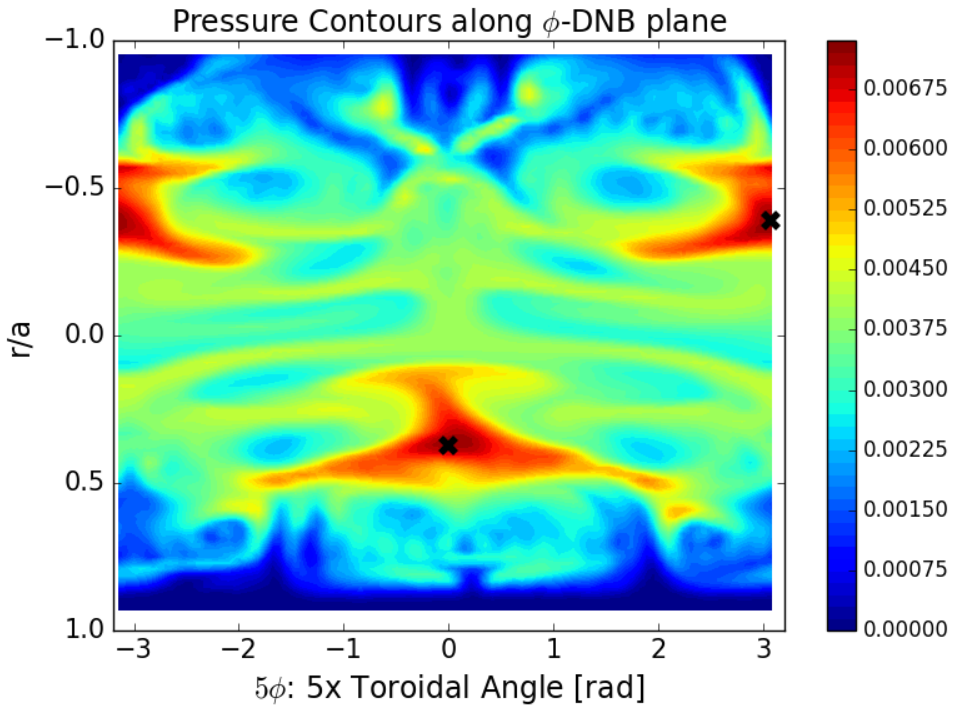

Figure 5.5.: DNB-ϕ cross-section of pressure contours showing the inboard and outboard pressure peaks that correspond to the inboard and outboard helical magnetic axes, marked by x's.

5.3. Comparison to Experiment

With the ability to identify the location of the helical magnetic axis, the experimental and simulation velocity profiles can be directly compared. Veloctiy data from NIMROD will be presented as if it were viewed with a synthetic CHERS diagnostic equivalent to the experimental diagnostic. The objective is to evaluate which simulations appear to match features in the experimentally measured global flow profile best.

The comparisons of the out-of-plane velocity and in-plane (toroidal) perturbed velocity are shown in Figure 5.6 and Figure 5.8 respectively. Contour plots of the experimental data generated from their parameterized profiles are shown in part a.) of the Figures for reference. The representative flux surfaces have been removed and replaced with a black x marking the magnetic axis from VMEC simulations for easier comparison to NIMROD, since flux surfaces weren't calculated for the NIMROD simulations. The mode amplitudes that would be measured at the CHERS measurement locations used in the experiment are shown in Figure 5.7 and Figure 5.9.

The dominant perturbed out-of-plane flow in each NIMROD simulation shown in Figure 5.6 is negative velocity for negative ϕ angles, and positive for positive ϕ angles. This is the opposite of the perturbed flow measured in the experiment, and is attributed to the different signs of the λ profiles in the experiment and simulation mentioned in Section 5.2.1.

The toroidal velocity profiles are more difficult to compare to the experiment given the reduced range of toroidal velocity measurements in the experiment. The $n = 5$ velocity is stronger relative to the other modes than the out-of-plane velocity. From Figure 5.8, it can be seen that the NIMROD simulations all have little to no velocity at $\phi = 0$; this is not true of the toroidal velocity in the experimental measurements, indicating a strong phase shift from the single-fluid simulations.

As seen in Figure 5.7 and Figure 5.9, generally, all cases show strong $n = 10$ and $n = 15$ modes in the mid-radius of the plasma, similar to experiment. No simulation has peaked $n = 15$ modes similar to what is seen in the experiment, however. Each simulation also shows a general alignment of the velocity structures with the magnetic axis, indicative of reconnection-like flows where the out-of-plane and toroidal flows are $\pi/2$ phase shifted from the magnetic axis (reconnection O-point). The following sub-sections will provide commentary on effects observed on the velocity profile from toroidicity, dissipation level, limited periodicity boundary condition, and possible two fluid effects in reference to the figures presented here.

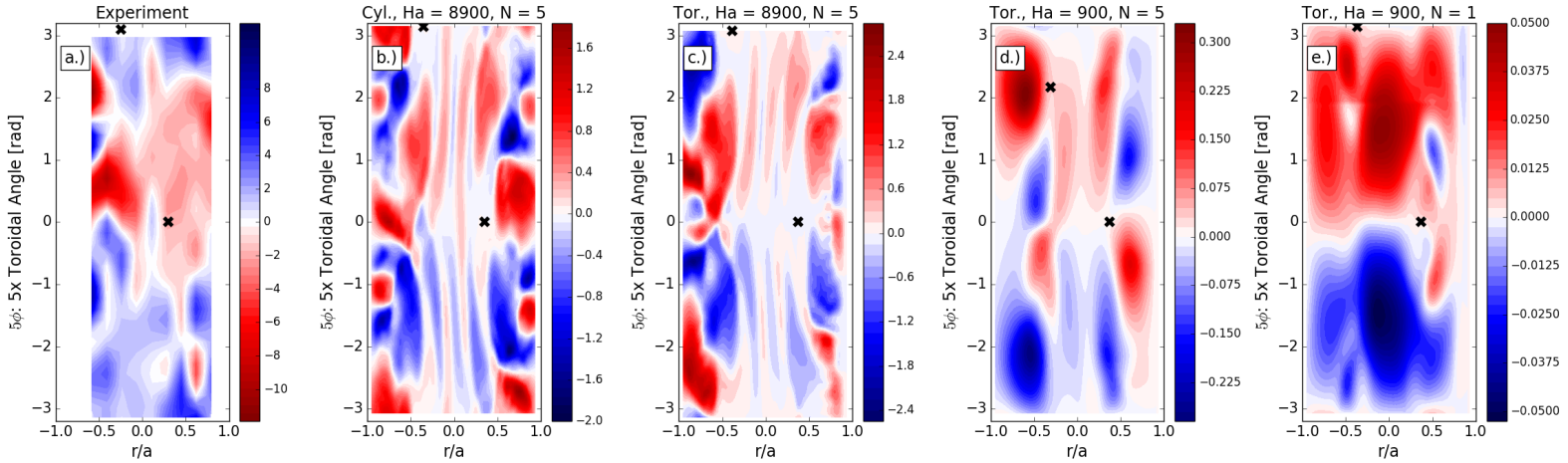

Figure 5.6.: Comparison of out-of-plane velocity between experiment and NIMROD in the ϕ-DNB plane. a.) experimental data is compared against b.) Ha = 8900, $N = 5$ periodic, cylindrical geometry, c.) Ha = 8900 $N = 5$ periodic, toroidal geometry, d.) Ha = 894, $N = 5$ periodic, toroidal geometry, e.) Ha = 894, $N = 1$ periodic toroidal geometry simulations. NIMROD data is taken from the last time point indicated by the dotted black line in Figure 5.1. The reversed color bar axis in Figure a.) is to account for the opposite helicity flows between experiment and simulations

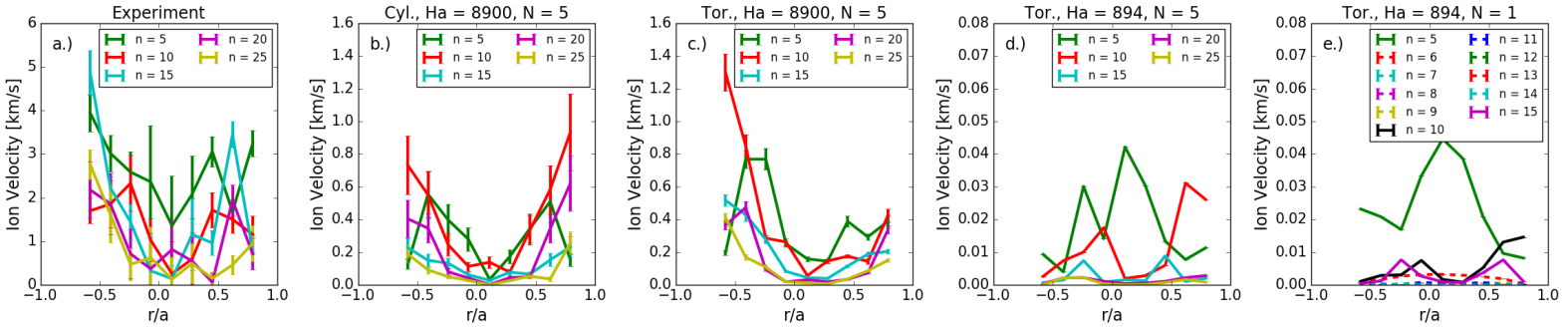

Figure 5.7.: Comparison of out-of-plane velocity mode amplitudes between experiment and NIMROD synthetic CHERS diagnostic. a.) experimental data is compared against b.) Ha = 8900, $N = 5$ periodic, cylindrical geometry, c.) Ha = 8900 $N = 5$ periodic, toroidal geometry, d.) Ha = 894, $N = 5$ periodic, toroidal geometry, e.) Ha = 894, $N = 1$ periodic toroidal geometry simulations.

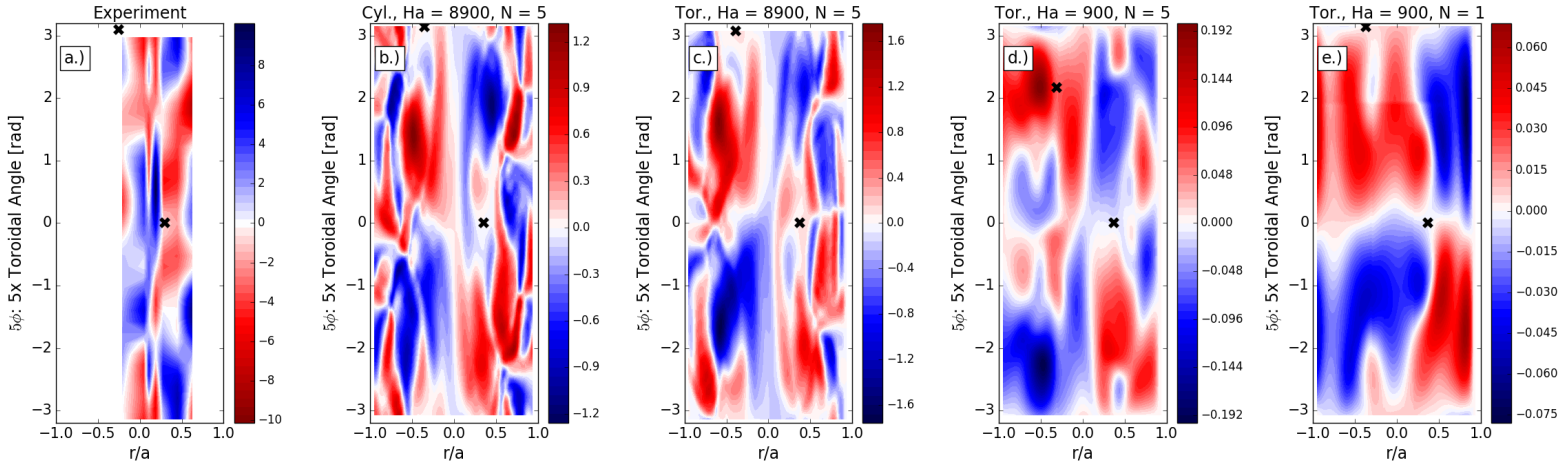

Figure 5.8.: Comparison of toroidal velocity between experiment and NIMROD in the ϕ-DNB plane. a.) Experimental data is compared against b.) Ha = 8900, $N = 5$ periodic, cylindrical geometry, c.) Ha = 8900 $N = 5$ periodic, toroidal geometry, d.) Ha = 894, $N = 5$ periodic, toroidal geometry, e.) Ha = 894, $N = 1$ periodic toroidal geometry simulations. NIMROD data is taken from the last time point indicated by the dotted black line in Figure 5.1 The reversed color bar axis in Figure a.) is to account for the opposite helicity flows between experiment and simulations

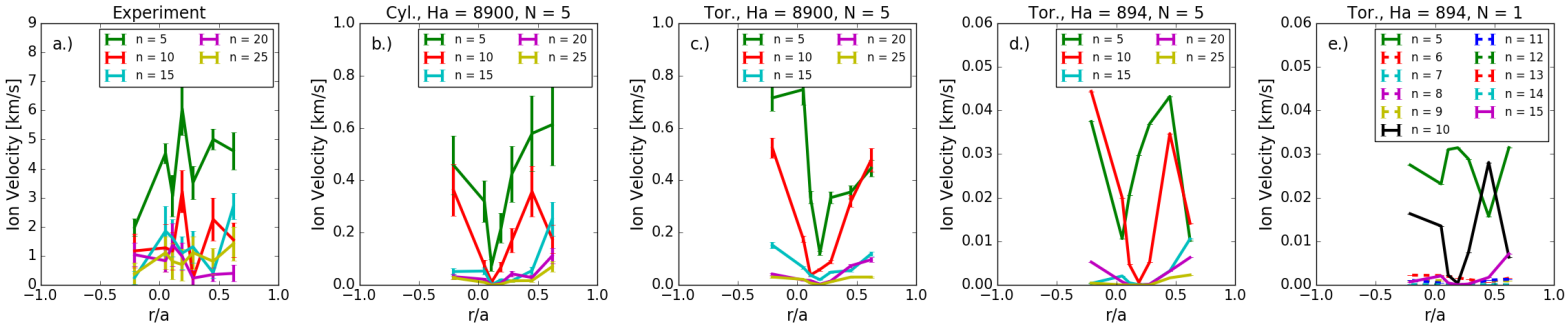

Figure 5.9.: Comparison of toroidal velocity mode amplitudes between experiment and NIMROD synthetic CHERS diagnostic. a.) Experimental data is compared against b.) Ha = 8900, $N = 5$ periodic, cylindrical geometry, c.) Ha = 8900 $N = 5$ periodic, toroidal geometry, d.) Ha = 894, $N = 5$ periodic, toroidal geometry, e.) Ha = 894, $N = 1$ periodic toroidal geometry simulations.

5.3.1. Effects of Viscosity

It is typically accepted that the relevant viscosity of the plasma scales inversely with plasma current, as discussed in Section 2.2.1, thus the increasing prevalence of QSH as plasma current increases challenges the notion that large viscosity is the key mechanism in QSH formation.

Comparing high and low Ha simulations Figures 5.6 and 5.8, the limited periodicity, high Ha number has a more complicated flow structure, with $n > 5$ mode amplitudes more comparable to the $n = 5$ mode amplitude than the low Ha simulations in both the out-of-plane and toroidal velocity profiles. Unsurprisingly, the higher viscosity of the low Ha simulations have significantly lower total velocity amplitude.

Both high Ha simulations have a hollow flow profile, whereas the high dissipation simulations have strong $n = 5$ flow in the core early on. The tendency of low Ha simulations to have strong flow in the core appears to be consistent with other high viscosity SH simulations such as the SpeCyl simulation reproduced in Figure 2.5, where the black arrows represent flow in the plane of the poloidal cross-section shown. Interestingly, as the low Ha simulations evolve in time, the $n = 5$ out-of-plane velocity profile eventually becomes hollow, shown in Figure 5.10 and Figure 5.11. The time periods where the velocity becomes hollow for these high dissipation runs is more dynamic, and the early flattop regions of the plots are considered more comparable to the saturate SHAx state seen in experiment. Given the consistency of the hollow profile in high Ha simulations, and the greater overall structure in the flow profiles, the high Ha limited periodicity simulations are considered more representative of the experimental data than the low Ha simulations.

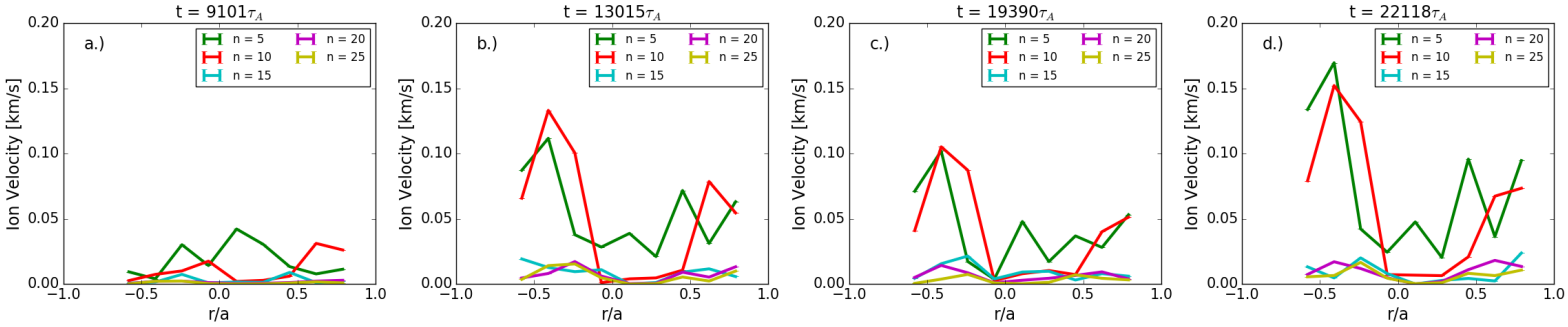

Figure 5.10.: Toroidal, Ha = 894, $N = 5$, Out-of-Plane velocity for a.) $9101\tau_A$, b.) $13015\tau_A$, c.) $19390\tau_A$, d.) $22118\tau_A$ times. Over time, when dithering between the $n = 5$ and $n = 10$ starts to occur, the mode profile changes from peaked to hollow.

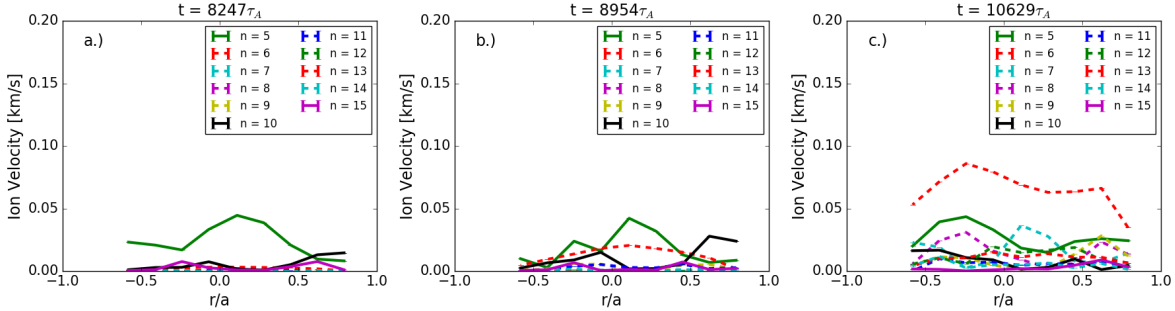

Figure 5.11.: Toroidal, Ha = 894, $N = 1$, out-of-plane velocity for a.) $8247\tau_A$, b.) $8954\tau_A$, and c.) $10629\tau_A$. The mode profile changes from peaked to hollow as the $n = 5$ QSH mode dies off.

5.3.2. Effects of Limited Periodicity Boundary Condition

While not a physical effect that can appear in experimental measurements, the limited periodicity boundary condition does influence the simulation results. When the boundary condition is lifted, the relative amplitude of the $n > 5$ velocity modes drop, as shown in e.) compared to d.) of Figures 5.7 and 5.9. It is expected that the amplitudes of the sub-dominant modes relative to the $n = 5$ mode amplitude would increase in the limited periodicity case, since there are fewer modes to couple away energy from the $n = 5$ mode. This helps explain why the $n = 10$ mode observed in the limited periodicity cases is stronger than what is observed in the experiment. Interestingly, the $n = 10$ and $n = 15$ mode profiles are larger than the $n = 6$ in the $N = 1$ periodic simulation.

While the $n = 5$ magnetic energy dominates $n > 5$ modes for all simulation times under consideration, the $n = 10$ kinetic energy is dominant or comparable to the $n = 5$ kinetic energy in each limited periodicity case. This is again likely the result of the truncation of allowed toroidal modes caused by the limited periodicity boundary condition. Nonlinear energy transfer that would normally be spread out over n = 6,7,8 etc. modes if the full domain of the torus were modeled is forced into the fewer number of modes allowed in the simulation.

Overall, the comparison between the $N = 1$ and $N = 5$ periodicity simulations is challenged by the fact that, in the $N = 1$ simulation, the $n = 5$ QSH state is short lived in time, and eventually the simulation yields an $n = 6$ QSH state, and then a long lived dominantly $n = 7$ QSH state. This behavior has not been observed in experiments.

5.3.3. Effects of Toroidicity

The effects of toroidal geometry are important in understanding the full poloidal and toroidal spectrum for non-axisymmetric modes. The geometry of a torus naturally introduces a $(m, n) = (1, 0)$ perturbation to profiles. The effects of toroidal geometry on magnetic profiles in standard, reversed RFP plasmas in MST were studied in detail using NIMROD simulations by Josh Sauppe[2]. Geometric coupling due to toroidicity allows coupling to the $m \neq 1$ modes from the $m = 1$ tearing mode, and causes phase shifts in the eigenmode profiles relative to cylindrical profiles, as shown in Figure 5.12 (b) and (a) respectively. Due to the lack of poloidal resolution in the the CHERS velocity measurements, the poloidal m modes cannot be distinguished, and the toroidal n mode's amplitude and phase are a summation of the entire poloidal mode spectrum:

$$V_n \cos(n\phi + \Delta_n) = \sum_m V_{n,m} \cos(m\theta + n\phi + \Delta_{m,n}). \tag{5.8}$$

Given the consistency of the phase of the $n = 5$ out-of-plane velocity across the plasma radius, it is likely that $n = 5$ velocity is dominated by a single global flow structure with an odd poloidal mode.

The impact of toroidal effect can be complex, but a simple analysis can provide insight into the flow asymmetry. A device without toroidal effects is expected to have poloidally symmetric profiles where the origin is defined as the axis of rotation of the helical equilibrium. Since the CHERS out-of-plane flow measurements are spaced at equidistant intervals from the axis of rotation, the ratio of a simple summation of the inboard and outboard flow measurements should be about unity for a poloidally symmetric profile without toroidal asymmetry. These ratios can be done for each toroidal mode of the parameterized profiles of the experimental velocity data, and compared to toroidal and cylindrical simulations. The

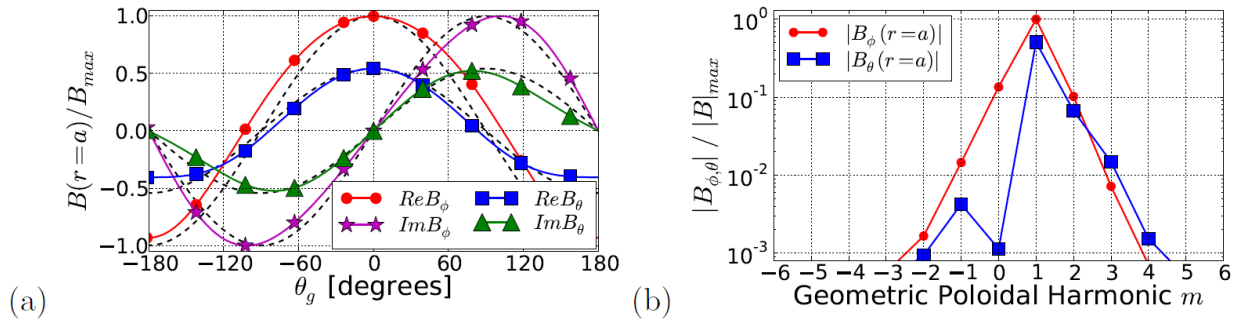

Figure 5.12.: Example of magnetic perturbations for the dominant tearing mode at r = a. (a) The eigenmode in configuration space in toroidal and cylindrical (dashed black lines) geometry. (b) Fourier decomposition of the eigenmode with respect to geometric poloidal angle. Figure is reproduced from Sauppe's thesis[2] Figure 8.11.

velocity ratio, $VR_{IN/OUT}$, for each mode is defined as:

$$VR_{IN/OUT} = \frac{\sum_{R_{IN}=[R_{CHERS,inboard}]} V_n(R_{IN})}{\sum_{R_{OUT}=[R_{CHERS,outboard}]} V_n(R_{OUT})} \tag{5.9}$$

where $[R_{CHERS,inboard}]$ is the set of inboard CHERS locations, $[R_{CHERS,outboard}]$ is the set of outboard CHERS locations, and V_n is the n toroidal mode velocity. Inboard and outboard are defined relative to the axis of rotation of the helical equilibrium, as described in Figure 3.4. The ratio is shown for $n = 0-25$ in Figure 5.13. While the experimental axisymmetric, $n = 0$, flow is highly asymmetric, the $n = 5$ mode has weaker asymmetry, within the uncertainty range of the cylindrical NIMROD simulation. The toroidal NIMROD velocity ratio is larger than the experimental ratio.

A simple expectation is the enhancement of measured flow on the inboard side relative to the outboard, assuming incompressible flow, since the total cross-sectional area on the inboard side is less than the outboard. The ratio of the cross-sectional areas between the inboard and outboard sides of the torus measured from a Shafranov-shifted axisymmetric

axis is only 0.7, so, for a flat density profile, the relationship between the net inboard and outboard velocity should be: $V_{IN} = 1.4V_{OUT}$. This simple geometrical factor would account for the asymmetry in most of the non-axisymmetric flow. Interestingly, the experimental axisymmetric flow appears to be enhanced beyond this ratio, possibly indicating stronger flow drive on the inboard side. The results suggest that for the dominant $n = 5$ mode, toroidal geometry is not necessary to capture the the $n = 5$ flow profile features seen in the out-of-plane flow. This could be verified with measurements on RFPs with lower and high aspect ratios than MST, such as RELAX and RFX.

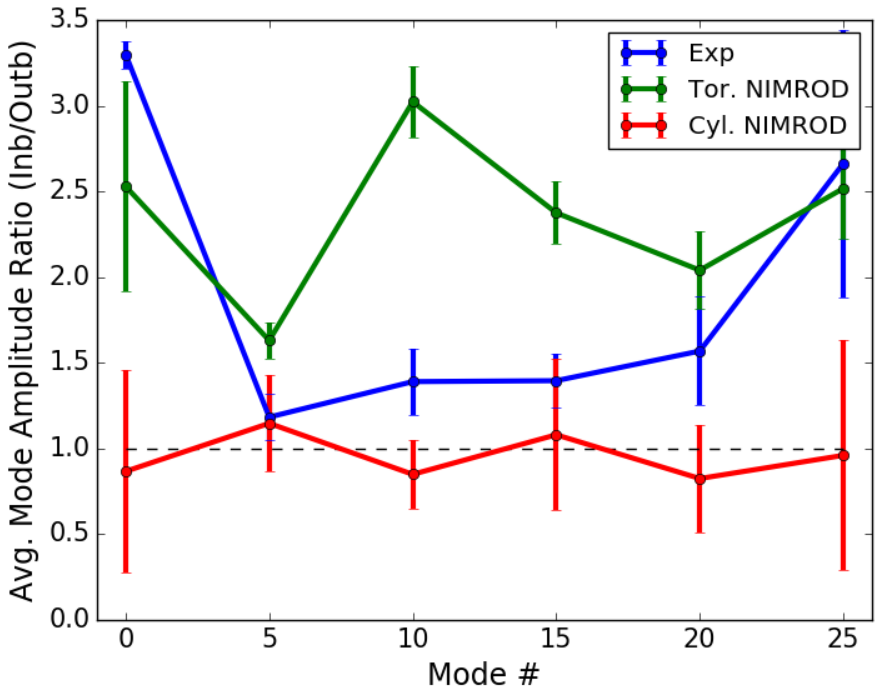

Figure 5.13.: Ratio of the inboard/outboard asymmetry of the out-of-plane flow per mode for the experiment and toroidal, Ha = 8900, N = 5 periodicity NIMROD simulation. The cylindrical Ha = 8900, N = 5 simulation is included as a baseline. The simulation error bars come from averaging velocity profiles at multiple time points in the simulations.

5.3.4. Possible Two-fluid Effects

Each simulation discussed was run using single-fluid MHD. However, it is likely that the MST SHAx state is in the two-fluid regime. The ion skin depth in MST's core is 14 cm, giving $d_i/a = 0.27$, a significant fraction of the minor radius. Most of the CHERS measurements are separated by 9 cm, well inside the ion skin depth. Work from J. King [3, 5] indicates that the effect of warm ions in MST's core in a single-helicity state is to shift the global flow profile relative to the magnetic reconnection system that is creating it. This is attributed to the ion-gyrovisous force, and persists after the tearing mode has saturated. The electron-fluid stays well-aligned with the magnetic perturbation to support reconnection-like flows, and is generally unaffected by whether the ions are warm or cold. The difference between warm and cold ion flow profiles is highlighted in Figure 5.14, where a single helicity tearing mode (blue) is plotted in helical coordinates against the ion flow profiles (red). The magnitude of the flows in the warm-ion ion case are also significantly larger than the cold-ion case.

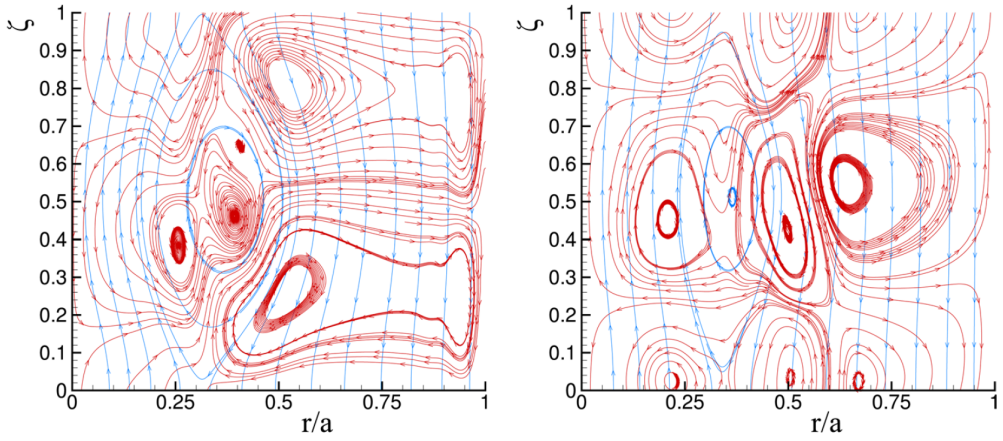

Figure 5.14.: A projection of the tearing mode structures onto a representative helical surface from single-island cold-ion modeling (left) and warm-ion modeling (right). The magnetic field is shown in blue with a single island at $r_s = 0.35a$ and the ion flow is shown in red. Figure taken from King, 2012[3]

The phase of the $n = 5$ flow in both the out-of-plane and toroidal direction in the

single-fluid, Ha = 8900, toroidal simulation is compared to the experimental $n = 5$ flow phase in Figure 5.15. Along the ϕ-DNB plane available to the diagnostic, a phase shift of about half a radian in the out-of-plane velocity from the expected phase of $\pi/2$ from the magnetic axis is observed over much of the plasma. By comparison, the single-fluid toroidal $N = 5$, Ha = 8900 simulation plotted in blue shows little shift from the expected $\pi/2$ phase from the magnetic axis.

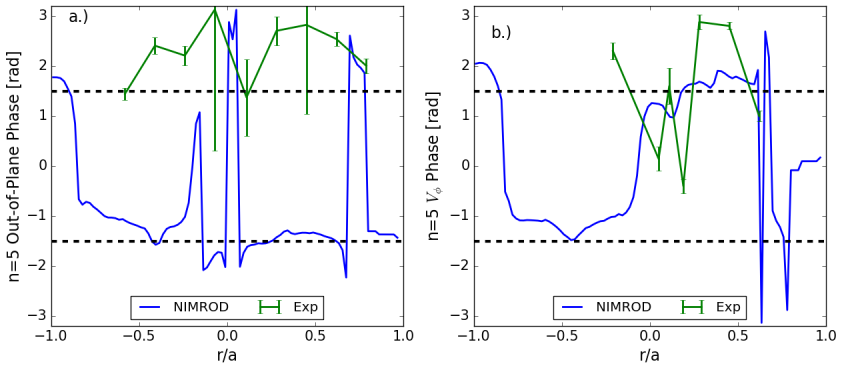

Figure 5.15.: Comparison of experimental and simulated Ha = 8900, N=5 periodic toroidal phases for the $n = 5$ out-of-plane (left) and toroidal (right) flow.

The same process can be performed for the toroidal flow data. The phase shift for this data is different than the poloidal data at the same location. The $n = 5$ velocity phase profile for the toroidal velocity is more complicated than the $n = 5$ poloidal velocity phase profile, showing more changes in phase versus radius.

A phase shift from reconnection-like flows relative to the global non-axisymmetric magnetic profile is suggestive of a decoupling of the ion and electron flow profiles. Care should be taken in interpreting these results. As mentioned in Section 5.3.3, toroidicity causes mode coupling that gives rise to $m \neq 1$ modes. The toroidal simulation is subject to the same geometric coupling, and shows little phase shift from the expected reconnection-like flows, however, so it is expected the influence of $m \neq 1$ modes on the $n = 5$ phase is small. Sepa-

rately, since there is technically no longer an x-point in SHAx, it is possible that the electron fluid has changed from a flow profile that supports reconnection, and the experiment, being a stronger SHAx state than the simulation, is more influenced by the change. While J. King's single-helicity two-fluid simulation work gives us excellent insight into possible effects of warm ions on the ion flow profile, the saturate state is a helical island, not SHAx, and future two-fluid, toroidal QSH simulations that achieve a SHAx state would improve the ability to interpret experimental data.

5.4. Summary

The experimental QSH measurements have been compared to four NIMROD simulations with different geometry, viscous dissipation, and periodic boundary conditions to help understand what the impact of toroidicity and viscosity has on the flow, as well as the effect the periodic boundary condition has on the simulation results. High Hartmann number (Ha = 8900) simulations resulted in a hollow radial profile of out-of-plane flow, similar to what is observed in experiment, and inconsistent with previously peaked radial profiles reported in low Hartmann number QSH simulations in literature, and the initial QSH flattop of low Hartmann (Ha = 894) number NIMROD simulations. The toroidal geometry causes an inboard/outboard flow asymmetry in the out-of-plane flow in simulations, similar to what is seen in axisymmetric out-of-plane flow in the experiment, but greater than what is observed in experiment for the non-axisymmetric out-of-plane flow, including the dominant $n = 5$ out-of-plane flow. The effect of the periodic boundary condition is to increase the amplitude of the sub-dominant modes. Lastly, two-fluid effects are potentially responsible for the phase shifts observe in the $n = 5$ out-of-plane and toroidal flow from reconnection like flows in the experiment, where single-fluid toroidal NIMROD simulations did not have such phase shifts.

References

[1] C. R. Sovinec, A. H. Glasser, T. A. Gianakon, D. C. Barnes, R. A. Nebel, S. E. Kruger, D. D. Schnack, S. J. Plimpton, A. Tarditi, and M. S. Chu, "Nonlinear magnetohydrodynamics simulation using high-order finite elements," *Journal of Computational Physics*, vol. 195, pp. 355–386, 3 2004.

[2] J. Sauppe, *Extended Magnetohydrodynamic Modeling of Plasma Relaxation Dynamics in the Reversed Field Pinch*. PhD thesis, University of Wisconsin - Madison, 2015.

[3] J. King, *First-order finite-Larmor-radius effects on magnetic tearing and relaxation in pinch configurations*. PhD thesis, University of Wisconsin - Madison, 2011.

[4] S. Cappello, D. Bonfiglio, and D. F. Escande, "Magnetohydrodynamic dynamo in reversed field pinch plasmas: Electrostatic drift nature of the dynamo velocity field," *Physics of Plasmas*, vol. 13, no. 5, p. 056102, 2006.

[5] J. R. King, C. R. Sovinec, and V. V. Mirnov, "First-order finite-Larmor-radius fluid modeling of tearing and relaxation in a plasma pinch," *Physics of Plasmas*, vol. 19, no. 5, p. 055905, 2012.

6. Shear Characterization of SHAx state

Velocity shear has the potential to cut off non-linear energy transfer between tearing modes, reducing the strength of sub-dominant modes, and increasing the strength of the dominant mode. This makes the shear profile in the SHAx state a measure of great interest for understanding possible mechanisms for achieving a SHAx equilibrium. This chapter will characterize the shear in the machine, calculated from the available velocity measurements in the saturated SHAx state. First, shear in the poloidal and toroidal plane is presented, and then the velocity is projected into a helical coordinate system at radial locations with overlapping toroidal and out-of-plane velocity measurements. Motivated by the work done on a shear suppression model for obtaining QSH[1, 2, 3] and described in Section 2.2.3, the shear in the helical angular velocity is calculated, and the critical shear for the suppression of non-linear coupling is discussed.

6.1. Shear in the toroidal and poloidal planes

The shear in the toroidal direction $\Delta V_\phi/\Delta r^*$, and out-of-plane direction, $\Delta V_O/\Delta r^*$, are shown in Figure 6.1 a.) and b.) respectively. The variable r^* is the radius measured from the toroidally-symmetric Shafronov-shifted axis about which the helical magnetic axis

rotates (this was previously the Sharfanov shifted magnetic axis when the plasma was in a multi-helicity state). This is distinguished from r, which is measured from the geometric axis. Note that the data is still plotted according the geometric axis variable, r.

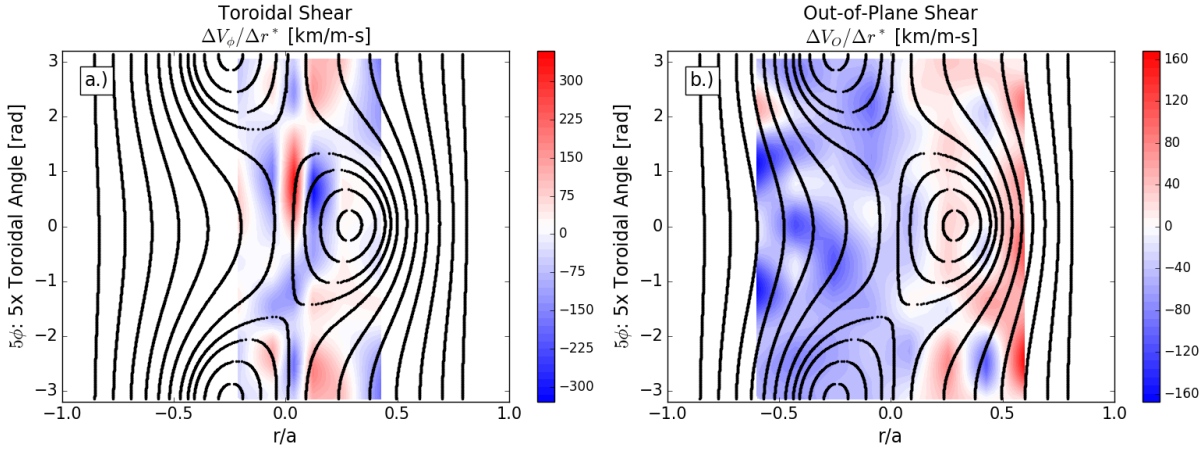

Figure 6.1.: a.) Shear in Toroidal Velocity. b.) Shear in out-of-plane velocity.

The toroidal flow shear is quite strong near the helical axis. This is primarily due to a nearly π phase shift in the $n = 5$ velocity profile between $r/a = 0.19$ and $r/a = 0.28$ that can clearly be seen in the profiles in Figure 4.12. The toroidal flow shear comes mostly from the non-axisymmetric portion of the velocity profile, since the axisymmetric toroidal velocity profile is relatively uniform. The shear in the out-of-plane velocity is dominated by the axisymmetric profile shown in Figure 4.14. The axisymmetric shear is nearly uniform on the inboard side and a portion of the outboard side due to a rigid-rotor like flow, before it turns over and reverses direction in the outboard edge.

6.2. Shear of the helical angular velocity

In context of the shear of the dominant mode required to decouple energy transfer to sub-dominant modes, it is not the total shear that is of interest, but the shear of angular velocity

in the $r - \chi$ plane, where χ is the helical angle matching the dominant mode helicity[1], illustrated in Figure 2.7. As was mentioned in Section 2.2.3, the angular velocity includes contributions from the radial velocity, however, this component was not measured. Only the V_χ component of angular velocity can be computed from the available measurements, shown in red in Figure 6.2. The measured helical angular velocity is only representative of the full angular velocity at $\chi = 0$, the island O-point (or the SHAx magnetic axis). In Figure 6.4 and Figure 6.4 the helical angular velocity is calculated and projected onto the DNB-ϕ plane that is sampled by the CHERS diagnostic. The region where the helical angular velocity is equivalent to the full angular velocity is shown in as a gray band on the figures.

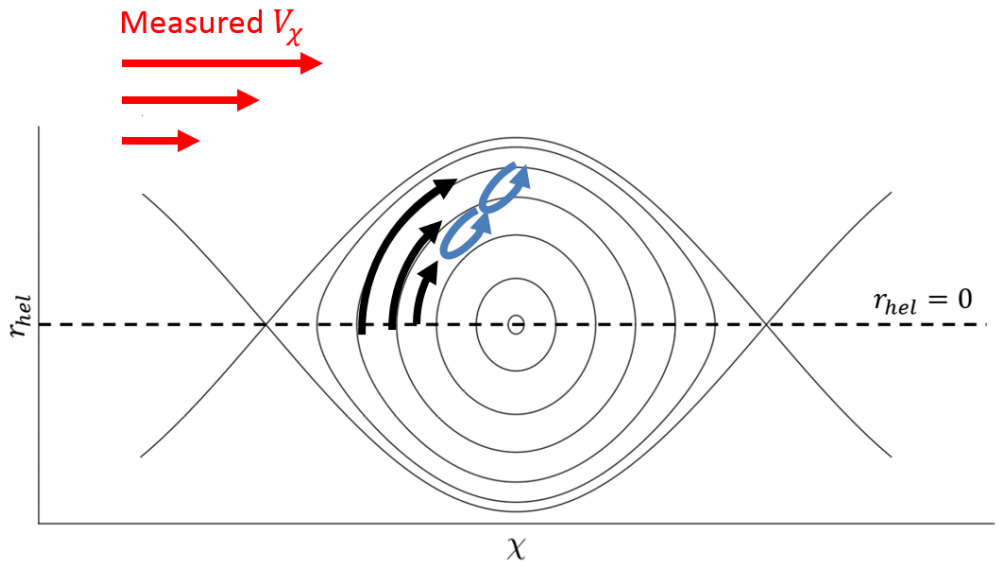

Figure 6.2.: Conceptual illustration of a sub-dominant tearing mode as a sheared "eddy" in the frame of reference the dominant tearing mode island. The helical angle is $\chi = m\theta + n\phi$, with the m and n modes of the dominant tearing mode, and $r_{hel} = r - r_s$, where r_s is the radial location of the dominant tearing mode rational surface. The blue circles represent the sub-dominant eddies, the black arrows are the sheared velocity or magnetic field, and the red arrows indicated the direction of measured velocity.

Helical coordinates are used to calculate the angular velocity. The radial coordinate is $r_{hel} = r^* - r_s$, where r_s is the radius of tearing mode rational surface, which closely translates

to the radius of the helical magnetic axis from the axis of rotation (see Figure 6.3). Both r^* and r_s are measured from the axisymmetric Shafranov shifted magnetic axis.

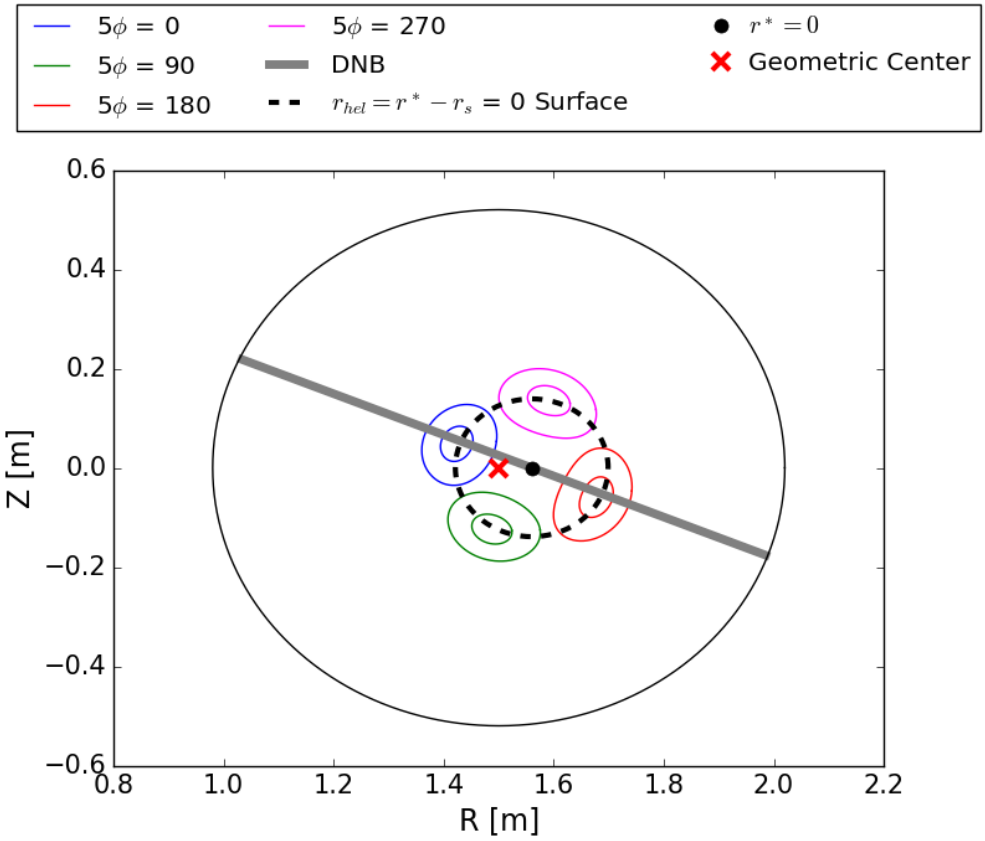

Figure 6.3.: Diagram showing that the helical radius $r_{hel} = 0$ is the surface on which the helical magnetic axis rotates in SHAx plasmas. Four different toroidal locations relative to the DNB are shown.

The angular velocity shear is

$$\Omega'_V = \frac{\partial}{\partial r_{hel}}\left(\frac{V_\chi}{r_{hel}}\right) \tag{6.1}$$

where $V_\chi = V \cdot r\nabla\chi = mV_\theta + \frac{nr}{R_0}V_\phi$.

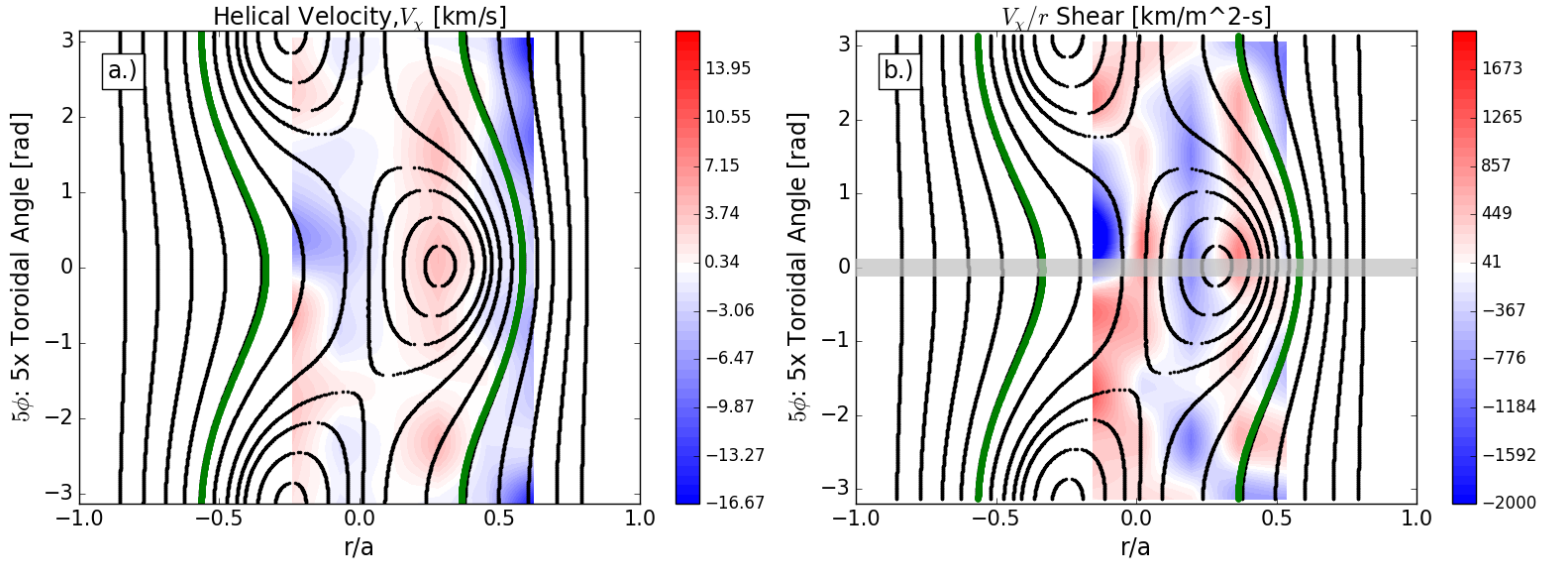

Figure 6.4.: a.) Velocity projected in the helical direction, and b.) helical angular velocity shear measured roughly from the surface of rotation of the helical magnetic axis, r_{hel}. The green lines mark the next sub-dominant mode location on the flux surface puncture plot, and the gray band is the toroidal location where the helical angular shear represents the full angular shear without any contributions from V_r/r_hel.

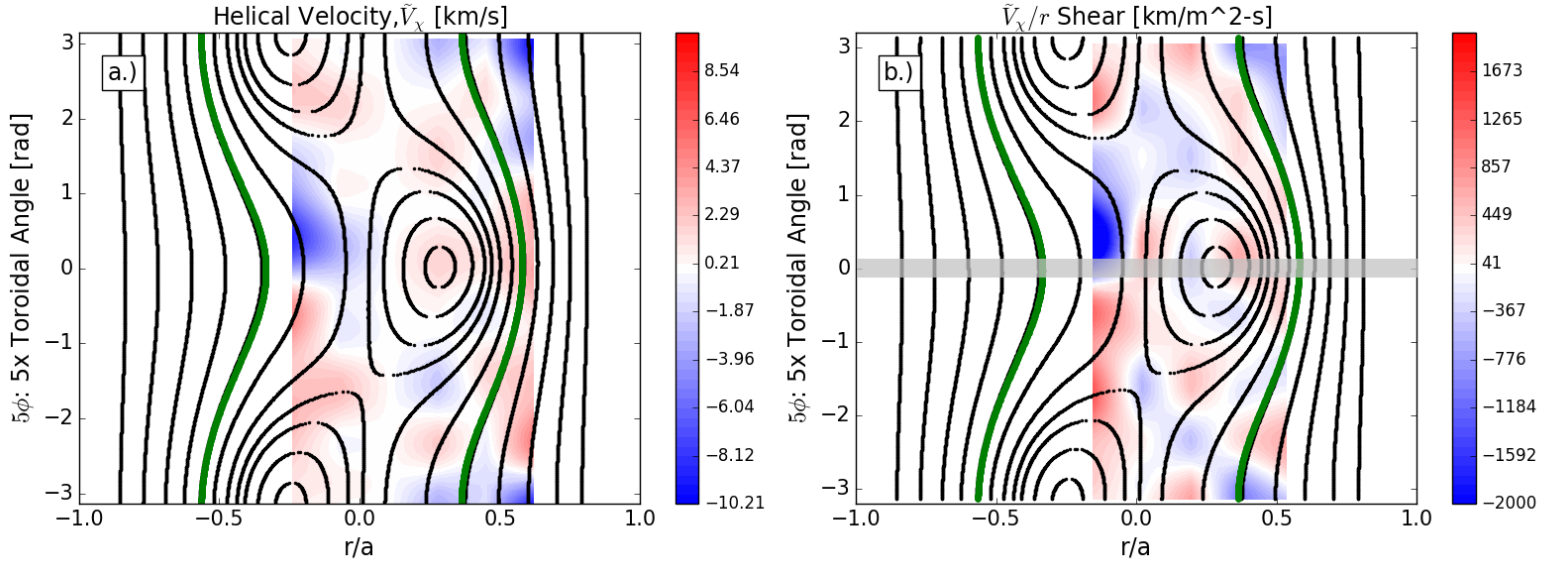

Figure 6.5.: a.) Non-axisymmetric velocity projected in the helical direction, b.) angular non-axisymmetric helical velocity shear measured roughly from the surface of rotation of the helical magnetic axis, r_{hel}. The Green lines mark the next sub-dominant mode location on the flux surface puncture plot, and the gray band is the toroidal location where the helical angular shear represents the full angular shear without any contributions from V_r/r_hel.

The helical velocity and helical angular velocity shear is calculated for both the full velocity profile (Figure 6.4 a.) and b.)) as well as for the purely non-axisymmetric velocity profile (Figure 6.5). This was influenced by the fact that the shear suppression model only considered perturbed components of velocity, but it is expected that the axisymmetric velocity can play a role as well. The helical velocity profile and shear are influenced by the axisymmetric velocity projected into the helical reference frame, but is not completely dominated by it, as can be seen by comparing Figure 6.4 and Figure 6.5. The green line in the figures represents the location of the sub-dominant tearing mode resonant surface nearest the magnetic axis. The region between the magnetic axis and the nearest sub-dominant tearing mode is expected to be most important for establishing a shear boundary layer and disrupting non-linear energy transfer between modes.

Repeating the discussion in Section 2.2.3, the peak angular velocity shear must be on the order of the eddy turnover time of the sub-dominant mode to affect the correlation between tearing modes. This leads to the shear suppression criterion in Equation 2.20. Using the expectation that sub-dominant tearing mode flows before the onset of QSH are on the order of the flows measured by David Ennis in reversed, 400 kA plasmas[4], and that the islands widths are on the order of 5-10 cm[5], the angular shear threshold is on the order of 100's of km/m^{2}s, with a maximum expected shear of 600 km/m^{2}s.

The uncertainty associated with the calculation is too high to make a strong statement about the size of flow shear compared to the critical shear necessary to affect tearing modes. This is especially true in the region between the helical magnetic axis and the adjacent sub-dominant tearing mode rational surface. To illustrate this point more clearly, the cross-section of helical angular shear flow measurements at the helical toroidal angle $5\phi = 0$ is shown in Figure 6.6, where the helical angular velocity is represents the entire angular velocity about the magnetic axis. The uncertainty in the helical angular shear is calculated assuming

a constant 3 km/s uncertainty in the poloidal and toroidal velocity, 1 cm uncertainty in r_*, and 2 cm uncertainty in the location of the rational surface, r_s. Both the uncertainty in the velocity and the location of the radial surfaces contribute about equally to the uncertainty in the helical angular shear. The uncertainty in the helical angular shear is roughly consistent over toroidal angle for a given radial location.

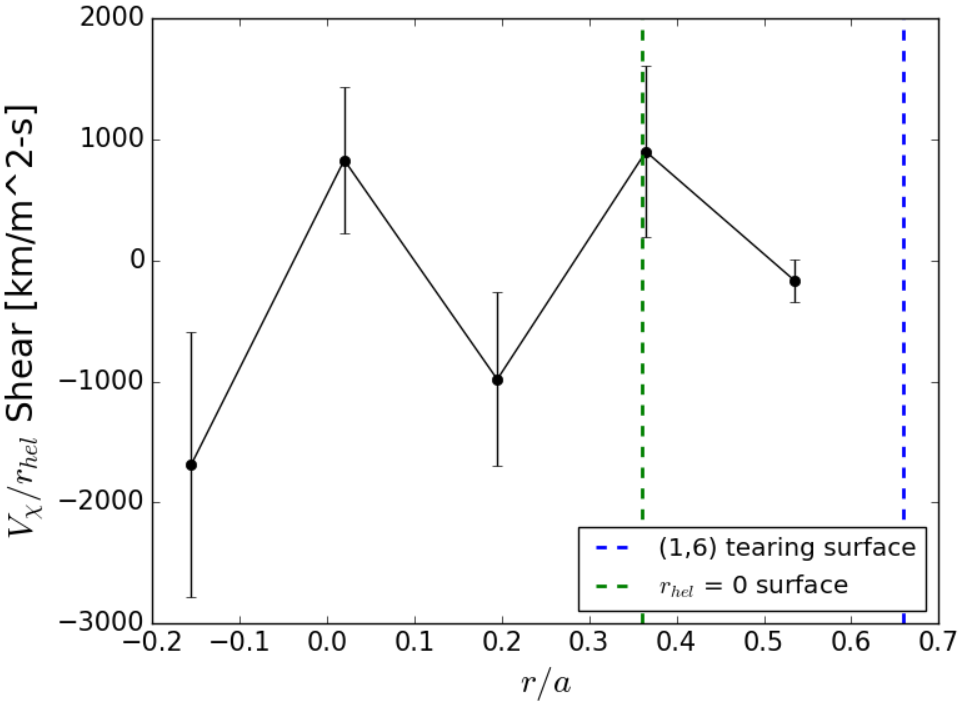

Figure 6.6.: Cross-section of the helical angular shear from Figure 6.4 at $5\phi = 0$. The helical angular velocity shear is on par with the critical shear necessary to affect sub-dominant tearing mode flow.

The calculation presented is an effort to apply a reduced model to a complex, 3D plasma. As such, simplifications are made to make the calculation tenable. Typically the shear flow of interest is in the plane perpendicular to the equilibrium magnetic field. In the SHAx state, with a 3D equilibrium, the perpendicular direction has a radial component which is ignored in the calculation. The helical magnetic also has $n > 5$ variation with the

toroidal angle which is also ignored in the calculation.By ignoring these features, the helical coordinate system considered is no longer associated with the V3FIT magnetic equilibrium calculated, and it is instead used as a rough guide for locating the average location of the helical magnetic axis, which is taken to be a constant. Ideally the both the theory and the data would be evaluated in context of a straight-field line coordinate system. The data is not sampled along straight field lines however, and would have to be mapped to such a coordinate system using a parameterized profile.

6.3. Summary

There is significant flow shear in the saturated SHAx state. Toroidal flow shear is strongest in the geometric core of the plasma, where $n = 5$ flows are counter propagating, and the out-of-plane shear is stronger outside the core. A method for estimating the helical angular shear is presented, and the shear is found to be comparable to the critical shear estimated based on the scale of the flow associated with the sub-dominant tearing mode flows over the typical sub-dominant island width. However, the uncertainty in the calculation is too large to make a conclusion on the possible role of shear in suppression non-linear energy transfer between tearing modes, especially in the region between the helical magnetic axis and the sub-dominant tearing mode rational surface. Improvements in the measurement of both velocity, and the location of the helical magnetic axis are necessary to better resolve the calculated helical angular shear flow.

References

[1] J. H. Kim and P. W. Terry, "Magnetic turbulence suppression by a helical mode in a cylindrical geometry," *Physics of Plasmas*, vol. 19, no. 12, p. 122304, 2012.

[2] P. W. Terry and G. G. Whelan, "Time-dependent behavior in a transport-barrier model for the quasi-single helcity state," *Plasma Physics and Controlled Fusion*, vol. 56, no. 9, p. 094002, 2014.

[3] I. J. McKinney and P. W. Terry, "Thermal transport dynamics in the quasi-single helicity state," *Physics of Plasmas*, vol. 24, no. 6, p. 062303, 2017.

[4] D. A. Ennis, D. Craig, S. Gangadhara, J. K. Anderson, D. J. Den Hartog, F. Ebrahimi, G. Fiksel, and S. C. Prager, "Local measurements of tearing mode flows and the magnetohydrodynamic dynamo in the Madison Symmetric Torus reversed-field pinch," *Physics of Plasmas*, vol. 17, no. 8, p. 082102, 2010.

[5] T. M. Biewer, C. B. Forest, J. K. Anderson, G. Fiksel, B. Hudson, S. C. Prager, J. S. Sarff, J. C. Wright, D. L. Brower, W. X. Ding, and S. D. Terry, "Electron Heat Transport Measured in a Stochastic Magnetic Field," *Physical Review Letters*, vol. 91, p. 045004, 7 2003.

7. Conclusions and Future Work

7.1. Conclusions

For the first time, toroidally resolved plasma flow velocity in the toroidal and poloidal plane are measured in the saturated SHAx state of a reversed field pinch plasma. The measurements implement a novel absolute wavelength calibration technique for spatially localized CHERS spectroscopic measurements, as well as a new method for phase locking control of the helical equilibrium with an RMP.

The axisymmetric toroidal flow has a flat radial profile with magnitude on the order of 10 km/s. The axisymmetric flow in the poloidal plane is rigid-rotor-like on the inboard side, but at the outboard side it turns over at the mid-radius and reverses sign at the edge. Similar axisymmetric flows are observed in improved confinement, reduced tearing (PPCD) plasmas, indicating the axisymmetric flow profile measured in the poloidal plane is not unique to the SHAx state.

A parameterized model is used to decompose the velocity profiles into Fourier harmonics of the $n = 5$ magnetic mode phase measured at the wall, a parameter representative of the toroidal location of the helical equilibrium. The amplitudes of the harmonics show that the radial profile is hollow, and the velocity is dominantly $n = 5$ for $r/a < 0.5$. However, the

flow in the poloidal plane has localized peaks at $r/a = -0.58$ and $r/a = 0.62$ indicative of $n > 5$ structure. The toroidal profile of the flow in the poloidal plane at these two radii is similar, with two well resolved peaks in the toroidal profile and an extended flat region.

Single fluid initial value extended-MHD NIMROD simulations run at high and low dissipation (low and high Hartmann number respectively), in both cylindrical and toroidal geometry using an $N = 5$ periodic boundary condition to achieve QSH provide insights as to what physical effects are influential in the observed flow profiles. The flow in the poloidal plane of low dissipation simulations has a hollow profile, similar to experimental observations. This is opposite what is observed in SpeCyl simulations that use high-dissipation to force a SH state, which have radial profiles that are peaked in the core. Similar peaked profiles are seen in the initial QSH flat-top of high-dissipation NIMROD simulations, with the caveat that the high-dissipation simulations did not reach a steady-state. The inboard/outboard asymmetry of the flow in the poloidal plane in the toroidal simulations is stronger than observed in experiment, with the exception of the axisymmetric flow, which was strongly asymmetric in the experiment. The experimental asymmetry in the dominant $n = 5$ flow was within the uncertainty range of the asymmetry measured in cylindrical simulations. The phase of the $n = 5$ flow measured in experiment showed significant phase shifts from the single-fluid simulations, which have $n = 5$ flow profiles directly out-of-phase with the $n = 5$ magnetic mode, similar to reconnection-like flows. The phase shifts are suggestive of decoupling between ion and electron fluids, a two-fluid effect. The measured plasma flow is inconsistent with predictions from high dissipation simulation and exhibits evidence for the importance of two-fluid and toroidicity effects. However, the requirement to impose artificial boundary conditions in the simulation to achieve SHAx states leave open the question of which effects might be essential to the SHAx formation.

Finally, the velocity shear profiles are evaluated from the experimental data. There

is strong shear in the non-axisymmetric toroidal flow, as well as the axisymmetric flow in the poloidal plane. A method for calculating the shear in the helical angular velocity is presented and compared to the critical shear necessary to affect tearing modes based on an analysis of the eddy turnover time expected of the sub-dominant modes. The uncertainty in the calculated helical angular velocity is too large in the region between the helical magnetic axis and the adjacent sub-dominant tearing mode rational surface to make a strong statement about the size of flow shear's size relative to the critical shear. Improvements in both the velocity uncertainty and the uncertainty in the location of the helical magnetic axis are necessary to better resolve the calculated shear.

7.2. Future Work

With a larger dataset using the same measurement techniques, two areas of investigation become feasible. The multi-helicity state exists in 500 kA plasmas only transiently before the onset of QSH and eventually the saturated SHAx state. With more data (on the order of 2x more), profiles could begin to be obtained in the MH regime and compared to the saturated SHAx regime. Additional data might be helpful to explain the dynamical changes in the detailed structure of the plasma flow in the transition from MH to SHAx. Time dynamics in the SHAx state could also be analyzed, such as the correlation of plasma flow to oscillations in the dormant magnetic mode amplitude.

Computationally, two-fluid simulations of the SHAx state will help inform the effects two-fluid physics has on the flow profile. While experimental data show phase offsets similar to previous two-fluid work, it is far from a conclusive measurement. The simulation results used in the analysis incorporate simplifying assumptions, and more accurate simulations run using more realistic viscosity, resistivity, and thermal conduction profiles, as well as

incorporating two-fluid physics would help with interpreting the velocity measurements.

Improvements to the characterization of uncertainty could also be performed. The largest source of unaddressed uncertainty in the fits is the relative calibration offset between the two fibers. In all previous CHERS work it is assumed that the offset was 9 pm, and that the offset never changes. This has been studied in some depth by Darren Craig. However, synthetic data analysis suggests that an offset of as little as a 1/2 picometer at low light levels could give non-trivial systematic offsets in the velocity fit.

For every velocity data point collected, an ion temperature and radiance data point was also collected. The profiles given in Appendix B suggest that the ion temperature profile is mostly flat, with an unexpected spike in both axisymmetric and non-axisymmetric temperature profile at the outer edge at $r/a = 0.79$. There are numerous possible avenues to investigate with this data such as the role of the average neutral density profile in ion heat confinement in SHAx, and the impact of sawtooth crash heating (or lack thereof) in SHAx. With an appropriate estimate of the neutral beam density profile, the carbon density profile could be obtained from the radiance measurements to explore impurity transport in helical plasmas[1].

References

[1] M. D. Nornberg, D. J. Den Hartog, and L. M. Reusch, "Incorporating beam attenuation calculations into an integrated data analysis model for ion effective charge," *Fusion Science and Technology*, vol. 74, pp. 144–153, 1 2018.

A. Systematic differences in axisymmetric flow

The axisymmetric toroidal flow measured at $r/a = 0.28$ has a notable dependence on the specific run day, outside of the systematic error associated with the daily velocity calibration. At this location, two distinct profiles were observed between five run days, shown in Figure A.1 a.). While the perturbation amplitudes are similar for the two profiles, the axisymmeteric flows are very different, having an offset between the profiles on the order of 10 km/s.

To further characterize the axisymmetric flow for each day, the rotating multi-helicity state of each shot is considered. When the plasma is still rotating, there is an offset between the tearing mode velocity and the measured CHERS velocity at $r/a = 0.28$. The day-to-day difference between these two velocities correlates well with the day-to-day differences in differences in velocity measured in the locked SHAx state. This suggests that the differences in the axisymmetric velocity in the SHAx profiles are not unique to the SHAx state but present for the entire plasma lifetime. In fact, when the daily average difference between the CHERS velocity and tearing mode velocity in the MH state is subtracted from the CHERS velocity profiles in the SHAx state, the offset between SHAx velocity profiles for each day is

mostly eliminated, as shown in Figure A.1 b.).

Two possibilities are considered for what could cause plasma-condition-dependent differences in the axisymmetric toroidal velocity profiles: the loss in momentum by charge exchange with neutrals and an increase in momentum transport due to stochasticity. The analysis is informed by similar work done to explain the deceleration in the $n = 6$ tearing mode velocity in PPCD [1]. The possibility of a bad absolute wavelength calibration was briefly considered, but multiple calibrations are performed at the beginning and end of each day which agree to within a ±3 pm, which corresponds to ±3 km/s in the velocity parameter. This is well below the systematic offset between the two profiles. Ultimately, neither of the following analyses offer a good explanation for the differences observed in SHAx velocity profiles.

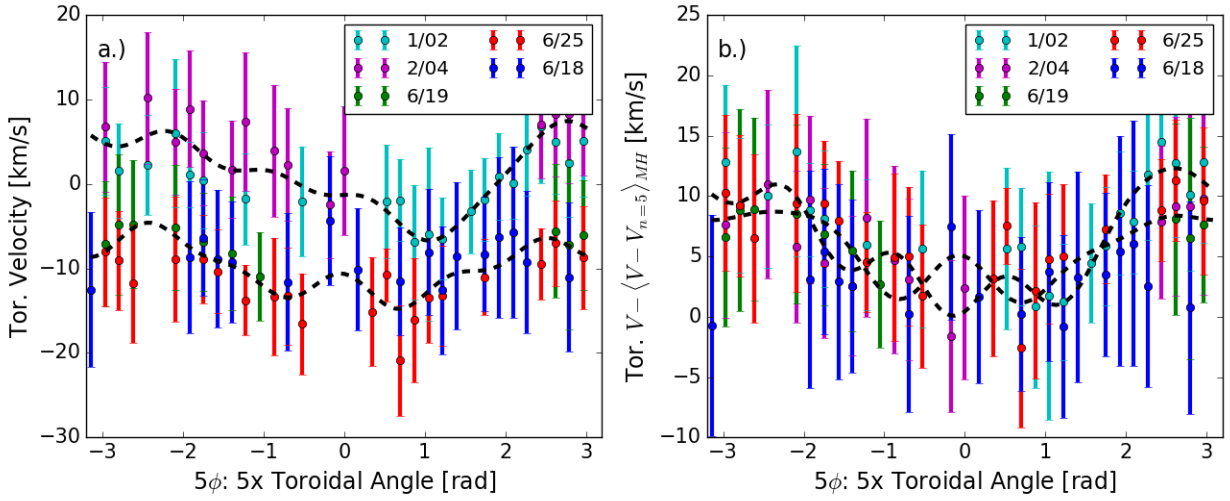

Figure A.1.: a.) Toroidal velocity binned every ten degrees in toroidal angle for each run day data was acquired at the radial location r/a = 0.28. Dotted black lines show two separate profiles for data acquired in June, 2018, and data acquired before June, 2018. b.) Toroidal velocity adjusted such that the there is no offset in tearing mode velocity and CHERS velocity before mode locking.

First the momentum loss by charge exchange with neutrals is examined. A change in the

neutral density should correlate to a change in the total Balmer H_α line emission observed from neutral particles in the edge. While drag on the plasma depends on the detailed neutral density profile, the total neutral content in the edge should act as a good proxy for the overall effect. MST has an array of D_α cameras that monitor these light levels every shot. As can be seen in Figure A.2, there is no substantial correlation with the run day. The 6/18 run day had systematically higher light levels than the rest of the other four days, however. The 6/18 run day also appeared to have less velocity variation with toroidal angle as well. It is possible, but inconclusive, that the larger source of neutrals has a net damping effect on the non-axisymmetric velocity. Given the overlap in D_α emission from the other four days, it is unlikely that the drag on the plasma from neutrals is the reason for the day-to-day difference in axisymmetric velocities.

The momentum transport due to stochasticity is examined next. Stochasticity is caused by the presence of the sub-dominant tearing modes, and scales with the strength of the sub-dominant tearing mode amplitude. If the flow profiles were strongly affected by the stochastic momentum transport, systematic offsets in the combined sub-dominant tearing mode amplitude similar to the offsets seen in the CHERS velocity profiles should appear. As Figure A.3 shows, that is not the case, and the secondary tearing modes for each day overlap over most of the toroidal profile.

There is no clear explanation for the difference in axisymmetric toroidal flow observed at $r/a = 0.28$ betweeen data taken in June, 2018 and before June, 2018. The non-axisymmetric flow between the two days is similar, however. Given that the axisymmetric toroidal flow of the adjacent radial locations is more in line with the profile obtained in June, 2018, and more days were used to acquire that profile, the data acquired before June, 2018 is considered an outlier and not used to provide Fourier components of the flow at that location.

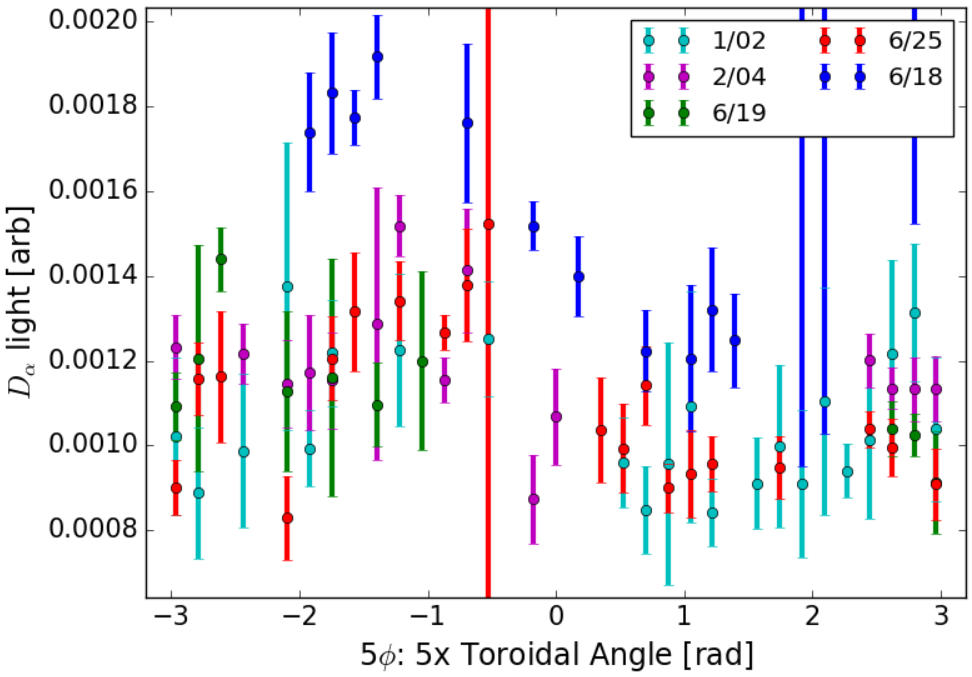

Figure A.2.: The observed D_α light vs toroidal angle of the helical equilibrium for each of the days toroidal velocity data was taken at $r/a = 0.28$, measured at an impact parameter whose line-of-sight is tangent to $r/a = 0.304$. The light levels fall in the same regime for four of the five days.

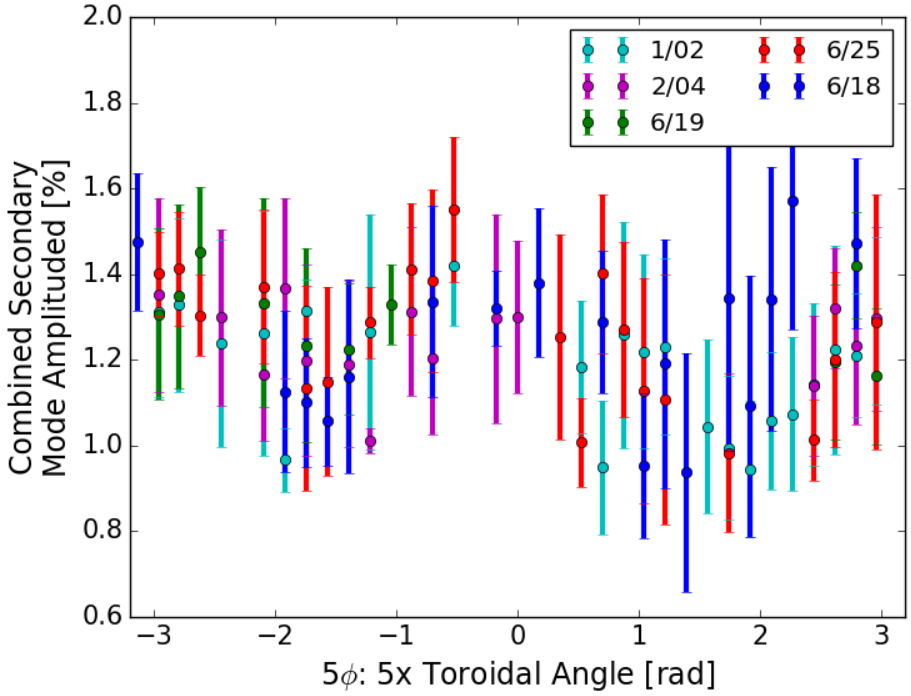

Figure A.3.: Sub-dominant tearing mode amplitudes do not change substantially day to day.

References

[1] D. Craig, E. H. Tan, B. Schott, J. K. Anderson, J. Boguski, D. J. Den Hartog, T. Nishizawa, M. D. Nornberg, and Z. A. Xing, "Intrinsic flow and tearing mode rotation in the RFP during improved confinement," *Physics of Plasmas*, vol. 26, p. 072503, 7 2019.

B. Temperature Measurements

Since a temperature measurement is available for every velocity measurement made, a corresponding dataset of temperature profiles is available for analysis. While not the focus of this thesis, the measurements are provided for reference in this appendix.

Overall, the ion temperature is relatively uniform. Toroidal variation is on the order of 20 eV, and the radial variation of the axisymmetric temperature is of the order of 40 eV. At the edge, $r/a = 0.79$, there is an inexplicable increase in both the average temperature and the $n = 5$ toroidal variation. This can be easily be seen in the data used for fitting, shown in Figure B.4.

This is a significantly lower ion temperature than expected from previous RFP temperature measurements, which typically yields a T_i/T_e ratio of 2/3. This ratio is closer to 1/3. There are two likely possibilities for this. The first is increased cooling from charge exchange due to a larger neutral density profile, recently explored in R. Norval's 2019 thesis. Secondly, the primary heating mechanism for ions is the sawtooth crash, which are absent in the QSH/SHAx state.

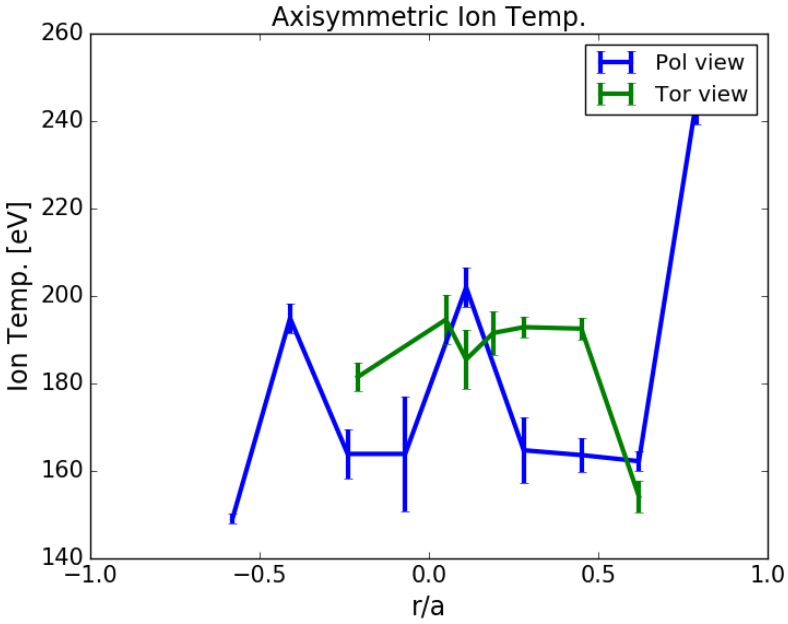

Figure B.1.: Axisymmetric Ion temperature profile measured from both the toroidal and poloidal view.

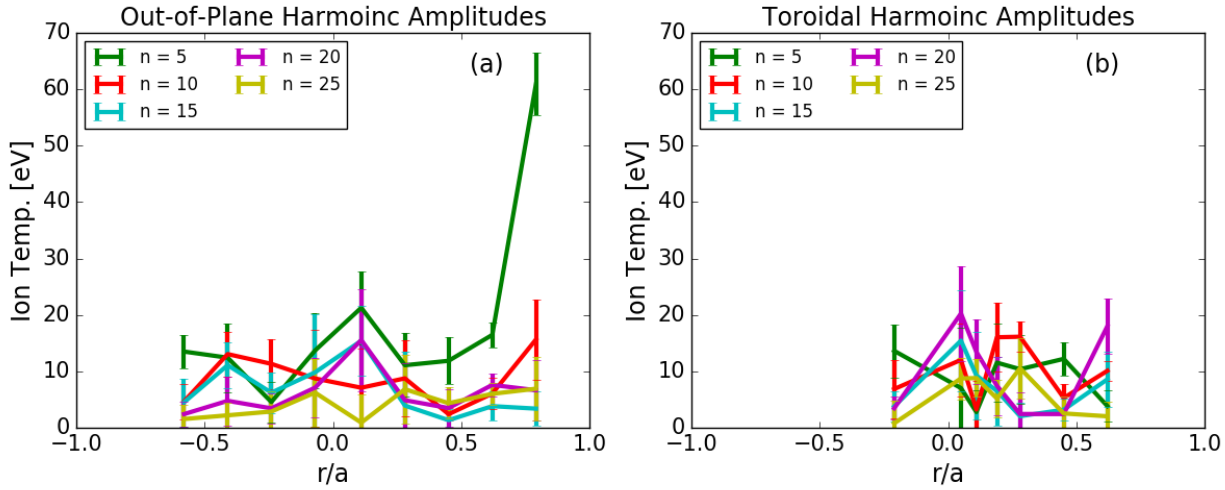

Figure B.2.: Perturbed temperature mode profile measured from the (a) poloidal view and (b) toroidal view

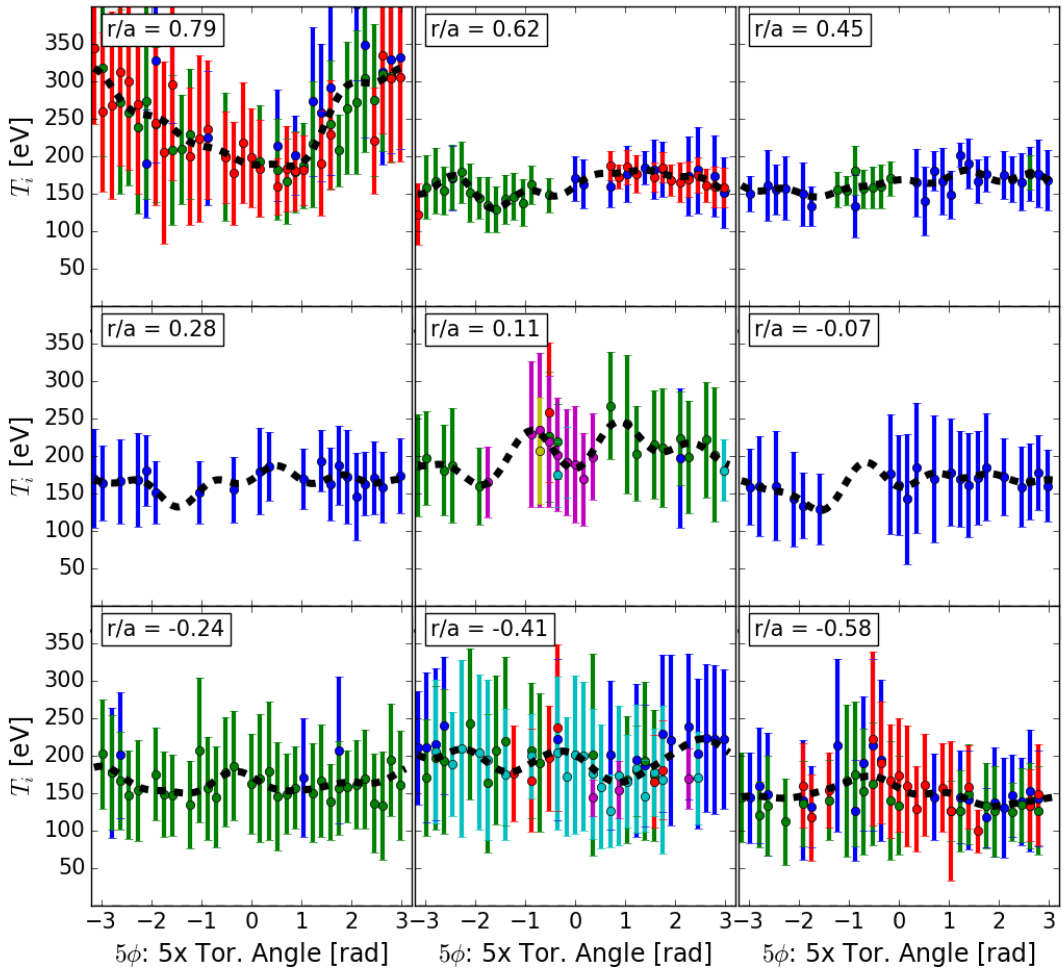

Figure B.3.: Temperature profiles measured from the poloidal CHERS views vs helical toroidal angle

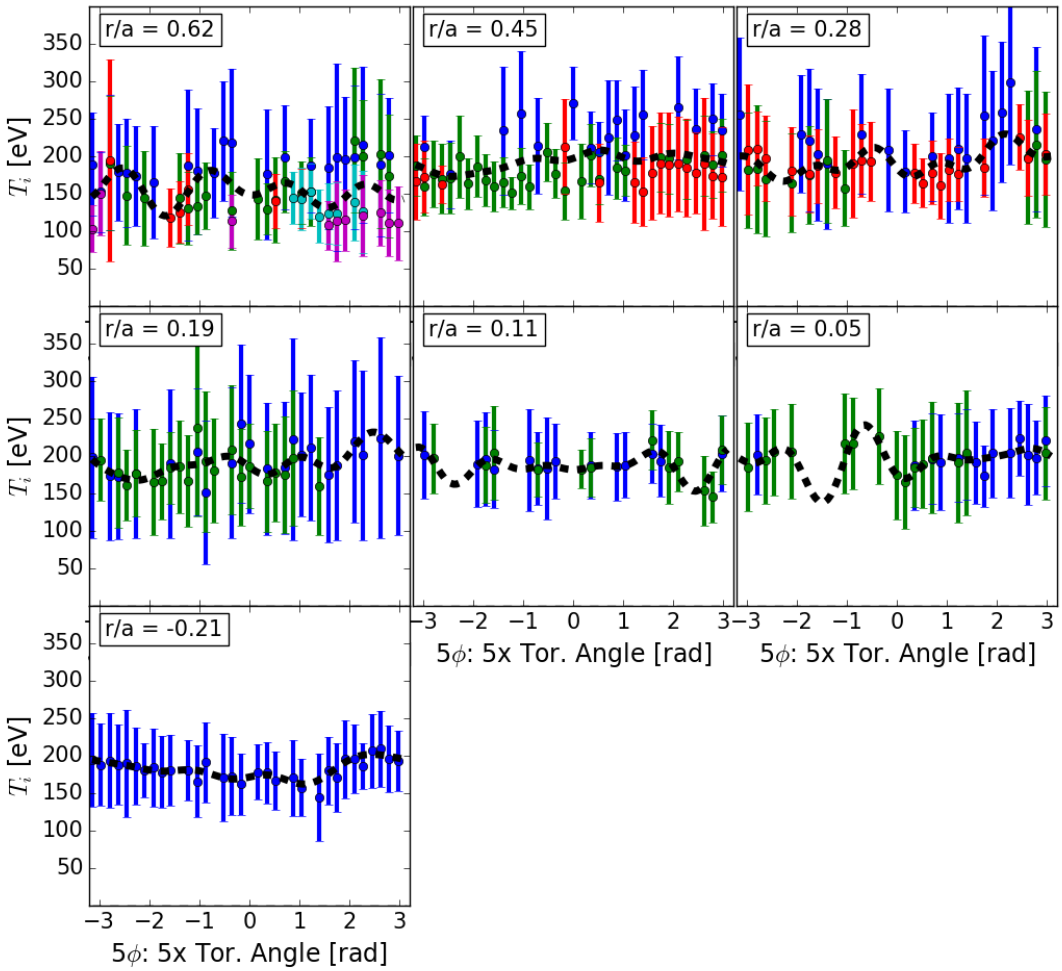

Figure B.4.: Temperature profiles measured from the toroidal CHERS views vs helical toroidal angle